An SPH-based Modelling Approach to Enhance the Predictability of Nano-scale Mechanical Machining

A thesis submitted in partial fulfilment

of the requirement for the degree of Doctor of Philosophy

Hao Shen

April 2024

School of Engineering
Ysgol Peirianneg

Abstract

Atomic Force Microscope (AFM) probe-based mechanical machining has attracted the attention of the research community over the past twenty years as a potential tool for conducting micro and nano-scale mechanical material removal operations. This technique has demonstrated potential applications in mechanical, physical, chemical, biomedical and other interdisciplinary fields. However, a current research issue affecting its wider utilisation is the lack of accurate simulation tools to quantitatively predict the process outcomes. In this context, this Thesis explores the possibility of employing a mesh-free numerical method, namely Smooth Particle Hydrodynamics (SPH), to simulate several scenarios in AFM-based micro and nano-scale machining.

Up to Chapter 4, the SPH modelling of nano-indentation was conducted using the ANSYS/LS-DYNA software using three different published studies as benchmarks. The SPH outcomes were found to compare well against finite element modeling and experimental results reported in benchmark studies in the context of both micro and nano-scale indentation processes. These feasibility studies conducted in this chapter suggested that the SPH mthod is a technique with the potential to be considered more widely by researchers investigating high strain, or strain rate, deformation phenomena on the nanoscale. For example, the presented research on the development of an SPH-based nano-indentation model lays the foundations towards formulating a more comprehensive SPH model for the accurate simulation of nanoscale tool-based machining processes in following Chapters.

Based on the above conclusion, Chapter 5 of the Thesis extended the complexity of the implemented SPH model by considering the influence of the lateral motion between the indenter and the sample following initial nano-indentation. In particular, the simulation of the nano-machining process on copper using SPH was conducted with a specific view to study the influence of the selected material constitutive model, namely the Johnson-Cook and the elasto-plastic models. The

simulated cutting and normal forces as well as the machined topography using both constitutive models were compared with the experimental work from existing literature. The SPH simulation results showed that using the Johnson-Cook material model, cutting and normal forces were closer to the experimental data compared to the results obtained with the elasto-plastic model. The results also showed that the cross-sectional profile of simulated nano-grooves using the Johnson-Cook model was closer to the experimental results. Therefore, the work conducted in Chapter 5 showed that the selection of the Johnson-Cook model is preferable for the SPH modelling of the nano-machining process.

The last part of the Thesis (i.e. Chapter 6) developed a novel SPH model in the context of AFM tip-based dynamic ploughing lithography (DPL), in which the AFM tip vibrates in vertical direction while machining in the horizontal direction. The SPH-predicted forces and surface topographies of AFM probe-based DPL were comprehensively investigated. The SPH simulation results showed that 3D periodic nanostructures with triangular-shaped profiles were clearly visible with a relatively large vibration period. In addition, the height of the generated periodic nanostructure was subject to the viewing direction. These SPH simulation results shed light on the possibility of employing AFM-based DPL for fabricating 3D periodic nanostructures with triangular-shaped or sinusoidal profile waveforms.

In summary, the implemented SPH models in this Thesis could be used as a suitable first approximation to predict the process outcomes during both nano-indentation and nano-machining. In addition, the SPH simulation results reported in this Thesis theoretically confirmed the possibility of employing AFM-based DPL for fabricating triangular-shaped waveform nanostructures with desired dimensions.

Acknowledgements

First, I would like to express my sincere gratitude to my supervisors, Prof Emmanuel Brousseau and Dr Sivakumar Kulasegaram. I would like to thank Prof Emmanuel Brousseau for his patient guidance throughout my PhD study and for helping me develop the skills of a professional academic researcher. Besides being a mentor and guide, Prof Emmanuel Brousseau is also like a very good friend. He was considerate of my mental health when I was dealing with research stress, and he also helped me cope with the mistakes and unpredictability of my PhD research and other inevitable challenges. I would also like to thank Dr Sivakumar Kulasegaram for his constructive suggestions and technical guidance in numerical simulation work, which is of vital importance in my PhD research. Dr Sivakumar Kulasegaram is also thanked for his continuous support and help in the weekly joint meeting and in correcting my published papers and thesis. I am exceptionally lucky and grateful for having the opportunity to conduct my PhD research with my excellent supervisors.

Second, I would like to thank my friends and office members in Cardiff, who made my stay in Cardiff a meaningful and unforgettable journey. In particular, Dr Yang Jiao, Dr Sameeh Baqain, Dr Xiaobo Wang, Dr Jun Song, and Mr Hongjin Luv are thanked for their support and help both in my PhD research and in my life in Cardiff.

In addition, I wish to express my thanks to the China Scholarship Council and Cardiff School of Engineering for the financial support during my PhD study.

Finally, I would like to thank my family for their unconditional love and understanding. They always stand by me and give me constant support and encouragement. I hope to pursue my future career with their love and company.

List of publications

- **Hao Shen**, Emmanuel Brousseau, and Sivakumar Kulasegaram*. "Assessment and validation of SPH modeling for nano-indentation." *Computational Particle Mechanics* 10.3 (2023): 603-613.
- **Hao Shen**, Emmanuel Brousseau, and Sivakumar Kulasegaram. "Assessment and investigation of SPH modelling for nano-scratching." Presented at: *8th International Conference on Nanomanufacturing & 4th AET Symposium on ACSM and Digital Manufacturing* (*Nanoman-AETS*), Ireland, 30 August - 1 September, 2022.

Contents

List of figures

List of tables

List of abbreviations

AFM	Atomic Force Microscope
DDD	Discrete Dislocation Dynamics
DPL	Dynamic Ploughing Lithography
EAM	Embedded Atom Model
EDM	Electro Discharge Machining
EOS	Equation of State
FEM	Finite Element Method
FIB	Focused Ion Beam
KDP	Potassium Dihydrogen Phosphate
LSE	Lateral Size Effect
MD	Molecular Dynamics
MEMS	Micro-Electro-Mechanical Systems
MPMs	Mesh-free Particle-based Methods
NCP	Nano-scale Contact Pressure
ODEs	Ordinary Differential Equations
OFHC	Oxygen-free High-conductivity Copper
PDEs	Partial Differential Equations
POCT	Point-of-care Testing
SERS	Surface Enhanced Raman Spectroscopy
SPH	Smooth Particle Hydrodynamics

Nomenclature

Ra (nm)	Arithmetical mean deviation of the roughness profile
f_s	Contact force
C_i	Contact location
ρ_j	Density of SPH particle j
ε^p_{eff}	Effective plastic strain
ε	Equivalent plastic strain
F_y	Friction force
β (GPa)	Hardening parameter
v_x (m/s)	Horizontal speed of AFM-based DPL
H (nm)	Indentation depth
σ_0 (GPa)	Initial yield strength
Ω	Integration domain
b	Length of edges of the diamond tip
m_j	Mass of SPH particle j
N_m	Master node
S_i	Master segment related to N_{mi}
A (GPa)	Material yield stress
k	Ratio between the indentation depth and influence depth
T_m (K)	Reference melting temperature
T_0 (K)	Reference temperature
α (degree)	Rotation angle of the inclined slice plane

a	Side length of the diamond tip
N_s	Slave node
W	Smoothing function
h	Smoothing length
n	Strain hardening coefficient
C	Strain rate parameter
B (GPa)	Strength coefficient
E_t (GPa)	Tangent modulus
T (K)	Temperature
m	Temperature coefficient
$\dot{\varepsilon}$	Time derivative of the plastic strain
$\dot{\varepsilon}_0$	User-defined plastic strain rate
A_m (nm)	Vibration amplitude of AFM-based DPL
T (nm)	Vibration period of AFM-based DPL
σ	Von Mises tensile flow stress
σ_y (GPa)	Yield strength
E (GPa)	Young's modulus

Chapter 1 Introduction

1.1 Background and motivation

Micro and nano-scale mechanical machining technologies enable effective machining of micro and nano-scale products with intricate features in various engineering materials. Atomic Force Microscope (AFM) probe-based mechanical machining, as a more specific process in this group of technologies, has attracted the attention of research community over the past twenty years as a potential tool for conducting micro and nano-scale mechanical material removal operations. As illustrated in Fig. 1.1, this process is realised on an AFM instrument. In this case, the nano-scale cutting tool used is simply the AFM probe as it possesses a tip with a cutting edge radius of a few tens of nanometres. When implementing this process, the AFM tip is actuated to move horizontally in the direction parallel to the sample surface to generate a nano-groove or more complex nanostructures. This technique has demonstrated potential applications in mechanical, physical, chemical, biomedical and other interdisciplinary fields. For example, AFM probe-based nanomilling process has been utilised to fabricate nanofluidic chips with multiple and controllable nanochannels (Wang et al., 2019), which are essential for medical and biological applications such as point-of-care testing (POCT) and virus detection. AFM probe-based nano-machining can also be used to fabricate periodic nanostructures with sinusoidal waveforms (Geng et al., 2017; Geng et al., 2018), which played an important role in surface enhanced Raman spectroscopy (SERS) (Wang et al., 2020). In addition, AFM-based nano-machining is potentially valuable for the fabrication of nanowires and nanosensors, which can find applications in chemical sensing (Lin et al., 2008). Therefore, the development of AFM-based micro and nano-scale machining provides an alternative and attractive tool for material removal operations at the micro and nanoscale.

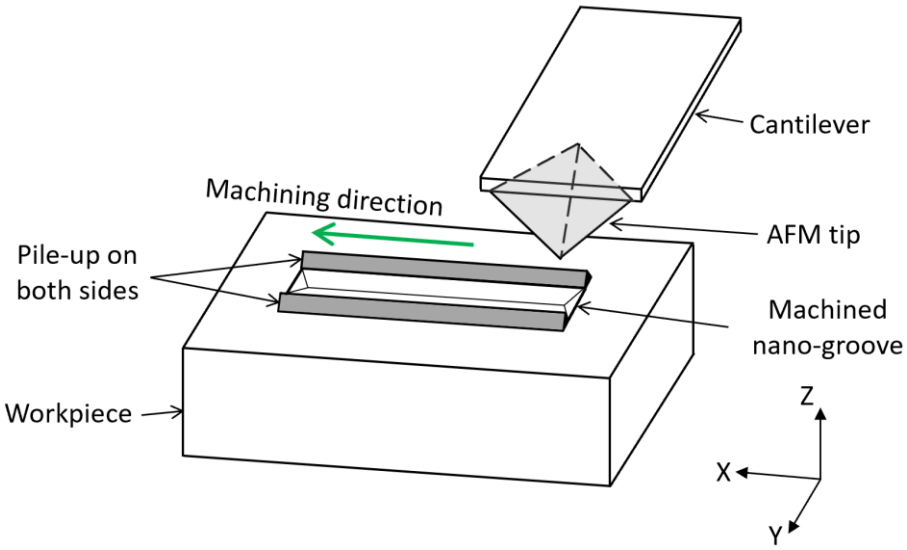

Fig. 1.1. Schematic diagram of AFM probe-based nano-scale mechanical machining.

Although complex micro and nano-scale features can be fabricated with AFM probe-based mechanical machining in a cost-effective manner and relatively easily, a current research issue affecting its wider utilisation is the lack of accurate simulation tools to quantitatively predict the process outcomes with reliable accuracy. This technological issue is linked to some underlying scientific challenges associated with micro and nano-scale mechanical machining, which can be described in detail as follows. Although kinematically similar to conventional macro mechanical machining, micro and nano-scale mechanical machining is fundamentally different from conventional macro mechanical machining in many aspects due to the size effects. More specifically, when the uncut chip thickness reaches the level of micrometre or nanometre, issues of cutting tool edge radius, negative rake angle of cutting tool, grain size and dislocations inside the workpiece material, considered to have little or no influence at macro scale, become dominant factors with strong influences on the micro and nano-scale machining mechanics. In other words, as the uncut chip thickness further decreases at micro and nano-scale, the size effects can change the whole aspect of the machining. Therefore, most traditional macro mechanical machining models which neglect the cutting tool radius and employ homogeneous and isotropic workpiece

materials cannot be directly applied to micro and nano-scale mechanical machining. To date, most research efforts in the field of micro and nano-scale mechanical machining still rely on extensive experimental trials, which can be not only expensive and time-consuming but also 1) provide limited insight into new machining phenomena, 2) provide limited insight into underlying micro and nano-scale cutting mechanics and 3) lead to limited scope for predicting the material responses when new processing conditions are investigated. In this context, theoretical studies should be performed to reveal underlying micro and nano-scale mechanical machining mechanics, with the ultimate objective of improving the reliability and predictability of the micro and nano-scale mechanical machining process.

In order to address this problem, some researchers have reported efforts using analytical approaches (Liu and Melkote, 2006) to predict the machined surface generated by small scale mechanical machining. The main point of these approaches is to calculate intersection points or surface profiles between consecutive tool paths. In addition to analytical approaches, tackling this problem has been attempted using the conventional mesh-based finite element method (FEM). The reported FEM simulations efforts focused on modelling and predicting machining phenomena at the micro and meso scales, such as stress distribution (Woon et al., 2008), chip formation (Mabrouki et al., 2008) and cutting forces (Kurniawan et al., 2021). Some researchers have focused on modelling micro and nano-scale mechanical machining through molecular dynamics (MD). This approach has been successfully applied to investigate a variety of process outcomes in nano-scale mechanical machining and to describe nano-scale machining phenomena, such as cutting forces (Lin and Huang, 2008), chip morphology (Markopoulos et al., 2018), defect evolution (Zhao et al., 2021) and topography of machined surface (Xu et al., 2019; Huo et al., 2007).

However, a number of challenges associated with the above modelling approaches. More specifically, the accuracy of analytical modelling approaches is relatively limited due to the construction of layers of assumptions and simplifications. In addition, an analytical model provides limited insight into the machining characteristics associated with the machining process, such as chip formation and cutting forces. Numerical simulations can predict a wider number of machining outcomes with less simplifying assumptions, but they still have a number of limitations. For example, FEM has inherent numerical difficulties (i.e. re-meshing techniques and the generation of highly distorted meshes) when simulating mechanical machining problems where large deformations and cracking occur (Chuzhoy et al., 2003). In addition, FEM can provide only limited nano-scale information such the defect evolution during plastic deformation. The main limitation of MD simulations is that this approach can only output machining responses over restricted lengths because of the associated computational cost. As the next chapter will elaborate, the maximum machining length among the reported MD simulations for AFM-based machining is found to be 30 nm (Zhao et al., 2021), which is less than the typical dimensions of features cut via this process. In summary, due to these limitations, there is scope for conducting further numerical simulation research in the field of micro and nano-scale mechanical machining.

In this context, this Thesis explores the possibility of employing an alternative mesh-free numerical method, namely Smooth Particle Hydrodynamics (SPH), to simulate several scenarios in micro and nano-scale mechanical machining. When using the SPH method for this purpose, the processed specimen is discretised into a set of SPH particles, which possess all the individual material properties and deform or move according to the governing conservation equations. The topographical modification of the sample surface is simulated by the collective movement of those SPH particles. On the one hand, SPH simplifies the discretisation of the specimen and can easily handle mechanical machining problems with large strains and strain rates, since refinement

of particles is more easily performed than mesh refinement. On the other hand, the SPH method still relies on constitutive models and thus the investigated length scale in SPH can reach several hundreds of nanometres or several tens of micrometres. Thus, the SPH method could be an alternative approach to FEM and MD when modelling micro and nano-scale mechanical machining conducted with an AFM tip. In fact, the SPH method has demonstrated the potential to be applied in the fracture of brittle solids (Benz and Asphaug, 1995), metal forming (Bonet and Kulasegaram, 2000) and high velocity impacts (Johnson et al., 1996). Therefore, this Thesis explores the possibility of extending the application of SPH method to the modelling of the AFM-based micro and nano-scale mechanical machining process.

1.2 Research aim and objectives

As presented above, the research aim of this PhD research is to gain a better scientific understanding of the fundamental mechanics (such as cutting forces, surface generation, material deformation mechanisms and machined surface topographies) of AFM-based nano-scale mechanical machining process with the aid of SPH simulations. The objective of this PhD research is to explore the possibility of extending the application of the SPH method to the modelling of several scenarios in AFM-based micro and nano-scale mechanical machining. In particular, the objectives of this PhD research are as follows.

1. Simulate the nano-indentation process by first reproducing an existing SPH model of nano-indentation, and then validate the implemented SPH-based nano-indentation model from the perspectives of 1) force-displacement response, 2) stress and strain distribution, 3) the influence depth of the area where indentation-induced stress exists and 4) the effect of shape of the nano-indenter.

2. Model and simulate the nano-machining process using the SPH method based on the implemented SPH nano-indentation model and compare the influence of

adopted constitutive material models on the material response with respect to cutting forces and the machined surface topography.

3. Characterise the AFM probe-based dynamic ploughing lithography (DPL) process using the SPH method with a view to predict the machined surface topography (with a focus on nanostructure patterns, feature sizes and the surface quality) when new machining conditions of dynamic ploughing are investigated.

The identification of knowledge gaps that have motivated the work completed in this thesis is discussed in more detail in Chapter 2. These knowledge gaps guided the formulation of the above key objectives of the Thesis.

1.3 Thesis contribution

Following the research aim and objectives outlined in section 1.2, this section details the principal contributions of the Thesis.

The Thesis successfully reproduced an SPH model of nano-indentation from existing literature, and expanded it by incorporating complementary work such as the identification of indentation speed, the implementation of the stress-strain relationship in LS-DYNA and detailed modelling procedures. A convergence study was conducted to determine the optimal particle density, thereby reducing the errors in particle approximation and enhancing the accuracy of the reproduced SPH nano-indentation model. Furthermore, the Thesis included an additional micro-indentation benchmark study for validating the reproduced SPH model against FEM predictions and experimental data in existing literature. The research in this part concluded with an investigation into the influence of the nano-indenter tip shape on the force-displacement response, providing enhanced confidence about 1) reliability of the reproduced SPH model of nano-indentation and 2) investigation

of process conditions that influence the nano-indentation process using the SPH method.

The Thesis established an SPH model for nano-machining of copper based on the implemented SPH nano-indentation model, utilising two distinct constitutive material models: Johnson-Cook and elasto-plastic material models. The comparison of these models' influence on simulation results included an analysis of cutting and normal forces at varying depths, the impact of cutting speed on simulated forces, and the surface topography of machined nano-scale grooves. The simulation results indicated that the Johnson-Cook model more accurately predicts forces and surface profiles, aligning closely with experimental results in existing literature.

In a pioneering effort, the Thesis applied SPH modelling to simulate the AFM probe-based DPL process. The SPH model was evaluated in comparison with MD results in existing literature, demonstrating the feasibility of SPH in predicting forces during dynamic ploughing and simulating surface topography. The study comprehensively investigated the surface topographies predicted by the SPH method, including the effects of vibration amplitude and period on nano-groove dimensions and the generation of periodic nanostructures. Additionally, the roughness profiles and roughness values of simulated nano-grooves were assessed across different dynamic ploughing periods, contributing to the understanding of how these process parameters influence the quality and characteristics of machined surfaces.

These contributions assist the scientific understanding of some mechanics aspects of AFM-based nano-scale mechanical machining, such as cutting forces, surface generation and machined surface topographies. They also validate and enhance the reliability and predictability of the AFM-based nano-scale mechanical machining process by employing SPH to simulate several scenarios in this process.

The Thesis's findings aim to provide a foundation for the development and application of accurate simulation tools, which are essential for the field of micro and nano-scale mechanical machining.

1.4 Thesis layout

The following diagram illustration (Fig. 1.2) provides an outline of this PhD thesis and explains the philosophical thinking behind the thesis structure. Detailed explanations of this diagram illustration are as follows.

Various industrial applications (such as medical engineering, nanofluidic chips, biotechnology, communications and optics, chemical sensing) are the main driving force behind the research on AFM probe-based mechanical machining and this PhD research. A current technological challenge of this technique which hinders its wider application is the lack of accurate simulation tools to enhance the predictability, reliability and process optimisation capability of this technique. To address this technological challenge, emphasis should be put on the underlying scientific challenges of micro and nano-scale mechanical machining, which focus on the micro and nano-scale cutting mechanics. After identifying the underlying scientific challenges of micro and nano-scale mechanical machining, Chapter 2 provides a comprehensive review of some numerical simulation methods which are commonly used to study different aspects of micro and nano-scale cutting mechanics, such as stress and strain distribution, cutting forces, chip formation, cutting phenomena, tool wear and surface generation. Among these numerical simulation methods, the SPH method is selected as the numerical method employed in this PhD research due to its adaptive, meshfree, Lagrangian and particle nature. The essential SPH formulations for

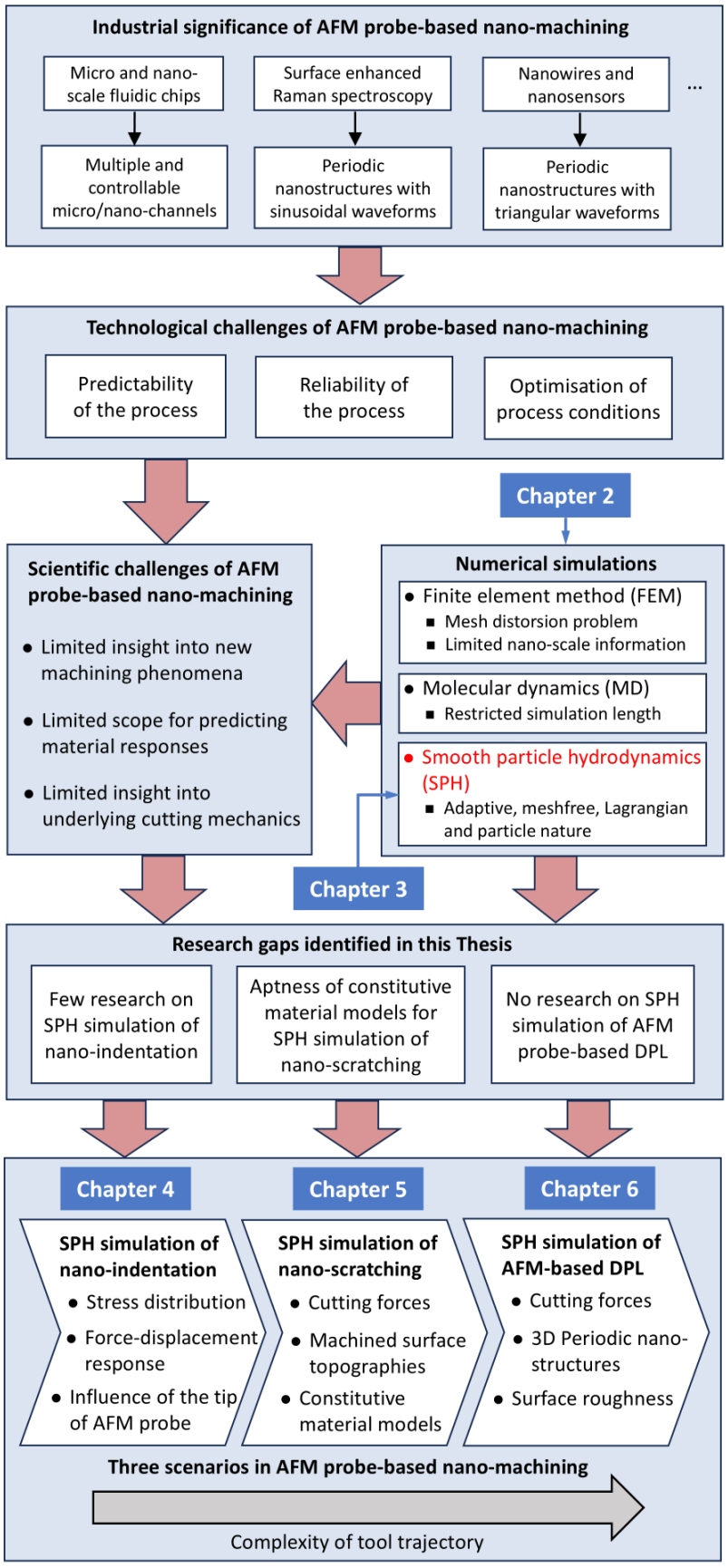

Fig. 1.2. The outline of this PhD Thesis.

micro and nano-scale mechanical machining and the computer implementation of SPH models within the ANSYS/LS-DYNA software are presented in details in Chapter 3. In the review of SPH simulations of micro and nano-scale mechanical machining in Chapter 2, three knowledge gaps are identified in three scenarios in AFM probe-based nano-scale mechanical machining, that is, nano-indentation, nano-scratching and AFM tip-based dynamic ploughing lithography (DPL). These three knowledge gaps motivated and correspond to the work completed in Chapter 4, Chapter 5 and Chapter 6, respectively. The main aspects of micro and nano-scale cutting mechanics concerned in Chapter 4 to Chapter 6 include stress distribution, cutting forces, surface generation, aptness of constitutive material models and surface roughness. From Chapter 4 to Chapter 6, the complexity of the motion between the tip and the sample is increasing and the simulation studies in Chapter 5 and Chapter 6 can be regarded as building on the results gained in the previous chapter. Finally, the resultant scientific understanding of different aspects of micro and nano-scale cutting mechanics, which are gained in Chapter 4 to Chapter 6, can be applied to AFM probe-based mechanical machining to enhance its reliability and predictability and fabricate micro and nano-scale features in various industrial applications.

To further elaborate, the chapters of this thesis are described in greater detail as follows:

Chapter 2 reviews numerical methods used by researchers (i.e. analytical methods, finite element method, molecular dynamics) for the simulation of micro and nano-scale mechanical machining. AFM probe-based mechanical machining is also presented with some additional level of details as it is in the context of this technique that the simulation work reported in this Thesis has been conducted. Finally, this chapter reviews recent development of the SPH method for the simulation of micro and nano-scale mechanical machining and discusses the identification of associated knowledge gaps that have motivated the work completed in this research.

Chapter 3 introduces some basic concepts (i.e. the kernel approximation and the particle approximation) behind the SPH method and the detailed formulation of SPH approximations. In addition, this chapter presents the calculation workflow of SPH simulations conducted in this Thesis with the ANSYS/LS-DYNA software. The material constitutive models and the contact model employed in this workflow are also presented. Finally, a convergence study to determine the optimal particle density for all subsequent simulations is conducted and dimensions of modelled diamond tips are presented, as these represent general information which is useful for the following chapters.

Chapter 4 aims to address the first knowledge gap identified. An SPH model of nano-indentation reported in existing literature is first reproduced and this implemented SPH model is then validated by comparing its outcomes with those published in the literature. Next, an additional benchmark study in the context of micro-indentation is considered and modelled to further establish and refine the accuracy of the implemented SPH model. Finally, the validated SPH model of nano-indentation is employed to investigate the influence of the shape of the nano-indenter tip on material response in the context of a nano-indentation study available in existing literature.

Chapter 5 aims to address the second knowledge gap. A nano-machining model of copper is implemented using SPH in this chapter to complement existing literature, with a specific view to study the influence of the selected material constitutive model on the material response. This is achieved by considering the Johnson-Cook and an elasto-plastic model and by analysing their effect on the simulated cutting and normal forces as well as on the surface topography of the machined nano-scale groove. The simulated data are finally compared against experimental results available in the literature.

Chapter 6 aims to address the third knowledge gap. An AFM-based DPL model reported in existing literature is first reproduced using the SPH method. Then, the SPH-predicted results are compared with MD simulation results published in the literature concerning cutting forces and the simulated surface topography. Following this, the effects of machining conditions of dynamic ploughing (i.e. the vibration amplitude and the period) on the generated periodic nanostructures are investigated in detail. The profile waveforms of the simulated periodic nanostructures are also quantitatively assessed. Finally, the roughness profile of simulated nanostructures and the corresponding arithmetical mean deviation of the roughness profile are evaluated for different periods of dynamic ploughing.

Chapter 7 presents the conclusions, research contributions of the Thesis and recommendations for further work.

Chapter 2 Literature Review

2.1 Overview

The main focus of this Chapter is to present current numerical methods for the simulation of micro and nano-scale mechanical machining and to identify associated knowledge gaps that have motivated the work completed in this Thesis. To achieve the aim of this Chapter, the next section starts by briefly introducing a number of micro and nano-scale machining technologies (e.g., vacuum and mask-based lithography techniques, micro and nano-scale mechanical machining, micro-electro discharge machining, laser micro-machining and focused ion beam micro-machining) as well as different definitions for the more specific process of mechanical machining at such small scales. In this section, Atomic Force Microscope (AFM) probe-based mechanical machining is also presented with some additional level of details as it is in the context of this technique that the simulation work reported in this research has been conducted. Next, the following section 2.3 reviews methods used in the past for the simulation of micro and nano-scale mechanical machining. Analytical methods are presented first before focusing in greater depth on numerical methods, which include the finite element method (FEM), molecular dynamics (MD) and smooth particle hydrodynamics (SPH) method. Advantages and limitations of these methods are also discussed in this section. The final section 2.4 presents a number of research and knowledge gaps that have been identified following this review and constitute the specific focus of the work conducted in this research.

2.2 Introduction to micro and nano-scale machining

The development of novel micro and nano-scale manufacturing technologies is a research area of high importance. Although vacuum and mask-based lithography techniques (Engstrom et al., 2014; Dimov et al., 2012) are employed in industry for the fabrication of semi-conductor devices and derived micro-electro-mechanical systems (MEMS) components, they still have several limitations (Menard and Ramsey, 2011; Liao et al., 2012; Devlin et al., 2009). In particular, these fabrication technologies

generally rely on capital-intensive equipment while being restricted to the fabrication of planar features and constrained to a limited set of processed materials. Besides, there are also increased concerns over their environmental friendliness as they are energy and resource intensive and generate significant waste (Fang et al., 2017). New micro and nano-scale manufacturing technologies have been developed by the research community to address these technological gaps. Gao and Huang (2017) reviewed recent developments and applications of four alternative micro-machining technologies, including micro mechanical machining (Dornfeld et al., 2006), micro-electro discharge machining (micro-EDM) (Liao et al., 2005), laser micro-machining (Mao et al., 2016), and focused ion beam (FIB) micro-machining (Chang et al., 2016). Micro mechanical machining technologies, which include micro-turning (Rahman et al., 2010), micro-milling (Câmara et al., 2012), micro-drilling (Egashira and Mizutani, 2002) and micro-grinding (Aurich et al., 2009), have the highest machining efficiency and can machine micro-scale products with intricate features in various engineering materials such as metals, polymers, ceramics, silicon, and glass.

Similar to conventional macroscale machining, micro and nano-scale mechanical machining refers to the material removal process from a workpiece by employing micro and nano-scale tools with geometrically defined cutting edges. Some researchers have defined this process based on different viewpoints. For example, one definition of microscale machining is based on the cutting condition that the uncut chip thickness is less than 999 μm (Masuzawa, 2000; Takacs et al., 2003). However, this definition neglects some characteristics of micro-scale machining which are distinguished from conventional macro-scale machining, such as the microstructure of the workpiece material and tool geometry. Considering these two differences between micro and macro-scale machining, Simoneau et al. (2006) defined micro-scale machining based on the grain size, as the point where the uncut chip thickness is less than the average grain size of the smallest grain type. Fang and Xu (2018) defined micro-scale machining based on the tool edge, for which the effect of cutting

edge radius could not be ignored. Similarly, nano-scale machining is defined by these authors in the same way where the uncut chip thickness is on the nano-scale and less than the average grain size of the smallest grain type, or where the effect of the tool edge could not be ignored.

The development of AFM-based micro and nano-scale machining techniques provide an alternative and powerful tool for material removal operations at such small scales. Although AFM was initially invented as a technology to measure the surface topography of specimens on the nano-scale (Binnig et al., 1986) and then further developed to extract mechanical properties of the probed surfaces, over the past twenty years it has attracted the attention of the research community as a potential tool to conduct micro and nano-scale mechanical machining operations (see, e.g. reviews in (Tseng, 2011; Yan et al., 2015; Xie et al., 2006)). In this case, the nano-scale cutting tool used is simply the AFM probe, as such probes typically possess a tip with a cutting edge radius of a few tens of nanometres. AFM probe-based machining can be seen as a process in which a diamond asperity slides over a sample surface. However, the main difference between this process and micro-cutting is that the nano-scale cutting tool used with an AFM is a flexible mechanism as it is a cantilever-type structure, which is not the case in micro-cutting. This means that the deflection of the cantilever during nano-scale scratching has a distinct influence on the actual normal load applied on the sample surface and the machined nanostructures (Sun et al., 2013). Another area of current investigations with AFM probe-based machining is related to the tip wear after long-distance scratching, as this effect could not be neglected (Noritaka et al., 2005; Zong et al., 2010) and thus would limit the throughput of the expected nanostructures. These issues can be alleviated by implementing the AFM probe-based dynamic plowing lithography (DPL) process, where the cantilever of the AFM probe can be driven to oscillate in the vertical direction at a high frequency, and the tip interacts with the sample surface many times in a short period. More specifically, the intermittent contact between the tip and sample in this method could

reduce the interaction force, which can result in reduced tip wear (Jin and Unertl, 1992). In AFM probe-based DPL, the material is mainly removed by extrusion with each stroke rather than through material shearing, as is the case in scratching. This mode of operation can also weaken the influence of the lateral force between the tip and sample on the variation of cantilever deflection (Yan et al., 2016). A research group at Harbin Institute of Technology has conducted a comprehensive series of studies in AFM probe-based DPL (He et al., 2017; He et al., 2017; He et al., 2018; Xiao et al., 2019). However, as the next section will demonstrate, there is still scope for conducting further numerical simulation research in AFM probe-based DPL.

Although complex features can be fabricated with AFM probe-based mechanical machining in a cost-effective manner and relatively easily, a current research issue affecting its wider utilisation is the lack of accurate simulation tools to quantitatively predict the process outcomes, especially in terms of dimensions of processed grooves as a function of process parameters. In general, despite the fact that micro and nano-scale machining share some similarities with macro-machining in terms of basic principles, there are still some significant differences. For example, micro and nano-scale machining is subject to the size effects (Woon et al., 2008). According to the definitions reported above, when depths of cut are at the level of micrometre or nanometre, these are normally smaller than the average grain size of the workpiece material and several orders of magnitude smaller than those of traditional macro-scale machining. Another difference between machining at such different scales is the potential mechanisms of material deformation (Sun and Cheng, 2010). Since the depth of cut in micro and nano-scale machining is comparable with the tool edge radius, the large negative rake angle of cutting tools can no longer be neglected, and the effect of ploughing may become important. A significant sliding along the tool flank face may also be observed for small-scale cutting due to the elastic recovery of the workpiece material, while, in traditional macro-scale machining, shear and friction are the dominant modes of material deformation.

To conclude this section, a brief framework for different micro and nano-scale mechanical machining processes is presented in Fig. 2.1, with the aim of summarising different engineering science aspects involved in these techniques and illustrating their underlying intricate relationships. Table 2.1 illustrates the descriptions for different micro and nano-scale mechanical machining processes mentioned earlier in this section. Although these cutting processes share a lot of common characteristics, they vary in workpiece shape, workpiece size, cutting tools, applications and other aspects. In Fig. 2.1, micro and nano-scale mechanical machining mechanics are central to the study of different micro and nano-scale mechanical machining processes. This is because micro and nano-scale mechanical machining is not a simple down scaling of traditional macro mechanical machining and it introduces some critical issues that fundamentally differ from those encountered in conventional macro machining, such as cutting forces, material deformation mechanisms, size effects, stress distribution and surface generation.

Among these aspects of micro and nano-scale cutting mechanics, the size effects play a significant role in explaining distinct machining phenomena at the micro and nano scale and have strong influences on other aspects of micro and nano-scale cutting mechanics. The size effects in micro and nano-scale cutting mechanics are categorised into three groups – micro structure size effect or grain size effect, cutting edge radius size effect and material properties size effect. The micro structure size effect takes place when the depth of cut at the micro and nano scale is comparable to the grain size of the machined material, which typically varies from 100 nm to 100 μm (Cheng and Huo, 2013). In this condition, the chip formation may take place inside the individual grain and thus the workpiece material cannot be treated as isotropic and homogeneous like in traditional macro machining. The material properties size effect occurs when a feature's minimum structural dimension decreases to the scale of a few microns or less. Under this circumstance, the initiation and propagation of dislocations inside the workpiece material can be influenced by geometrical constraints such as

grain boundaries, defects and surfaces. As a result, this dislocation mobility can affect the plastic deformation and thus change material properties at the micro and nano scale. The cutting edge radius size effect arises when the edge radius of the cutting tool is on the same order of amplitude as the depth of cut or the grain size. In such cases, the effective rake angle of the cutting tool may become highly negative, which thus significantly influences the chip formation and material deformation mechanisms. Another important issue closely related to the cutting edge radius size effect is the minimum chip thickness, which is the smallest depth of cut that will result in chip formation. The influence of minimum chip thickness needs to be incorporated into various models of cutting forces and material deformation mechanisms at the micro and nano scale. The cutting edge radius size effect is also exhibited in tool-workpiece contact at the flank face. When the tool edge radius cannot be ignored in micro and nano-scale cutting, the elastic recovery occurs and a friction force is introduced by ploughing or sliding between the flank face and workpiece. These aspects of tool-workpiece contact (elastic recovery and friction force) at the flank surface cannot be ignored in the cutting force modelling at the micro and nano scale.

It is highlighted that various mechanics aspects of micro and nano-scale mechanical machining detailed above are central to the study of micro and nano-scale mechanical machining. On the one hand, different modelling and simulation methods have been developed to assist the scientific understanding of various mechanics aspects of micro and nano-scale mechanical machining, with the aim of improving the reliability and predictability of the micro and nano-scale mechanical machining process. On the other hand, these engineering science aspects in micro and nano-scale cutting mechanics and their underlying intricate relationships have driven the progress of modelling and simulation techniques and provide foundation for modelling and simulation development, which will be reviewed in detail in the next section.

Table 2.1. Descriptions for different micro and nano-scale mechanical machining processes. (Cheng and Huo, 2013; Yan et al., 2015)

	Description
Single point diamond turning	Creating rotational parts of both spherical and aspheric surface, normally with low aspect ratios, through commercially available ultra-precision machine tools. Focusing on achieving highest possible dimensional accuracy and surface finish using single crystal diamond as the cutting tool.
Micro turning	Producing 3D micro cylindrical or rotational symmetrical components with high aspect ratio, typically through micro turning machines.
Micro milling	Fabricating freeform and complex 3D micro-structures and micro features with both convex and concave shapes and high aspect ratios. Achieved by mechanical interaction between a rotating micro cutter and workpiece, causing shearing of the material along defined tool paths and removal of unwanted material in the form of chips.
Micro drilling	Creating round holes through or blind and capable of machining deep holes.
Micro grinding	Producing high dimensionally accurate 3D micro components with convex and concave shapes and superior surface finishes, normally used as the final production procedure. Achieved by repeated penetrating, rubbing and scratching of abrasive grits on the workpiece material (capable of machining brittle and hard materials) at a relatively high speed.
AFM-based mechanical machining	Employing the AFM tip as the cutting tool to penetrate and scratch the sample surface to realise nano-scale mechanical removal of materials.

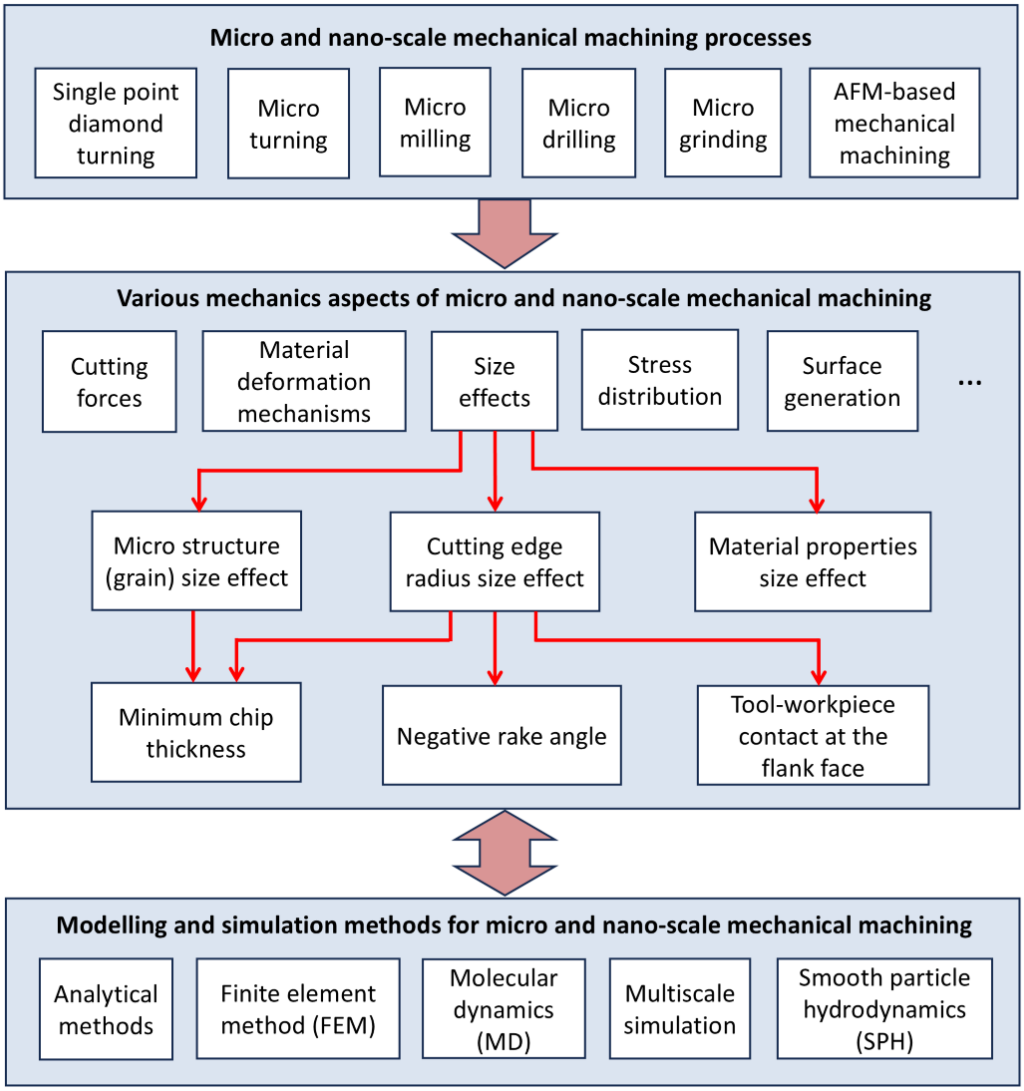

Fig. 2.1. A brief framework for micro and nano-scale mechanical machining processes and involved engineering science aspects.

2.3 Methods for the simulation of micro and nano-scale mechanical machining

As mentioned above, small scale mechanical machining can be employed to fabricate complex features and process various engineering materials, compared with other commonly used vacuum-based manufacturing technologies. At the same time,

mechanical machining at small scales needs an in-depth understanding of associated phenomena and mechanics, as this process should be distinguished from conventional macro-scale mechanical machining. Some research efforts in this field rely on extensive experimental work (Geng et al., 2016) to understand process mechanics and optimise cutting parameters. However, such experimental tests are not only expensive but also labour-intensive and time-consuming due to the required careful preparation of samples. In addition, these experimental tests provide limited insight into machining phenomena and limited scope for predicting the machining response when new processing conditions are introduced and required.

Therefore, in addition to experimental investigations, theoretical studies should be performed to characterise the micro and nano-scale mechanical machining in order to improve the reliability and predictability of the process. Anand and Patra (2014) reviewed the state-of-the-art modelling and simulation techniques in mechanical micro-machining. Markopoulos et al. (2020) presented a review of the most commonly used meshless methods in machining and micro-machining modelling. In this section, some modelling methods commonly used in the simulation of micro and nano-scale mechanical machining are reviewed.

2.3.1 Analytical methods

For predicting the surface generated by a cutting tool at a small scale through analytical approaches, the main objective is to calculate intersection points or profiles between consecutive tool paths in the tool feed direction. An early effort in this area was presented by Cheung and Lee (2000), who developed a model of the single point diamond turning process to predict the surface topography in the feed direction of machined parts. In the developed model, the real tool path was determined by taking into account the feed rate and the tool-workpiece vibration. The surface generation process was modelled by geometrically transferring the tool profile onto the

workpiece along this tool path. However, in this model, only the vibration caused by spindle axial error in the infeed cutting direction was considered and thus, the tool-workpiece vibration was assumed to be a simple harmonic motion. A few years later, following the modelling philosophy reported by these authors, Luo et al. (2005) developed a more complex model of the precision turning process by introducing some nonlinear factors, such as time-dependent cutting forces, cutting tool characteristics and regenerative chatter into the characterisation of dynamic tool-workpiece vibrations. In a subsequent research investigation, Zhou and Cheng (2009) further refined this approach by proposing an integrated micro and nano-scale cutting model, where a number of additional nonlinear factors associated with the workpiece material, cutting process and machine tool performance were considered. Size effects, which are responsible for the discrepancy between the achieved roughness and the kinematic roughness, should be an important consideration in modelling micro and nano-scale mechanical machining. In particular, some researchers have investigated the influence of mechanical properties of the workpiece material and some machining phenomena associated with size effects on surface generation. For example, Liu and Melkote (2006) paid particular attention to the plastic side flow of the machined material in micro turning. In the reported work, the authors presented a model for assessing and quantifying the influence of plastic side flow on surface roughness by considering the strain gradient strengthening of processed materials. However, the accuracy of this model could be further improved by taking into account other machining characteristics associated with size effects. In particular, in addition to plastic side flow, Vogler et al. (2004) considered the contribution of the minimum chip thickness effect in the surface generation model of micro milling. In particular, the authors proposed a predictive model to estimate the surface profile, and thus the surface roughness, achieved in the feed direction when cutting single-phase materials with micro milling by taking into account the geometric effect and the minimum chip thickness effect. It should be noted that, in this model, the predicted surface roughness value of a multiphase material in micro milling was approximated by the

weighted average of those of all the single phases within the material. However, from a theoretical perspective, there is no a priori reason to make this approximation. Thus, the surface generation model in this work could not be directly applied to multiphase materials until the accuracy of this approximation had been validated. To overcome this issue, more recently, Elkaseer and Brousseau (2013) proposed a novel modelling approach to predict the surface roughness generated in AFM-based nano-machining, where the heterogeneity of a workpiece material was taken into account. Figure 2.2 illustrates this analytical model to determine the intersection points between two adjacent profiles based on the tip edge radius and the step-over. Compared with the model developed by Vogler and co-workers, the complementary work in this study consisted of 1) the inclusion of the elastic recovery characteristic of the workpiece material in addition to the minimum chip thickness effect and 2) the adaptation of an image processing technique to identify the type of the processing phase. Despite the ability of this model to predict the generated roughness for multiphase materials, its accuracy could be further improved since it did not take into account plastic side flow, the initial topography of the workpiece, as well as the burr formation effect at the phase boundaries which was reported in (Vogler et al., 2004).

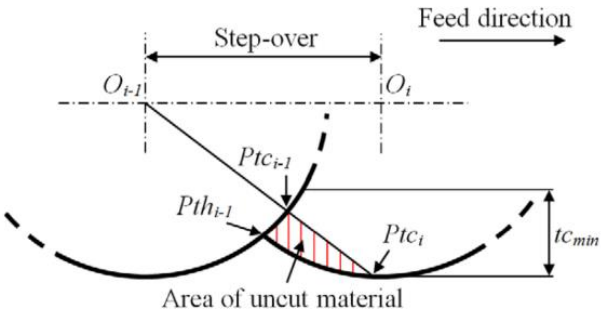

Fig. 2.2. Surface generation calculated by the analytical method during AFM probe-based machining. (Elkaseer and Brousseau, 2013)

There are mainly two common limitations associated with the above analytical modelling approaches for micro and nano-scale machining. Firstly, the accuracies of these models are relatively limited. Indeed, with a few exceptions excluded, the

minimum prediction error of these models reported in (Cheung and Lee, 2000; Luo et al., 2005; Liu and Melkote, 2006; Vogler et al., 2004; Elkaseer and Brousseau, 2013) is still more than 10%. This is partly due to the construction of layers of assumptions and simplifications and the adoption of some classical cutting models at the macro level. Secondly, these models essentially aim to predict the produced surface topography and, thus, provide limited insight into the machining characteristics associated with the process, such as chip formation, stress distribution, and cutting forces. A way around these limitations is to employ a numerical simulation approach to model the process. Numerical simulations can predict a wider number of machining outcomes with less simplifying assumptions and enable the understanding, or even the discovery, of new machining phenomena. Consequently, several numerical modelling techniques that have been employed to simulate micro and nano-scale machining are presented in the following sections.

2.3.2 Finite element method

Some researchers have focused on modelling micro and nano-scale mechanical machining through the conventional mesh-based finite element method (FEM), which is currently one of the widely used methods in numerical simulations. For example, Chuzhoy et al. (2002, 2003) modelled the ductile iron machining process in the main cutting direction by using FEM. More specifically, this FEM model enabled 1) the simulation of the micro-scale mechanical properties of heterogeneous materials, as well as the material flow and fracture during machining and 2) the provision of insights into some machining phenomena, such as chip formation, cutting forces, as well as strain and stress distributions within the sample. Youn and Kang (2005) employed a FEM model to study the tip effect and indentation size effect on the deformation behaviours (piling-up, sinking-in, and elastic recovery) of hard-brittle materials, such as amorphous silicon and Pyrex 7740 glass. Using the Abaqus software, Woon et al. (2008) investigated the chip formation mechanism and its corresponding stress states of AISI 4340 steel with FEM. Mabrouki et al. (2008) simulated orthogonal micro-cutting

on aluminium alloys with FEM to gain a deeper understanding of the physical phenomena accompanying chip formation. This FEM model proposed a coupling between material damage and fracture energy using the Abaqus software. Flórez Garcia et al. (2020) carried out a finite element analysis of orthogonal machining process to investigate the mechanical response of S235 carbon steel for different vibration-assisted cutting conditions. Wang et al. (2020) performed a FEM simulation of nano-scratching on a typical hard-brittle material (optical glass BK7) to study the stress distribution, which helped understanding the lateral cracks initiation and thus, the surface deformation and material removal mechanism of such material. Fu et al. (2021) established a 2D FEM model for orthogonal micro-machining to simplify the cutting of epoxy-based material using the Abaqus software. In this FEM model, the minimum undeformed chip thickness was 2 μm, which was comparable with the cutting edge radius (0.5-2.5 μm). Similar to the work of Fu and co-workers, Kurniawan et al. (2021) established a 2D FEM model of ultrasonic elliptical vibration cutting on AISI 1045, in which the cutting tool oscillated according to an inclined elliptical shape. It should be noted that the minimum depth of cut (10 μm) was within the same order or magnitude of that of the element sizes (1-10 μm) in this FEM model, which is a distinguishing feature in comparison to the conventional cutting process. Shi et al. (2021) established a polygon SiC particles model with a high-volume fraction to investigate the SiC particles crushing under different ultrasonic-assisted milling conditions. It should be noted that the SiCp/Al composites with reinforced phase SiC particles were represented by two different constitutive models. More specifically, the aluminium alloy 6061 and SiC particles were described with the Johnson-Cook model and the Johnson-Holmquist ceramic model, respectively. It should also be noted that the depth of cut (2-6 μm) in the FEM simulations was smaller than the average size of the SiC particles (45 μm). Oymak et al. (2021) established a micro-orthogonal cutting FEM model to simulate micro-milling of Ti6Al4V alloy. The authors presented how cutting temperature, forces and chip formations evolved during the FEM simulations. The Johnson-Cook plasticity failure criterion was also used to observe the chip removal.

The FEM simulations efforts reported above are also listed in Table 2.2.

Table 2.2. Recent development of FEM simulation for micro and nano-scale mechanical machining.

Topic of research work	Authors and year	Remarks	Minimum depth of cut
Residual stress distribution and load-displacement relation	Youn and Kang (2005)	Nano-indentation simulations were performed for various tip radii, half-angle of conical indenter, and indenter geometries to predict the nano-deformation behaviours of hard-brittle materials.	0.1 μm
Chip formation and stress distribution	Woon et al. (2008)	The invalidity of assuming perfect tool sharpness in the modelling of micromachining is proven based on chip formation behaviour and the associated stress states as the undeformed chip thickness approaches the tool edge radius.	0.1 μm
Physical phenomena accompanying chip formation	Mabrouki et al. (2008)	A failure damage model, which included two steps, namely damage initiation and damage evolution, was exploited based on the Johnson-Cook law to simulate chip formation.	300 μm
Effect of vibration-assisted cutting conditions	García et al. (2020)	The effects of different tool trajectories and cutting conditions (e.g. cutting speed, cutting feed, vibration frequency, depth of cut) on the mechanical response of the vibration-assisted cutting process in S235 carbon steel were investigated.	200 μm
Stress distribution analysis	Wang et al. (2020)	The crack initiation and propagation behaviour and its dependence on scratch directions were investigated by the stress field distribution.	0.5 μm
Chip formation and strain distribution	Fu et al. (2021)	Three different chip shapes were obtained, and the epoxy-cutting deformation mechanism was revealed.	2 μm

Cutting force and stress distribution	Kurniawan et al. (2021)	The cutting forces, tool temperature, and residual stress in ultrasonic elliptical vibration cutting are examined.	10 μm
Cutting force and kinematics of cutting edge	Shi et al. (2021)	The microscopic morphology, cutting force and surface roughness of the SiCp/Al composites during machining under different ultrasonic milling parameters were explored.	2 μm
Effect of different cutting conditions	Oymak et al. (2021)	The effects of cooling methods on cutting temperature, tool wear, strain and stress distribution, chip formations, and cutting forces were studied.	1 μm

In spite of the fact that the FEM method has been widely used in the simulation of micro and nano-scale mechanical machining, this approach still has the following inherent drawbacks which affect its accuracy.

First, the meshing strategy is an essential factor influencing the FEM simulation results. FEM has numerical difficulties when simulating problems where large deformations and even breakages occur, as is typical in mechanical machining. More specifically, adaptive mesh refinement or re-zoning techniques are required in such cases to avoid the generation of a highly distorted mesh. However, such mesh re-zoning procedures may be non-trivial and time-consuming and may introduce additional inaccuracies into the model. Indeed, the FEM model developed in (Chuzhoy et al., 2003) was re-meshed and re-zoned ninety times within a length of cut of 720 μm. In addition, at micro and nano scales, creating a mesh that is fine enough to represent the individual grains and their boundaries inside the workpiece material can be computationally intensive and may not be practical.

Second, most engineering materials used are polycrystalline materials with typical grain size varying from approximately 100 nm to 100 μm, which are comparable in size to the minimum depths of cut reported in Table 2.2 (ranging from 0.1 μm to 300 μm).

Under these circumstances, the chip formation may take place inside the individual grain and the micro structure size effect occurs. The workpiece material can no longer be assumed as homogeneous and isotropic like in conventional macro cutting. However, the FEM method may not accurately capture the micro structure size effect due to the following reasons. (1) The FEM method may not incorporate the necessary microstructural features or the correct constitutive models to accurately simulate the anisotropy or the non-homogeneity of the material. (2) The effects of grain boundaries inside the workpiece material cannot be neglected when the depth of cut is in the same order as the material grain size. Grain boundaries can influence the flow of material during machining, affecting the stress distribution and the chip formation. The FEM may not adequately represent these effects, which may result in inaccuracies in the simulation results. Therefore, the FEM has shortcomings when it comes to simulating micro and nano-scale mechanical machining because the FEM may not be able to accurately simulate the micro structure size effect and the grain boundary effects which are significant at this scale.

The above drawbacks of the mesh-based FEM approach when simulating micro and nano-scale machining can be addressed using mesh-free particle-based methods (MPMs) (Liu and Liu, 2003), for which the specimen and the cutting tool can be represented by a set of discrete particles, instead of a continuous mesh. MPMs exhibit the following attractive features for modelling micro and nano-scale machining. First, MPMs simplify the discretisation of the specimen and the cutting tool since only an initial particle discretisation is required. Second, MPMs can easily handle problems with large deformations since refinement of particles is more easily performed than mesh refinement. Third, many MPMs approaches can be applied to discrete systems due to their particle nature. More specifically, many MPMs are initially developed for systems with discrete particles, and the material workpiece during micro and nano-scale machining may be regarded as a discrete solid due to the size effect. Finally, due to the fact that most MPMs are inherently Lagrangian, following the material

deformation and separation in time to study different machining phenomena becomes easier. Due to these advantages, some researchers have already attempted to model micro and nano-scale machining using MPMs. In particular, Molecular dynamics (MD), an atomistic-scale MPM based on force potential functions, has been widely used among these methods.

2.3.3 Molecular dynamics

The basic principles of MD simulation for nano-machining can be described in Fig. 2.3. The nano-machining system comprising the cutting tool and the workpiece is represented by its atomistic structure. The workpiece is divided into three zones: the Newtonian atoms zone, the thermostat atoms zone and the boundary atoms zone. The boundary atoms are assumed to be unaffected by the indentation and scratching process. The motions of the thermostat atoms are modified by the method of velocity reset. The atoms of the Newtonian zone can move freely under the influence of interatomic forces produced by potential functions, such as the Morse function or the Embedded Atom Model (EAM) function. The interatomic forces can be derived from the differentiation of the potential function, and the motions of individual atoms are usually assumed to be governed by Newton's second law. Atomistic forces, temperatures, stresses and subsurface damage can be determined after the simulation. MD simulations are limited to nanometer size cutting lengths. It should be noted that MD deals with problems at the molecular or atomic scale. On this scale, a solid material workpiece can no longer be viewed as a continuum. Therefore, conventional continuum mechanics cannot apply, and the assumptions made by continuum mechanics-based methods, such as FEM in the previous section, are no longer valid.

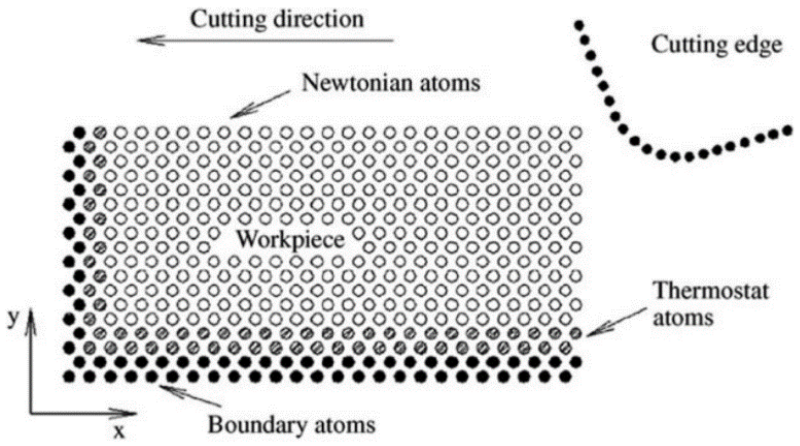

Fig. 2.3. MD simulation model of nano-scale cutting process. (Cai et al., 2007)

MD has been successfully applied by researchers to investigate a variety of process outcomes in nano-scale mechanical machining. For example, Geng et al. (2015) have performed MD simulations to study nanometric cutting phenomena. In particular, using MD simulation, Geng and co-workers theoretically observed that dislocation slip is the dominant material deformation mechanism when sliding a diamond three-sided pyramidal AFM tip over a single crystal copper surface. Maekawa and Itoh (1995) simulated orthogonal nano-machining of copper using MD simulation with a specific focus on friction and tool wear. It should be noted that the tool wear in the MD model was simulated by reducing the cohesion energy of carbon atoms. More specifically, the tool wear mechanism consisted of the interdiffusion of tool and workpiece atoms and the re-adhesion of worn particles to the tool. Similar to the work reported by Maekawa and co-workers, Zhang and Tanaka (1997) established a two-dimensional MD model for a diamond-copper sliding system to investigate the mechanisms of wear during atomic sliding. In addition, authors highlighted the similarity and differences between atomic and micro analyses of deformation mechanisms (i.e. dislocation motion and slip-line distribution). Therefore, further work is required to bridge the gap between atomic analysis and micro-scale analysis that use continuum mechanics. Cheng et al. (2003) carried out MD simulations to simulate the nano-cutting of a single crystal silicon plate and investigated the wear mechanism of the diamond tip. In their

simulations, tool wear was modelled by interactions between the workpiece atoms and cutting tool atoms and could therefore be studied by analysing the loci of these atoms. The wear mechanism was also investigated by considering the effect of cutting heat, cutting temperature and the stress in the diamond tip. Fang et al. (2005) established a MD nano-cutting model on a typical brittle and hard material monocrystalline silicon and studied its nano-scale cutting mechanism. The simulation results showed that the material removal mechanism at the nano-scale was based on extrusion. The authors believed this model would also be suitable for metallic materials because they showed ductility when the undeformed chip thickness was on the nano-scale. Lin and Huang (2008) employed MD simulations to predict the cutting forces during nano-cutting of a single crystal copper workpiece. In their work, a nano-scale contact pressure factor (NCP factor) was proposed to compensate for the inconsistent scale between conducted AFM experiments and MD simulations when predicting the cutting forces. Hosseini et al. (2011) performed MD simulations of nano-scale cutting on single-crystal copper. The distribution of dislocation in the workpiece was simulated by MD and used as a criterion of the machined surface deformation to study the effects of tool geometry on cutting forces and chip formation. Karkalos et al. (2018) investigated the effect of cutting depth and material properties on cutting forces using MD simulation of nano-machining of nickel and iron. Similar work was found in (Markopoulos et al., 2018; Karkalos and Markopoulos, 2019), where Markopoulos and co-workers developed a MD model for nanometric face milling and several characteristics of this process, such as the cutting forces and chip morphology, were investigated. Xu et al. (2019) performed MD simulations on nano-scratching to represent the nano-grinding of a Cu-Si model. It should be noted that the phase transition of Cu and dislocation evolutions inside Cu were investigated in detail by MD. Based on this atomic scale information, the effects of the grinding speed and depth on the workpiece temperature and grinding forces were analysed. Using MD simulation, Zhao et al. (2021) investigated the defect interactions of the nano-crystalline materials during nano-cutting. In particular, the interaction mechanism between grain

boundaries and microstructures in nano-cutting of nanocrystalline copper, as well as its effect on mechanical response (such as surface topography, cutting forces, stress and temperature distribution), were investigated based on the atomic motions and interactions. It should be noted that the MD model in these authors' work could model grain boundary networks, grain shape and size, crystal orientation, defect evolution, displacement of workpiece atoms and Von Mises stress distribution. The MD simulations studies of nano-scale mechanical machining that were presented above are also listed in Table 2.3.

Table 2.3. Recent development of MD simulation for nano-scale mechanical machining.

Topic of research work	Authors and year	Remarks	Machining length
Friction and tool wear	Maekawa and Itoh (1995)	The influence of the friction and tool wear in the nano-scale machining on the cutting mechanism was similar to that observed in the macro-scale machining.	12 nm
Atomic-scale wear and friction	Zhang and Tanaka (1997)	Four distinct regimes of deformation in an atomic diamond-copper sliding system were revealed: the no-wear regime, adhering regime, ploughing regime and cutting regime. The transition between different deformation regimes was governed by indentation depth, sliding speed, asperity geometry and surface lubrication conditions.	300 nm*
Diamond tool wear	Cheng et al. (2003)	Thermo-chemical wear was the basic wear mechanism of the diamond tip of an atomic force microscope (AFM).	2 nm
Undeformed chip thickness in nanometric cutting	Fang et al. (2005)	The mechanism of nanometric scale material removal was based on extrusion rather than shearing in conventional machining.	12 nm

Cutting forces	Lin and Huang (2008)	The heaping of copper atoms in MD simulations and comparisons of simulated and experimental cutting forces demonstrated the accuracy of the proposed estimation model of cutting forces during nano-cutting.	3.84 nm
Effects of tool geometry on nano-machining	Hosseini et al. (2011)	A sharp tool with no edge radius and a variety of edge radii with specific rake and clearance angles were compared in terms of tool forces, coefficient of friction and distribution of dislocation based on the distribution of dislocation in the machined workpiece.	6 nm
Cutting forces	Karkalos et al. (2018)	The effect of cutting depth and material properties on cutting forces during nano-milling was investigated.	3 nm
Cutting force and chip formation	Markopoulos et al. (2018)	The effects of cutting tool geometries and feed values on chip morphology and cutting forces were presented.	7 nm
Cutting forces	Karkalos and Markopoulos (2019)	Effects of cutting conditions, such as feed rate and cutting speed, on cutting forces and subsurface damage was conducted.	
Effects of machining parameters on machining forces and temperature	Xu et al. (2019)	The effects of grinding depth, speed, and Cu thickness on material removal, defects, grinding forces, and temperature were analysed based on atomic-scale dislocations and phase transitions.	22 nm
Micro-structure evolution	Zhao et al. (2021)	The plastic deformation and surface generation mechanisms of copper were investigated based on the atomic motions and interactions.	30 nm

* A two-dimensional MD analysis was used in this paper.

Despite the ability of MD approaches to study nano-scale machining phenomena, the main limitation of MD simulations is that the length of cut commonly investigated is very short due to the high computational power required. For example, the maximum machining length among all MD simulations reported in Table 2.3 is found to be 30 nm. This is less than the typical dimension of features cut via nano-scale machining. In addition, the accuracy of MD simulations depends on the accuracy of the potential functions utilised for computing interatomic forces.

As two popular numerical modelling techniques for micro and nano-scale machining, FEM and MD have their respective advantages and limitations. For example, MD simulation can be used to describe and understand nano-scale mechanics and phenomena; however, it can only cover machining responses over restricted lengths because of the computational cost. On the other hand, FEM simulation is suited for modelling meso and macro scale machining, although micro-scale information such as the microstructure evolution during plastic deformation can be difficult to be captured.

In this context, multiscale simulations have been developed to bridge the gap between the MD and FEM simulation. They could achieve a reasonable compromise between computational efficiency and accuracy at the micro/nano scale. For example, such multiscale approaches have been conducted in the field of nano-indentation. In order to obtain a deeper understanding of the mechanics of plastic nano-indentation, researchers have also carried out multiscale simulations by combining the advantages of the above modelling approaches at different length scales. For example, Chang et al. (2010) investigated multiscale simulations of nano-indentation on copper from the atomic scale to continuum scale. In their study, MD simulations provided details of the dislocation nucleation mechanism at the atomic scale. This information was then incorporated as sets of local rules and passed on to discrete dislocation dynamics (DDD) models that could simulate dislocation propagation. At the continuum scale, DDD simulations were used to compute coefficients in constitutive equations for crystal

plasticity finite element models, which were performed and directly compared with AFM observations. Sun and Cheng (2010) conducted multiscale simulation of nanometric cutting of single crystal aluminium based on the Quasicontinuum method, which is characterised by the combined MD-FE technique. In this study, the chip formation, generation, propagation of atomic dislocations and other cutting physics aspects during the nanometric cutting process were comprehensively examined to investigate the effect of the rake angle on the cutting force and internal stress. Wang et al. (2008) also performed multiscale simulations of nano-indentation on Ni (100) thin film by coupling MD and FEM. Such multiscale modelling approaches can overcome the barriers of individual simulation techniques and bridge the gap between these methods at different length scales. Thus, it is a promising research area for the study of nano-indentation. It is important to note that at the higher length scale of such multiscale approaches, FEM is currently the primary technique employed by researchers studying nano-indentation. However, it could be argued that an alternative approach to FEM, which is typically more suitable for the simulation of large strains and strain rates, could also be of interest for the study of nano-scale deformation phenomena, while still relying on constitutive models informed by atomistic-based, dislocation-based and/or microstructure-based effects. One of such approaches is Smooth Particle Hydrodynamics (SPH) method which will be the focus of next section.

2.3.4 Smooth Particle Hydrodynamics

In order to avoid the above-mentioned limitations of MD simulation while still benefiting from MPMs, it would be advantageous for researchers to find alternative MPM with which the investigated length scale can reach several hundreds of nanometers or several tens of micrometres. One very promising MPM that can potentially meet this requirement is Smooth Particle Hydrodynamics (SPH) (Liu and Liu, 2003).

SPH is a Lagrangian MPM that can be applied to problems at different scales. For example, since its first invention to solve astrophysical problems (Gingold and Monaghan, 1977), the SPH method has been extensively studied and applied to a vast range of scenarios in engineering and science ranging from macro-scale, such as fluid dynamics related problems (Kulasegaram et al., 2004), fracture of brittle solids (Benz and Asphaug, 1995), metal forming (Bonet and Kulasegaram, 2000), high velocity impacts (Johnson et al., 1996; Randles et al., 1995) and explosion problems (Liu et al., 2003), to atomistic-scale simulations (Liu et al., 2002; Nitsche and Zhang, 2002). Thus, the SPH method demonstrates the potential to be a robust approach to model micro and nano-scale mechanical machining. As illustrated in Fig. 2.4, when using the SPH method for this purpose, the processed specimen is discretised into a set of SPH particles, which possess all the individual material properties and deform or move according to the governing conservation equations. The topographical modification of the sample surface is simulated by the collective movement of those SPH particles.

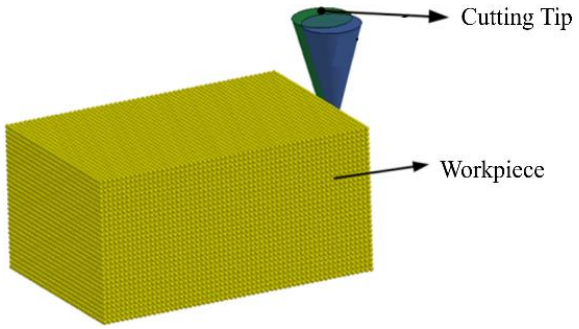

Fig. 2.4. SPH model of micro and nano-scale mechanical machining. (Takabi et al., 2017)

The avenues investigated by SPH simulations of small scale machining can be summarised as at least the following four aspects from the current literature. First is the study of chip formation, cutting forces and tool wear. For example, Zhao et al. (2014) established a micro-machining model on OFHC copper using the SPH method in LS-DYNA software. In this work, the influence of residual stress on subsequent micro-machining process was studied by comparing the chip shape and cutting forces

under different cutting depths. Similar to Zhao's work, Geng et al. (2017) established an orthogonal micro-machining model on OFHC copper using SPH with the LS-DYNA software. The effects of the friction coefficient between the tool and workpiece on cutting forces and chip morphology were studied. It should be noted that the Johnson-Cook model was employed to describe the workpiece in these SPH simulations. Guo et al. (2020) applied the SPH approach to model micro-machining of industrial pure iron. The mechanism of chip formation and its dependence on tool edge radius were discussed by analysing the chip morphology and tracing the displacement trajectories of the SPH particles. Other research studies that focus on these specific process characteristics can also be found in (Calamaz et al., 2009; Madaj and Píška, 2013; Xi et al., 2014; Stenberg et al., 2017).

A second focus is the study of the surface generation mechanism and residual stress distribution. For example, Duan et al. (2017) established a 3D SPH model for single diamond micro-scratching on monocrystal SiC. The influence of different diamond shapes on material removal modes of SiC was analysed and the stress distribution was studied through SPH simulations. Gouskov et al. (2018) simulated nano-machining on Potassium dihydrogen phosphate (KDP) crystal based on the SPH method. The roughness of the machined surface and the distribution of the von Mises stress were studied by introducing a scalar plasticity measure. Li et al. (2021) established a single grain scratching SPH model to study the subsurface damage of optical quartz glass. The generation and propagation of subsurface cracks were studied in detail by analysing the stress distribution during the scratching process and combining it with the scratch elastic stress field model. Other SPH-based research works that investigated the surface generation mechanism and residual stress distribution can be found in (Zhao et al., 2013; Cao et al., 2016; Shchurov et al., 2016).

Third is the study of machined surface profile and topography. For example, Leroch et al. (2016) simulated micro-scratching induced surface damage on OFHC copper using

a self-developed SPH algorithm, which included an explicit Velocity-Verlet time integration algorithm and a radial return plasticity algorithm. Using these algorithms, the simulated surface topography (i.e. profile, scratch depth and scratch width) was found to be in excellent agreement with experimental results. As a further work based on (Xu et al., 2019), Duan et al. (2017) established a subsequent nano-scale scratching model via SPH. In this work, the emphasis was placed on 3D grooves topography after double scratching and interference mechanisms. Another SPH-based research work that specifically focused on the study of the machined surface profile and topography can be found in (Varga et al., 2017). Zhang and Zong (2020) employed the SPH method to investigate the material removal mechanism of KDP crystal when the diamond tool had different types of tool-edge micro defects. The machined surface topography along the cutting direction was extracted to study the generated surface roughness..

The fourth topic is the effect of cutting conditions, such as tool geometries, material parameters and particle density, on micro and nano-scale machining. For example, Islam et al. (2012) simulated the nano-machining process on copper using an in-house SPH code. The effects of nano-machining conditions (i.e. depth of cut, tip rake angle, sliding friction coefficient) on material responses were systematically studied. It should be noted that these authors used an elasto-plastic model to describe the material behaviour of copper in contrast with the majority of other studies reported in this section. Similarly, Guo et al. (2017) established an SPH model for nano-machining on a copper workpiece with two tip shapes: the spherical capped conical tip and the regular three-sided pyramidal tip. The effects of nano-machining conditions (i.e. scratching speed, scratching depth, scratching direction, tip face angle) on material responses (i.e. chip formation and cutting forces) were investigated. Gu et al. (2018) investigated the effect of geometrical parameters of cutting tools on the ductile-brittle transition of sapphire in micro-machining using the SPH method. Other SPH-based research studies in this area of investigation can be found in (Rüttimann et al., 2013; Varga et al., 2017; Takabi et al., 2017; Zhong et al., 2017; Zhang et al., 2019).

The SPH simulations studies reported above for the micro and nano-scale mechanical machining are listed in Table 2.4.

Table 2.4. Recent development of SPH simulation for micro and nano-scale mechanical machining.

Topic of research work	Authors and year	Minimum cutting depth	Material	Material model
Chip formation, cutting forces and tool wear	Zhao et al. (2014)	50 nm	Oxygen-free high-conductivity (OFHC) copper	Johnson-Cook model (without failure model)
	Geng et al. (2017)	3 μm	OFHC copper	Johnson-Cook model (without failure model)
	Guo et al. (2020)	0.4 μm	Pure iron	Johnson-Cook model (without failure model)
	Calamaz et al. (2009)	300 μm	Ti6Al4V alloy	Johnson-Cook model (without failure model)
	Madaj and Piska (2013)	400 μm	A2024-T351 alloy	Johnson-Cook model (with failure model)
	Xi et al. (2014)	150 μm	Ti6Al4V alloy	Johnson-Cook model (without failure model)
	Stenberg et al. (2017)	300 μm	Steel	Johnson-Cook model (with failure model)
Surface generation mechanism and (residual) stress distribution	Duan et al. (2017)	15 μm	Monocrystal SiC	Johnson-Holmquist-Cook model
	Gouskov et al. (2018)	10 nm	KDP crystal	Multi-linear elastic-plastic model
	Li et al. (2021)	1 μm	Optical quartz glass	JH-2 model
	Zhao et al. (2013)	300 nm	OFHC copper	Johnson-Cook model (without failure model)
	Cao et al. (2016)	0.07 μm	SiC ceramics	Johnson-Holmquist model

	Shchurov et al. (2016)	10 μm	6061-T6 aluminium	Johnson-Cook model (with failure model)
Machined surface profile and topography	Leroch et al. (2016)	5 μm	OFHC copper	Johnson-Cook model (without failure model)
	Duan et al. (2017)	10 μm	Monocrystal SiC	Johnson-Holmquist-Cook model
	Varga et al. (2017)	25 μm	Metals	Johnson-Cook model (without failure model)
	Zhang and Zong (2020)	0.1 μm	KDP crystal	Multi-linear elasto-plastic model
Effect of cutting conditions (i.e. tool geometries, material parameters, particle density, etc) on micro/nano-machining	Islam et al. (2012)	100 nm	Copper	Elasto-plastic model
	Guo et al. (2017)	20 nm	OFHC copper	Johnson-Cook model (without failure model)
	Gu et al. (2018)	2 μm	Single crystal sapphire	JH-2 model
	Rüttimann et al. (2013)	8 μm	90MnCrV8	Johnson-Cook model (without failure model)
	Varga et al. (2017)	25 μm	Metals	Johnson-Cook model (without failure model)
	Takabi et al. (2017)	400 μm	Aluminium and cortical bone	Johnson-Cook model (with failure model) and elastic-plastic model
	Zhong et al. (2017)	1.19 μm	OFHC copper	Johnson-Cook model (without failure model)
	Zhang et al. (2019)	0.14 μm	KDP crystal	Piecewise-linear plasticity model

2.4 Identified knowledge gaps

Based on the presented literature review, this thesis focuses on the following three knowledge gaps.

- The first knowledge gap of interest in this thesis is concerned with investigating the feasibility of employing SPH modelling for simulating the nano-indentation process. In contrast to the relatively numerous studies on SPH simulation of micro and nano-scale mechanical machining, only one publication (Guo et al., 2015) was found on the SPH simulation of nano-indentation. In addition to being one of the most common techniques for the quantitative characterisation of materials, nano-indentation is also the first process step when conducting nano-scale machining with an AFM instrument. Therefore, this Thesis aims to demonstrate the potential of the SPH method to model the material response during nano-indentation. This feasibility study which is the focus of Chapter 4 lays the foundations for further SPH-based prediction and simulation works reported in later chapters.

- The second knowledge gap identified is concerned with comparing the influence of adopted material models on the material response during micro and nano-scale machining, with a specific focus on the predicted surface profile of machined grooves. On the one hand, from the review of existing SPH simulations of micro and nano-scale machining reported in Table 2.4, two different material models (i.e. the Johnson-Cook model without failure, the Johnson-Cook model with failure and the elasto-plastic model) were employed. It can be noticed from this table that the Johnson-Cook model without a failure criterion was the most commonly used material constitutive model. The SPH method suitably enables the simulation of material separation (Villumsen and Fauerholdt, 2008; Gallet and Lacome, 2002); thus, a failure-based model is not normally needed; However, as it was discussed in (Madaj and Píška, 2013), by implementing a failure criterion,

residual particle speeds change to values more realistic to the observed residual speeds. The Johnson-Cook model with failure would also have an influence on the considered machining responses. Therefore, the influence of the above-mentioned two material models on material responses during micro and nano-scale machining should be compared. On the other hand, it can be seen from Table 2.4 that only a few SPH simulations (Leroch et al., 2016; Varga et al., 2017) were concerned with the prediction of surface profile on metallic materials, which is an essential objective in the simulation of micro and nano-scale machining. Therefore, in Chapter 5, the influence of adopted material models on the material is compared with a specific focus on the predicted surface profile of machined grooves.

- The third knowledge gap of interest in this Thesis is concerned with the feasibility of employing SPH modelling to simulate the AFM probe-based dynamic ploughing lithography (DPL) process. DPL conducted with an AFM instrument is a promising mechanical machining technique for fabricating nano-scale surface structures. However, none of the SPH-based studies presented above focused on simulating this specific process. In Chapter 6 of this thesis, an attempt is made to simulate the AFM probe-based DPL process using the SPH method with a view to further reveal machining mechanisms and to predict the surface generation process.

Chapter 3 SPH implementation of micro and nano-scale tip-based material deformation

3.1 Overview

The main objective of this Chapter is to introduce the basic concepts behind the SPH method and the computer implementation of SPH models with the ANSYS/LS-DYNA software. To achieve the aim of this Chapter, the next section starts by discussing the strategy applied with the SPH method for solving partial differential equations (PDEs), which makes it a meshfree, adaptive and Lagrangian method for large deformation problems and solid mechanics problems such as micro and nano-scale mechanical machining. This section also presents some essential formulations of the SPH method, which include the continuous kernel approximation and the discretised particle approximation. These essential formulations illustrate how the SPH method converts the continuous representation of a function to the discretised particle summations based on an arbitrary set of particles. This makes SPH a simple numerical method without the need to use a background mesh. Following the presentation of the detailed procedure for kernel and particle approximations, the third section describes the computer implementation of SPH formulations in LS-DYNA which was carried out in this research. In this section, the SPH formalism is first extended to discretisation of the momentum conservation equation and energy conservation equation, and these formulations are already available in LS-DYNA. Then, the details of the contact model and material models employed in this thesis are also discussed in this section. The fourth section reports a convergence study conducted to investigate the influence of SPH particle density. This convergence study also serves as an introduction for the numerical simulations to be discussed in the following chapters. This section also presents the calculations of the essential dimensions of three types of diamond tips used for modelling material deformation in this thesis as this represents general information which is useful for the following chapters. The final section presents the concluding remarks of this chapter.

3.2 Introduction to the SPH method

3.2.1 Basic principles of the SPH method

As mentioned in Chapter 2, the SPH method is suitable for solid mechanics problems which are described in the form of partial differential equations (PDEs) of field variables, such as the energy, density and velocity. While obtaining analytical solutions for these PDEs is usually not feasible, the SPH method offers an alternative approach that does not rely on such solutions. This is because it relies on some key concepts to help achieve this task. With the SPH method, the problem domain is represented by a set of arbitrarily distributed particles, which determines the mesh-free nature of the SPH method. The integral representation, also named as kernel approximation in SPH, is used to approximate field functions. This integral representation is then further approximated using particles by replacing the integration term in the kernel approximation of the function with summations over all the corresponding values of the neighbouring particles in a particular domain. These particle approximations are performed on all variables in the PDEs to produce a set of ordinary differential equations (ODEs) with respect to time, which are relatively easier to solve. These basic principles make the method a mesh-free, adaptive, Lagrangian technique to model large deformation in solid mechanics problems.

The Lagrangian nature of the SPH method is explained as follows with some additional level of details, as this attractive feature of the SPH method allows the SPH particles to function as not only approximation points but also as material components. The SPH method is referred to as a ‘Lagrangian technique’ due to its intrinsic adherence to the principles of the Lagrangian description. The SPH method focuses on the motion of individual particles or material elements, which is the distinguishing feature of Lagrangian techniques. More specifically, in the SPH method, the SPH particles carry material properties (such as density, mass, momentum, and energy), and are allowed to move in light of the internal interactions and external forces. In addition, the particle

approximations in SPH are performed to all terms related to field functions in the partial differential equations to produce a set of ODEs in discretised form with respect to time only, by which the entire time history of all the field variables at a material point can be easily tracked and obtained. Therefore, the SPH method is in direct alignment with the Lagrangian technique, which is characterised by a material description that follows the motion of material components.

The formulation of the SPH method is divided into two steps. The first step is the kernel approximation of field functions. The second step is the particle approximation. In detail, since an arbitrary function can be represented in an integral form, the field functions are first re-written in the form of integral representation by introducing a smoothing kernel function. Next, the problem domain where the field functions are defined is discretised by a set of arbitrarily distributed particles. The kernel approximation is then performed by summing up the values of the nearest neighbour particles in a local domain called the support domain, which yields the particle approximation of the function at a point. The detailed formulation of the SPH method is presented in the following sub-sections.

3.2.2 Kernel approximation

The formulation of the SPH method starts from the following identity, which describes that a function $f(\boldsymbol{x})$ can be represented in an integral form.

$$f(\boldsymbol{x}) = \int_{\Omega} f(\boldsymbol{x}')\delta(\boldsymbol{x} - \boldsymbol{x}')d\boldsymbol{x}' \tag{3.1}$$

where f is a function of the three-dimensional vector $\boldsymbol{x}$, Ω is the integration domain which contains $\boldsymbol{x}$ and $\delta(\boldsymbol{x} - \boldsymbol{x}')$ is the delta function given by:

$$\delta(\boldsymbol{x} - \boldsymbol{x}') = \begin{cases} 1 & \boldsymbol{x} = \boldsymbol{x}' \\ 0 & \boldsymbol{x} \neq \boldsymbol{x}' \end{cases} \tag{3.2}$$

The concept of kernel approximation comes from replacing the delta function

$\delta(\boldsymbol{x}-\boldsymbol{x}')$ in equation (3.1) with a smoothing kernel function $W(\boldsymbol{x}-\boldsymbol{x}',h)$, and therefore equation (3.1) is rewritten as:

$$\langle f(\boldsymbol{x})\rangle = \int_{\Omega} f(\boldsymbol{x}')W(\boldsymbol{x}-\boldsymbol{x}',h)d\boldsymbol{x}' \tag{3.3}$$

where the angle bracket $\langle\ \ \rangle$ represents the kernel approximation operator in the SPH convention, W is the kernel function and h is the smoothing length that defines the influence area of W. This influence area is called the support domain of W at point $\boldsymbol{x}$. The "=" symbol is employed in equation (3.3) as it is the standard expression of the kernel approximation of a function, although the integral representation at the right hand side of equation (3.3) can only be an approximation.

In the SPH method, the kernel function $W(\boldsymbol{x}-\boldsymbol{x}',h)$ is not a unique kernel. In fact, any function satisfying the following properties can be employed as the kernel in the SPH method.

(1) Unity property. The integration of the kernel over its support domain should be equal to one.
(2) Compact support property. The value of the kernel function should be zero outside the support domain.
(3) Positivity property. The kernel function should be non-negative in the support domain.
(4) Decay property. The value of the kernel function for a concerned particle should be monotonically decreasing as the distance away from that particle increases.
(5) Symmetric property. The kernel function should be an even function.
(6) Smoothness. The kernel function and its derivatives should be sufficiently smooth.

So far, different kernels have been constructed following the above requirements by researchers, including the Gaussian kernel, the cubic spline kernel, higher order (quartic and quintic) splines kernel and the piecewise kernel. However, in the

traditional SPH method, for a given micro and nano-scale machining problem, the kernel function is unique and applicable for all the particles. Despite that particle-wise kernel function, which is not unique for a given problem and depends on the particle position, can be constructed to improve the accuracy of the particle approximation, its cost-effectiveness in computation needs to be considered.

Among the above-mentioned properties of the kernel function, the compact support property can be described by the following equation:

$$W(\boldsymbol{x}-\boldsymbol{x}',h)=0 \quad \text{when } |\boldsymbol{x}-\boldsymbol{x}'|>\kappa h \tag{3.4}$$

where κ is a constant which also defines the support domain of W at point $\boldsymbol{x}$. Using the compact support condition, integration over the entire problem domain is localised as integration over the support domain of W. This is very important considering the computation effort because problems with large deformation usually require a large number of particles to discretise the entire problem domain. The kernel function W is illustrated in Fig. 3.1, which will also be discussed later.

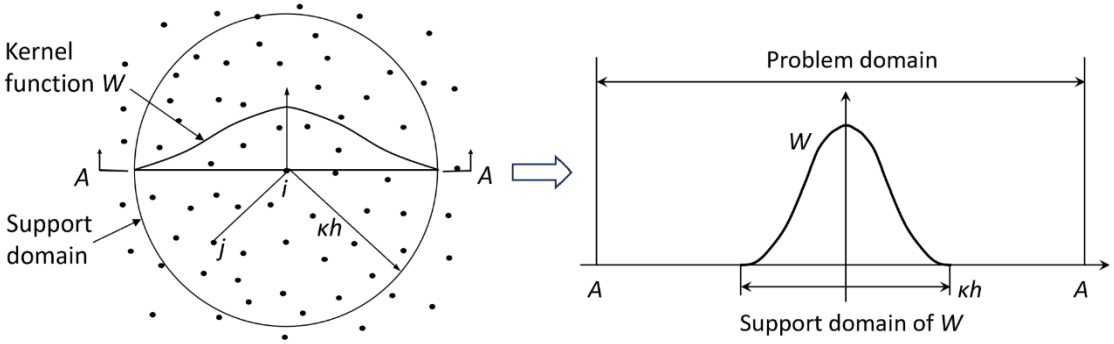

Fig. 3.1. Kernel approximation and smoothing kernel function in the SPH method. (partly adopted from (Liu and Liu, 2003))

The approximation for the derivative of $f(\boldsymbol{x})$ can be obtained by substituting $f(\boldsymbol{x})$ with $\nabla f(\boldsymbol{x})$ in equation (3.3) as follows:

$$\langle \nabla f(\boldsymbol{x}) \rangle = \int_{\Omega} [\nabla f(\boldsymbol{x}')] W(\boldsymbol{x} - \boldsymbol{x}', h) d\boldsymbol{x}' \tag{3.5}$$

where ∇ is the gradient operator. This is because f is defined as a function of the three-dimensional position vector $\boldsymbol{x}$.

Since

$$[\nabla f(\boldsymbol{x}')] W(\boldsymbol{x} - \boldsymbol{x}', h) = \nabla [f(\boldsymbol{x}') W(\boldsymbol{x} - \boldsymbol{x}', h)] - f(\boldsymbol{x}') \nabla W(\boldsymbol{x} - \boldsymbol{x}', h) \tag{3.6}$$

From equation (3.5), the following equation is obtained using integration by parts.

$$\langle \nabla f(\boldsymbol{x}) \rangle = \int_{\Omega} \nabla [f(\boldsymbol{x}') W(\boldsymbol{x} - \boldsymbol{x}', h)] d\boldsymbol{x}' - \int_{\Omega} f(\boldsymbol{x}') \nabla W(\boldsymbol{x} - \boldsymbol{x}', h) d\boldsymbol{x}' \tag{3.7}$$

The next step of transformation relies on the divergence theorem, which states that the volume integration of the divergence of a field over the region inside a closed surface is equal to the total outward flux of the vector field from that surface. Using the divergence theorem, the first volume integral over the support domain Ω on the right hand side of equation (3.7) can be converted into a surface integration over the surface *S* of the support domain Ω. This process is described as follows.

$$\int_{\Omega} \nabla [f(\boldsymbol{x}') W(\boldsymbol{x} - \boldsymbol{x}', h)] d\boldsymbol{x}' = \int_{S} f(\boldsymbol{x}') W(\boldsymbol{x} - \boldsymbol{x}', h) \cdot \vec{\boldsymbol{n}} dS \tag{3.8}$$

where $\vec{\boldsymbol{n}}$ is the unit vector normal to the surface S. From equation (3.7), the following equation is obtained.

$$\langle \nabla f(\boldsymbol{x}) \rangle = \int_{S} f(\boldsymbol{x}') W(\boldsymbol{x} - \boldsymbol{x}', h) \cdot \vec{\boldsymbol{n}} dS - \int_{\Omega} f(\boldsymbol{x}') \cdot \nabla W(\boldsymbol{x} - \boldsymbol{x}', h) d\boldsymbol{x}' \tag{3.9}$$

For those points whose support domain is entirely within the problem domain, the surface integration over the boundary *S* of the support domain will be zero because the kernel $W(x - x', h)$ is zero outside the support domain. This is due to the

compact support property of the kernel function. Therefore, equation (3.9) can be simplified as follows.

$$\langle \nabla f(\boldsymbol{x}) \rangle = -\int_{\Omega} f(\boldsymbol{x}') \nabla W(\boldsymbol{x} - \boldsymbol{x}', h) d\boldsymbol{x}' \tag{3.10}$$

For those points whose support domain intersects with the problem domain, necessary adjustments should be implemented to address the boundary effects if the surface integration is considered to be zero.

Equation (3.10) implies that the derivative of a function can be obtained by the derivative of the kernel function. More specifically, the kernel approximation of the derivative of a field function can be determined from the values of the function and the derivatives of the kernel function.

The kernel function W should meet some smoothness conditions since the gradient operator ∇ is applied on W in equation (3.10). For the SPH simulation of micro and nano-scale mechanical machining, the adopted kernel function should be sufficiently smooth for at least the kernel itself and its first two derivatives. In other words, the kernel should be at least twice continuously differentiable. This is because for the SPH simulation of micro and nano-scale mechanical machining process, the second order derivative of the kernel function is required when calculating the pressure force and the viscous force. If the second derivative of the kernel function is continuous and differentiable, the approximation of the pressure force and the viscous force during the process can be very stable and accurate even for disordered particles. If the second derivative of the kernel is not smooth enough, it can lead to numerical instability or inaccurate results. Therefore, the kernel adopted in the context of SPH simulations of micro and nano-scale mechanical machining should have continuous and differentiable derivatives up to the second order.

It should be noted that the kernel approximation is not directly linked to the micro

cutting mechanics. The kernel approximation, as the first step of the SPH method, is purely a mathematical concept or a mathematical technique that can be used to approximate an arbitrary function and its derivatives. Although the kernel approximation is not directly linked to the micro cutting mechanics, it plays a very important role in the SPH simulation of micro cutting mechanics. Based on this concept of kernel approximation expressed in equation (3.3) and equation (3.10), the relationship between the kernel approximation and the micro cutting mechanics can be explained from the following aspects.

First, the kernel approximation enables the numerical computation of micro cutting mechanics. For SPH simulations of micro cutting mechanics problems, the governing equations can be established from the conservation laws, which states that a certain number of system field variables such as the mass, momentum and energy must be conserved during the evolution process of the system. These three fundamental conservation equations, together with the constitutive material models and equation of state completely determine the behaviour of the micro cutting system. These fundamental physical equations of micro cutting mechanics can be expressed in the form of some partial differential equations (PDEs). Obtaining analytical solutions for such a set of PDEs is very difficult. The kernel approximation expressed in equation (3.10) can be used to transmit the partial differential terms in micro cutting mechanics to a differential operation on the kernel function, thereby producing a set of ordinary differential equations (ODEs) with respect only to time. These ODEs can then be easily solved via time integration. Therefore, by using kernel approximation, it becomes possible to numerically calculate micro cutting mechanics.

Second, the kernel approximation simplifies the numerical computation of micro cutting mechanics as far as the computational efforts are concerned. More specifically, the kernel approximation expressed in equation (3.3) transforms the numerical computation of micro cutting mechanics over the entire problem domain (for example,

the entire workpiece material) to the computation over a very small region (the support domain Ω of kernel function). This is realised by the compact support property of the kernel function, which states that the value of the kernel function is non-zero only within the effective area of a point, namely the support domain Ω of a point. In other words, the kernel approximation transforms an SPH approximation from global operation to a local operation. Therefore, the kernel approximation improves the computational efficiency of SPH simulations of micro cutting mechanics.

Third, the kernel approximation ensures a physically meaningful representation of the micro cutting mechanics. From the kernel approximation expressed in equation (3.3), the value of a function at a point can be determined from the values of the function at neighbouring particles weighted by the kernel function. When employing the kernel approximation to micro cutting mechanics, the physical properties of a point within the workpiece material are dependent on the neighbouring particles of that point, and the influence of all the neighbouring particles on the concerned particle is described by the kernel function. In other words, the kernel approximation defines how the neighbouring particles contribute to the physical properties of the concerned particle with the workpiece material. In addition, the kernel function is monotonically decreasing with the increase of the particle distance. This is physically consistent with the fact that in micro cutting mechanics, nearer particle should have a bigger influence on the concerned particle. In other words, with the increase of the distance of two interacting particles, the interaction force decreases.

Fourth, the kernel approximation mathematically provides the necessary accuracy and stability to the SPH simulation of micro cutting mechanics. Based on the third points, the kernel approximation expressed in equation (3.10) allows the spatial gradient to be determined from the values of a function and the derivatives of the kernel function, rather than from the derivatives of the function itself. This means that the kernel approximation has a smoothing effect – it reduces the smoothness requirement on

the interested field functions. In theory, by elaborate construction of the kernel function, the kernel approximation will not be sensitive to particle disorder and will produce stable solutions for PDEs in micro cutting mechanics. This feature of the kernel approximation is very important and necessary for micro cutting mechanics, as irregularly distributed particles are always encountered in micro cutting mechanics problems.

3.2.3 Particle approximation

The particle approximation is another key step in the SPH method. This process is carried out as follows. The integral form of equation (3.3) can be converted to a discretised form of summation over all the particles in the support domain, as shown in Fig. 3.1. This can be realised by replacing $d\boldsymbol{x}'$ (at particle *j*) in equation (3.3) with the finite volume ΔV_j (at particle *j*). Since the system in the support domain is represented by a finite number of particles that occupy individual space and carry individual mass, the following equation is given to express ΔV_j as:

$$\Delta V_j = \frac{m_j}{\rho_j} \tag{3.11}$$

where m_j and ρ_j represent the mass and density of particle *j*, respectively. Equation (3.11) is a very important equation that links the kernel approximation to the particle approximation. Its physical meaning can be explained from the following two aspects.

First, equation (3.11) describes an infinitesimal volume in the workpiece material with a discretised manner. As mentioned above, to obtain the discretised form of the kernel approximation expressed in equation (3.3), the infinitesimal volume $d\boldsymbol{x}'$ in the integration at the location of particle j can be replaced by the finite volume of the particle ΔV_j, where j=1, 2, …, *N* (*N* is the total number of particles within the support domain of the concerned particle i). For the particle j, its finite volume ΔV_j is related to its mass of m_j by the following equation: $m_j = \Delta V_j \cdot \rho_j$.

Second, this equation introduces the mass and density of the particle into the particle approximation. The discretised particles are now assigned a mass and a density during the particle approximation, meaning that they are actually the physical material particles and thus can represent the workpiece materials in micro cutting mechanics problems. This is probably one of the major reasons for the SPH method being particularly convenient for micro cutting mechanics problems, in which the density is a key field variable.

Using equation (3.11), the integral form of equation (3.3) can be written in the following form of particle approximation:

$$\begin{aligned} \langle f(\boldsymbol{x})\rangle &= \int_{\Omega} f(\boldsymbol{x}')W(\boldsymbol{x}-\boldsymbol{x}',h)d\boldsymbol{x}' \\ &\approx \sum_{j=1}^{N} f(\boldsymbol{x}_j)W(\boldsymbol{x}-\boldsymbol{x}_j,h)\Delta V_j \\ &= \sum_{j=1}^{N} \frac{m_j}{\rho_j} f(\boldsymbol{x}_j)W(\boldsymbol{x}-\boldsymbol{x}_j,h) \end{aligned} \tag{3.12}$$

where *N* is the number of particles within the support domain of particle i. Equation (3.12) illustrates the process of converting the integral form of kernel approximation to the discretised form of particle approximation. The "≈" symbol is adopted because the errors in particle approximation are inherent and inevitable. The phenomenon in which the particle approximation in discretised form in equation (3.12) does not exactly equal to the kernel approximation in continuous form is called particle inconsistency.

The errors of particle approximation mainly come from the following two aspects.

First is the irregularly distributed particles. The kernel approximation theoretically ensures that the first integral on the right hand side of equation (3.12) can exactly approximate a function as the particle spacing approaches zero, provided that the

kernel function is elaborately constructed. However, this is based on the assumption that the particles are uniformly distributed, which is an idealised circumstance. For more general problems, such as micro cutting mechanics problems where large deformations occur, the particles are usually irregularly distributed, which will result in unbalanced particle contribution. Therefore, the discrete counterpart of the kernel approximation will not equal the integral form and errors of particle approximation will arise.

Second is for particles on and near the boundary. In such cases, the support domain (or the kernel function) of the concerned particle is truncated by the boundary, thereby resulting in the unbalanced particles contributing to the discretised summation, even for regular particle distribution. Therefore, particles on and near the boundary will also introduce errors of particle approximation.

In summary, irregularly distributed particles and particles near the boundary will affect the particle approximation accuracy. Although novel particle-wise kernel functions (Liu and Liu, 2003) can be constructed to restore the particle inconsistency and reduce the possible errors inherent in the particle approximation, the cost-effectiveness for this approach needs to be considered since additional CPU time is required to solve the particle-wise kernel functions for all the particles. The balance between accuracy and efficiency should be taken into account when attempting to improve the particle approximation accuracy.

For a given particle i, the equation (3.12) can be written as

$$\langle f(\boldsymbol{x}_i)\rangle = \sum_{j=1}^{N} \frac{m_j}{\rho_j} f(\boldsymbol{x}_j) W(\boldsymbol{x}_i - \boldsymbol{x}_j, h) \tag{3.13}$$

Equation (3.13) implies that the value of a function at particle i can be approximated by summing up the average values of the function at all the particles within the support domain weighted by the kernel function. In other words, the particle

approximation in equation (3.13) converts the integral form of a function to the discretised summation over an arbitrary set of particles. This makes the SPH method simple without the need for a background mesh for numerical integration.

Following the same procedure in section 3.2.2, the particle approximation for the derivative of a function is:

$$\langle \nabla f(\boldsymbol{x}) \rangle = -\sum_{j=1}^{N} \frac{m_j}{\rho_j} f(\boldsymbol{x}_j) \nabla W(\boldsymbol{x} - \boldsymbol{x}_j, h) \tag{3.14}$$

For a given particle i, the equation (3.14) can be written as

$$\langle \nabla f(\boldsymbol{x}_i) \rangle = -\sum_{j=1}^{N} \frac{m_j}{\rho_j} f(\boldsymbol{x}_j) \nabla W(\boldsymbol{x}_i - \boldsymbol{x}_j, h) \tag{3.15}$$

Equations (3.13) and (3.15) are essential when dealing with the discretised form of the momentum conservation equation and the energy conservation equation with the SPH implementation (Hallquist, 2006). This is clarified and explained as follows. For SPH simulations of micro cutting mechanics problems, the workpiece material is represented by a set of SPH particles, which possess individual material properties and move according to the governing equations. The governing equations for micro cutting mechanics problems are based on three fundamental conservation laws of physics, which include conservation of mass, conservation of momentum and conservation of energy. These conservation equations state that the system field variables of the mass, momentum and energy must be conserved during the evolution process of the workpiece material. More specifically, the continuity equation is based on the conservation of mass. The momentum equation is based on the conservation of momentum, which is represented by Newton's second law in the continuum mechanics. The energy equation is based on the conservation of energy, which is a representation of the first law of thermodynamics. These three fundamental conservation equations, together with the constitutive material models and equation

of state, completely determine the behaviour of the micro cutting system.

It can also be seen from equations (3.13) and (3.15) that the particle approximation introduces the mass and density of particles. This makes the SPH method particularly convenient and popular for solid mechanics problems in which the density is a key field variable. These equations are also fundamentals for the SPH implementation in LS-DYNA, as described in the next section.

3.3 SPH implementation of micro and nano-scale tip-based material deformation in LS-DYNA

3.3.1 SPH formulations for micro and nano-scale tip-based material deformation

In section 3.2, the essential formulations for the kernel approximation and the particle approximation were presented. It is seen from equation (3.15) that the SPH method can be used to approximate the derivative of a function. This section derives the fundamental SPH equations for micro and nano-scale tip-based material deformation, aiming to illustrate how the SPH formulation takes a particle-based approximation of a continuum system. To achieve this, the governing equations of micro and nano-scale tip-based material deformation in Lagrangian form are first described. The SPH equations are then derived by discretising these governing equations using the essential formulations for the particle approximation in section 3.2. The derived SPH equations for micro and nano-scale tip-based material deformation are a set of ODEs with respect to time, which can finally be solved via time integration.

As mentioned in the previous section, the governing equations for micro and nano-scale tip-based material deformation are the conservation equations of continuum mechanics, which include conservation of mass, conservation of momentum and conservation of energy. These conservation equations state that the system field variables of the mass, momentum and energy must be conserved during the evolution process of the workpiece material. More specifically, the continuity equation is based

on the conservation of mass. The momentum equation is based on the conservation of momentum, which is represented by Newton's second law in the continuum mechanics. The energy equation is based on the conservation of energy, which is a representation of the first law of thermodynamics. These three fundamental conservation equations, together with the constitutive material models and equation of state, completely determine the micro and nano-scale tip-based material deformation.

The fundamental conservation laws of continuum mechanics in Lagrangian form are described by the following set of partial differential equations. Detailed procedures to obtain these conservation equations can be found in (Liu and Liu, 2003).

$$\begin{cases} \dfrac{D\rho}{Dt} = -\rho \dfrac{\partial \boldsymbol{v}^{\beta}}{\partial \boldsymbol{x}^{\beta}} \\ \dfrac{D\boldsymbol{v}^{\alpha}}{Dt} = \dfrac{1}{\rho} \dfrac{\partial \sigma^{\alpha\beta}}{\partial \boldsymbol{x}^{\beta}} \\ \dfrac{De}{Dt} = -\dfrac{p}{\rho} \dfrac{\partial \boldsymbol{v}^{\beta}}{\partial \boldsymbol{x}^{\beta}} + \dfrac{\mu}{2\rho} \varepsilon^{\alpha\beta} \varepsilon^{\alpha\beta} \\ \dfrac{D\boldsymbol{x}^{\alpha}}{Dt} = \boldsymbol{v}^{\alpha} \end{cases} \tag{3.16}$$

where ρ is the scalar density, e is the internal energy, p is the pressure, μ is the dynamic viscosity, $\boldsymbol{v}^{\alpha}$ and $\boldsymbol{v}^{\beta}$ are the components of velocity vector, $\sigma^{\alpha\beta}$ is the total stress tensor. $\boldsymbol{x}$ is the position vector. If the Greek superscripts α and β are used to denote the coordinate directions, the summation in the equations is taken over repeated indices, and the total time derivatives are taken in the moving Lagrangian frame.

The above conservation equations incorporate conservative and dissipative forces. In the second equation, which is the momentum equation, the considered force includes 1) the pressure and 2) the shear and normal stress when calculating the net force on a Lagrangian material element. In the third equation, which is the energy equation, the change of the internal energy of a Lagrangian material element consists of 1) the

work done by the isotropic pressure and 2) the energy dissipation due to the viscous shear forces.

The detailed SPH formulations for the conservation equations in equation (3.16) are described as follows. In order to approximate the density using SPH, the concepts of SPH approximations are applied to the continuity equation, which is the first equation in equation (3.16). More specifically, the particle approximation derived in equation (3.15) is applied to the velocity divergence part in the continuity equation, which yields the following equation.

$$\frac{D\rho_i}{Dt} = -\rho_i \sum_{j=1}^{N} \frac{m_j}{\rho_j} \boldsymbol{v}_j^{\beta} \cdot \frac{\partial W_{ij}}{\partial \boldsymbol{x}_i^{\beta}} \tag{3.17}$$

where $W_{ij} = W(x_i - x_j, h)$, which is the kernel function of particle i evaluated at particle j. After some trivial transformations, equation (3.17) can be rewritten as the following equation.

$$\frac{D\rho_i}{Dt} = \sum_{j=1}^{N} m_j \left(\boldsymbol{v}_i^{\beta} - \boldsymbol{v}_j^{\beta}\right) \cdot \frac{\partial W_{ij}}{\partial \boldsymbol{x}_i^{\beta}} \tag{3.18}$$

This equation clearly shows that the SPH approximation converts the partial differential equation of the continuity equation into an ordinary differential equation with respect only to time. The time rate of density change at a concerned particle is determined by the mass and relative velocities of all the neighbouring particles in the support domain. The gradient of the kernel determines the contribution of each neighbouring particle in the support domain.

Similar procedures can be used to derive the SPH formulations for the momentum equation. Again, the particle approximation in equation (3.15) is applied to the gradient of the total stress tensor in the momentum equation (3.16), which yields the following equation.

$$\frac{D\boldsymbol{v}_i^{\alpha}}{Dt} = \frac{1}{\rho_i}\sum_{j=1}^{N}\frac{m_j}{\rho_j}\sigma_j^{\alpha\beta}\frac{\partial W_{ij}}{\partial \boldsymbol{x}_i^{\beta}} \tag{3.19}$$

After some trivial transformations, equation (3.19) can be rewritten as the following equation.

$$\frac{D\boldsymbol{v}_i^{\alpha}}{Dt} = \sum_{j=1}^{N} m_j\frac{\sigma_i^{\alpha\beta}+\sigma_j^{\alpha\beta}}{\rho_i\rho_j}\frac{\partial W_{ij}}{\partial \boldsymbol{x}_i^{\beta}} \tag{3.20}$$

For the SPH formulations for the energy equation, which is the third equation in equation (3.16), the particle approximation in equation (3.15) is applied to the velocity divergence part, which is the first part on the right hand of the equation representing the pressure work. This pressure work is then approximated by the following equation.

$$-\frac{p}{\rho}\frac{\partial \boldsymbol{v}_i^{\beta}}{\partial \boldsymbol{x}_i^{\beta}} = \frac{p_i}{\rho_i^2}\sum_{j=1}^{N} m_j\left(\boldsymbol{v}_i^{\beta}-\boldsymbol{v}_j^{\beta}\right)\cdot\frac{\partial W_{ij}}{\partial \boldsymbol{x}_i^{\beta}} \tag{3.21}$$

Considering the pressure work and the energy dissipation caused by the viscous shear forces, the SPH formulation for internal energy can be obtained as follows.

$$\frac{De_i}{Dt} = \frac{p_i}{\rho_i^2}\sum_{j=1}^{N} m_j\left(\boldsymbol{v}_i^{\beta}-\boldsymbol{v}_j^{\beta}\right)\cdot\frac{\partial W_{ij}}{\partial \boldsymbol{x}_i^{\beta}} + \frac{\mu_i}{2\rho_i}\varepsilon_i^{\alpha\beta}\varepsilon_i^{\alpha\beta} \tag{3.22}$$

The SPH equations for micro and nano-scale tip-based material deformation to calculate the density, momentum and energy are summarised in equation (3.23). It can be seen from equation (3.16) and equation (3.23) that the SPH method converts the differential operations in the conservation equations in continuous forms to a discretised representations based on an arbitrarily set of particles. These particle-based approximations of the conservation equations in equation (3.23) are ordinary differential equations which can be solved by time integration. The SPH formulations summarised in equation (3.23) can be used to simulate micro and nano-scale tip-based material deformation in this Thesis.

$$\begin{cases} \dfrac{D\rho_i}{Dt} = \sum_{j=1}^{N} m_j \left(\boldsymbol{v}_i^{\beta} - \boldsymbol{v}_j^{\beta} \right) \cdot \dfrac{\partial W_{ij}}{\partial \boldsymbol{x}_i^{\beta}} \\ \dfrac{D\boldsymbol{v}_i^{\alpha}}{Dt} = \sum_{j=1}^{N} m_j \dfrac{\sigma_i^{\alpha\beta} + \sigma_j^{\alpha\beta}}{\rho_i \rho_j} \dfrac{\partial W_{ij}}{\partial \boldsymbol{x}_i^{\beta}} \\ \dfrac{De_i}{Dt} = \dfrac{p_i}{\rho_i^2} \sum_{j=1}^{N} m_j \left(\boldsymbol{v}_i^{\beta} - \boldsymbol{v}_j^{\beta} \right) \cdot \dfrac{\partial W_{ij}}{\partial \boldsymbol{x}_i^{\beta}} + \dfrac{\mu_i}{2\rho_i} \varepsilon_i^{\alpha\beta} \varepsilon_i^{\alpha\beta} \\ \dfrac{D\boldsymbol{x}_i^{\alpha}}{Dt} = \boldsymbol{v}_i^{\alpha} \end{cases} \tag{3.23}$$

3.3.2 General workflow of the SPH simulations conducted in this Thesis

With the aid of rapidly expanding computational power of modern machines, the SPH method has been a powerful tool in studying complex interacting systems such as micro and nano-scale mechanical machining. For example, the majority of SPH simulations of micro and nano-scale machining reported in Table 2.4 of the previous Chapter were performed with the commercially available software LS-DYNA. For this reason, all the SPH simulations in this Thesis were also conducted using LS-DYNA.

The SPH implementation of micro and nano-scale tip-based material deformation in LS-DYNA can be described with Fig. 3.2. The simulation workflow starts by establishing the mechanical tip-based deformation model, assigning material properties and defining simulation conditions with the SolidWorks software. Then, the established model with assigned physical and geometrical properties is meshed by SPH particles in LS-DYNA and converted into a keyword file, which contains all the information of each SPH particle, such as the initial velocity, initial position, mass and initial density. After inputting this keyword file into the LS-DYNA solver, SPH identifies the location of neighbouring particles for a given point according to the smoothing length and the sorting method. The sorting consists of finding which particles interact with which others at a given time. Once having the density, strain and strain rate in SPH, LS-DYNA can calculate the pressure, stresses and energy for a given particle with constitutive laws and the discrete form of conservation equations. Then, the interaction forces between SPH particles can be readily determined. These SPH particles deform or move

according to the particle forces and contact model. Finally, the topographical modification of the established SPH model is simulated by the collective movement of those SPH particles. It can be noted from Fig. 3.2 that the particle approximation is performed at the early stage of every calculation cycle; therefore, the implementation of the SPH method is not affected by the shape of the workpiece which changes with time. For this reason, SPH does not have the problem of mesh distorsion and thus can naturally handle problems with large deformation.

The fact that the implementation of the SPH method is not affected by the shape of the workpiece indicates another important advantage of SPH over the conventional mesh-based FEM, which is the adaptive nature of the SPH method. This is clarified and explained as follows. The mesh-based FEM is very difficult to simulate large deformation problems, because its formulation is based on mesh. The accuracy of the FEM will be severely affected if the mesh is heavily distorted. To minimise the mesh distortion, Adaptive rezoning procedures are required in FEM, which can be tedious and time-consuming and may introduce additional inaccuracy. As a very promising alternative to FEM, the SPH method uses particles instead of a mesh to discretise the workpiece material. The particle approximation is performed at the early stage of every time step; therefore, the use of the particles is based on the current local set of arbitrarily distributed particles. Because of this adaptive nature of the SPH method, the implementation of the SPH method is not affected by the arbitrariness of the particle distribution that changes with time. For this reason, SPH does not have the problem of mesh distortion and thus can naturally handle problems with large deformation.

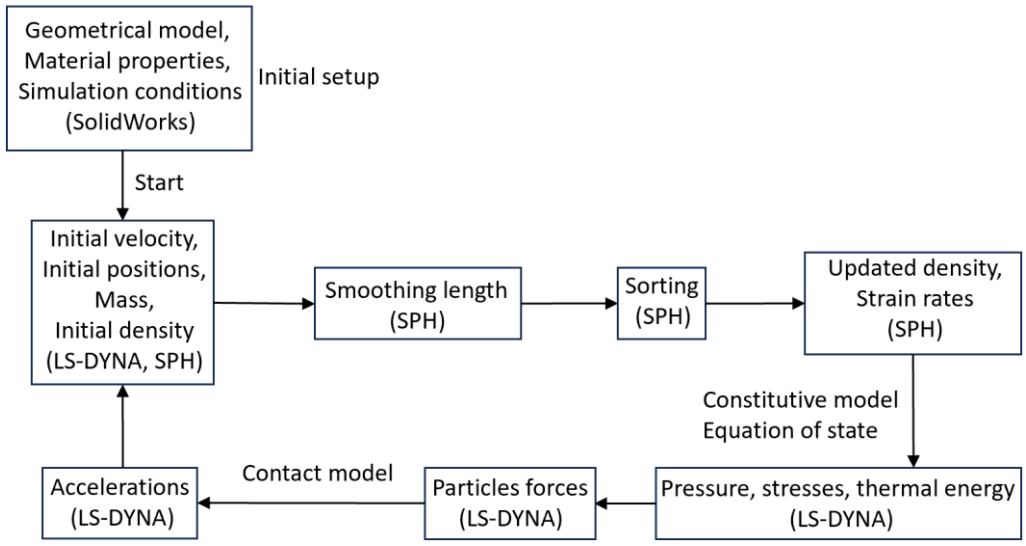

Fig. 3.2. SPH implementation of micro and nano-scale tip-based material deformation in LS-DYNA. (partly adopted from (Hallquist, 2006))

As illustrated in Fig. 3.2, the material constitutive model and contact model are integrated into LS-DYNA and play an important role in the SPH simulations of micro and nano-scale tip-based material deformation. Therefore, the material constitutive model and contact model employed in this Thesis are presented in detail in the following sub-sections.

3.3.3 Contact model

In LS-DYNA, a contact is defined by identifying which locations are to be checked for potential penetration of a slave node through a master segment, where a segment is defined to be a 3- or 4-node element of a surface in the LS-DYNA Theory Manual (Hallquist, 2006). With the SPH implementation in LS-DYNA, the surface of a body is discretised by a set of triangular (3-node element) or quadrilateral (4-node element) segments, and then each segment is replaced by an SPH particle at the centre of this segment. A search for penetrations, using any of a number of different algorithms, is made every time step. In the case of a penalty-based contact (Hallquist, 2006), when a penetration is found, a force proportional to the penetration depth is applied to resist and finally eliminate the penetration. Though sometimes it is convenient and

effective to define a single contact that handles any potential contact situation in a model, it is permissible to define any number of contacts in a single model. The implementation of the penalty-based contact algorithm is illustrated in Fig. 3.3 and described in the following paragraphs.

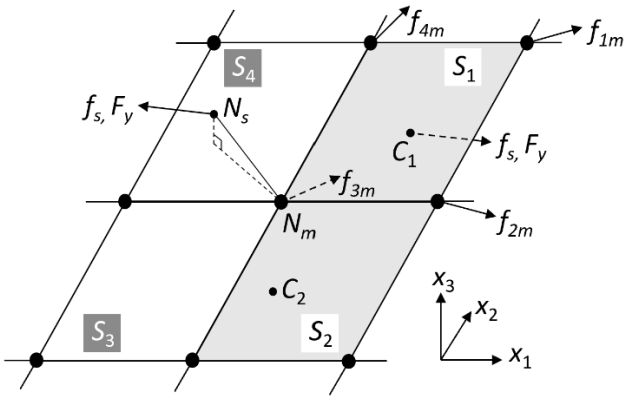

Fig. 3.3. The penalty-based contact between a slave node and a master surface in LS-DYNA.

For a given slave node N_s and a master surface, the calculation of contact starts by searching the nearest master node N_m of the slave node N_s and all the master segments related to N_m (S_1, S_2, S_3 and S_4 in Fig. 3.3). The second step is to determine potential master segments (S_1 and S_2 highlighted in grey in Fig. 3.3) through which the slave node N_s penetrates the master surface. These potential master segments can be determined by checking the orientations of master segments S_i and the position of vector N_m to N_s. The third step consists of calculating the potential locations (C_1 and C_2 in Fig. 3.3) on master segments S_1 and S_2 where penetration happens. These locations can be obtained using parameter representations of the location vector of a point on master segments. Then, the algorithm checks if the slave node N_s penetrates the master segment S_i through location C_i in this time step. If this is the case, the algorithm defines and applies a force f_s between N_s and C_i, whose value is proportional to the penetration depth. This force can be regarded as placing a spring with a specific spring stiffness between the slave node N_s and the contact location C_i. Once the contact force between N_s and C_i is determined, the friction force can also be calculated simply by

introducing the friction coefficient. The final step consists of calculating the equivalent component forces of contact force f_s (i.e. f_{1m}, f_{2m}, f_{3m} and f_{4m}) and friction force F_y on each node of the master segments S_i. The component forces of f_{1m}, f_{2m}, f_{3m}, f_{4m} can further be calculated under the global coordinate system. In the penalty-based contact algorithm, the above calculation cycle is carried out for each slave node N_s to model the actual contact between two parts in contact problems or large deformation problems. The above calculation procedure is summarised as a flowchart in Fig. 3.4.

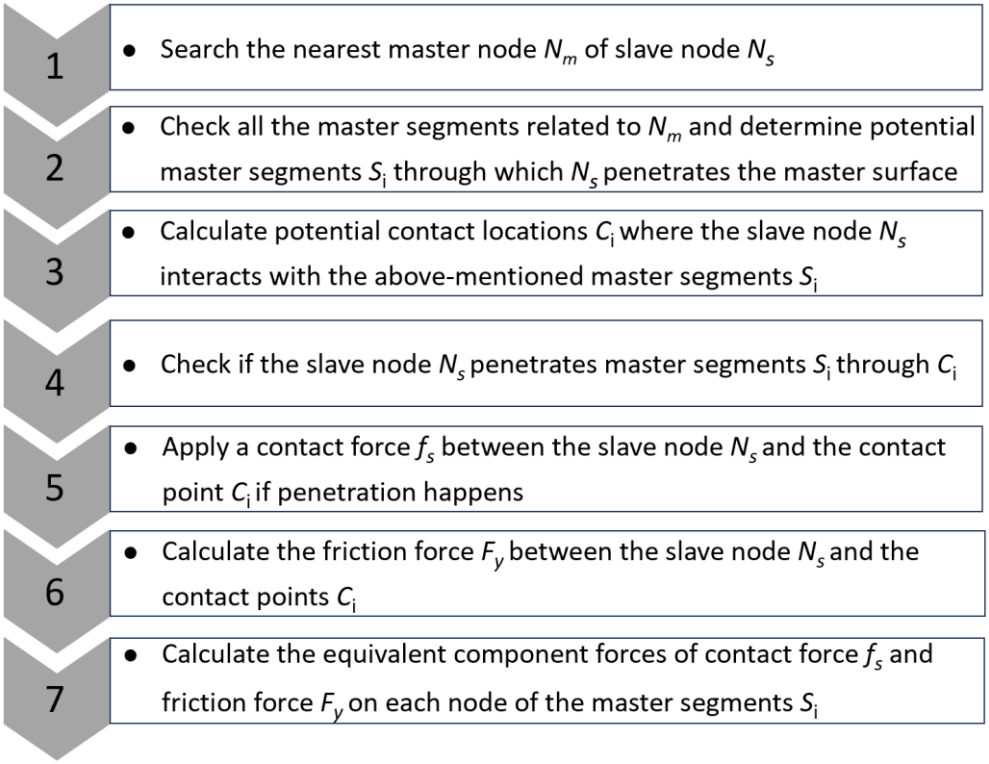

Fig. 3.4. Flow chart of the implementation of contact algorithm within one time step in LS-DYNA

To enable flexibility in modelling contact, LS-DYNA presents a number of contact types. There are mainly three such contact types, namely the single-surface contact, node-to-surface contact and surface-to-surface contact. The single surface contact is suitable for self-contact problems or large deformation problems where pre-determination of the contact surface is difficult. The surface-to-surface contact is ideal

for modelling contact where apparent sliding occurs on the contact interface. The node-to-surface contact is proposed for modelling contact where the surface of one part penetrates the surface of another. In particular, it is suitable for coupling mesh-based FEM and mesh-free SPH. LS-DYNA also defines a number of contact options, such as the General, Automatic and Eroding contact options, for each contact type to control various aspects of the contact treatment. The details of the contact model will be presented in the following paragraphs.

The contact model chosen and employed in simulations in this thesis is defined as the Contact Model a5 “*Contact_Automatic_Nodes_to_Surface” in LS-DYNA. As discussed in previous paragraphs, the penalty method has been implemented to treat interaction between disjoint parts in this contact model. Therefore, each slave node is checked for penetration through the master surface. The use of the “Nodes_to_Surface” contact type is to couple the micro and nano-scale cutting tool, defined by finite elements, and the workpiece, defined by SPH particles. This contact type is a one-way treatment of contact and indicates that only the slave nodes on the nano-indenter are checked for penetration of the master segments on the workpiece. While in a two-way treatment of contact, a second iteration to check the master nodes for penetration through the slave segments would be required. Therefore, the “Nodes_to_Surface” contact type is effective and can reduce cost in the SPH simulation of micro and nano-scale tip-based material deformation. In addition, the contact option term “Automatic” means that this contact is non-oriented and can detect penetration from either side of an element. This makes the contact type “Nodes_to_Surface” better suited for large deformation problems, such as micro and nano-scale mechanical machining. In summary, these factors mentioned above contribute toward the choice of “*Contact_ Automatic_Nodes_to_Surface” as the contact model in this thesis. It is highlighted that the contact option “Eroding” is also suitable for the SPH simulation of AFM-based DPL in Chapter 6. This is because in dynamic ploughing processes, material may be locally removed or damaged due to stress concentration, and using "Eroding" can better

describe this phenomenon where material is gradually removed or disappears during successive contact processes.

The adopted parameters of this contact model are listed in Fig. 3.5. The variable CID is a unique number that defines a contact interface ID for this contact. The eight variables in the first card define the workpiece as the master part and the cutting tool as the slave part according to their node set type and part ID. The second card defines parameters related to different types of friction, such as static friction, dynamic friction and viscous friction. The third card deals with the penalty stiffness associated with the contact force f_s. The detailed descriptions of different variables in Fig. 3.5 can be found in the LS-DYNA keyword user's manual (Hallquist, 2003).

```
*CONTACT_AUTOMATIC_NODES_TO_SURFACE_ID
$#     cid                                                          title
         1
$#    ssid      msid     sstyp     mstyp    sboxid    mboxid       spr       mpr
         2         1         3         3         0         0         0         0
$#      fs        fd        dc        vc       vdc    penchk        bt        dt
       0.0       0.0       0.0       0.0       0.0         0  0.01.00000E20
$#     sfs       sfm       sst       mst      sfst      sfmt       fsf       vsf
       1.01.0000E-12       0.0       0.0       1.0       1.0       1.0       1.0
$#    soft    sofscl    lcidab    maxpar     sbopt     depth     bsort    frcfrq
         1      0.05         0     1.025       2.0         2         0         1
```

Fig. 3.5. Keyword input of contact model in LS-DYNA employed in this Thesis.

3.3.4 Material models

LS-DYNA provides a wide range of material and equation of state models. The piecewise linear isotropic plasticity model is used in Chapter 4 to represent the KDP crystal. Two different material constitutive models are employed in Chapters 5 and 6 to describe the flow stress of the OFHC copper for comparison purpose. These material models are the Johnson-Cook and the elasto-plastic material models.

One of the constitutive models of OFHC copper chosen in this Thesis is the Johnson-Cook model (Johnson, 1983), which corresponds to Type 15 (*Mat_Johnson_Cook) in the LS-DYNA Keywords Users' Manual (Hallquist, 2003). The Johnson-Cook model can traditionally be used to provide a description of metal material behaviour with large

strains, high strain rates, and temperature-dependent visco-plasticity. In particular, it can be expressed as:

$$\sigma = (A + B\varepsilon^n)\left[1 + C\ln\left(\frac{\dot{\varepsilon}}{\dot{\varepsilon}_0}\right)\right]\left[1 - \left(\frac{T - T_0}{T_m - T_0}\right)^m\right] \tag{3.24}$$

where σ is the von Mises tensile flow stress, ε is the equivalent plastic strain, $\dot{\varepsilon}$ is its time derivative, and T is the temperature. Here, $A, B, C, m, n, \dot{\varepsilon}_0, T_0, T_m$ *are* the material yield stress, strength coefficient, strain rate parameter, temperature coefficient, strain hardening coefficient, a user-defined plastic strain rate, reference temperature and reference melting temperature respectively. The adopted parameters of the Johnson-Cook model are found in existing literature and are listed in Table 3.1. Since the values of these parameters are almost the same in different papers, those in reference (Guo et al., 2017) are employed as the values of Johnson-Cook parameters in this thesis.

The Gruneisen equation of state (EOS) is used in this research to define pressure for each discrete point in the OFHC copper. This equation states that the pressure for each discrete point could be considered as a linear function of density, internal energy and temperature. In SPH simulations of micro and nano-scale tip-based material deformation, EOS is required to accurately simulate material hydrostatic behaviour in high strain rates and material pressure. The expression of the Gruneisen EOS and its parameters for OFHC copper used can be found in (Leroch et al., 2016).

For comparison purpose, another constitutive model of OFHC copper is chosen as the elasto-plastic material model (Kreig and Key, 1976), which is a very cost-effective model and suited to model isotropic and kinematic hardening plasticity. The elasto-plastic model can be expressed with the following equation, in which the strain rate is taken into account using the Cowper and Symonds model, described in detail in (Jones, 1983).

Table 3.1. Parameters of the Johnson-Cook model of OFHC copper employed in the existing literature and this Thesis.

Reference	A (GPa)	B (GPa)	C	m	n	T_m (K)	T_0 (K)
Zhao et al., 2014	0.09	0.292	0.025	1.09	0.31		
Geng et al., 2017	0.09	0.292	0.025	1.09	0.31		
Zhao et al.,2013	0.09	0.292	0.025	1.09	0.31		
Leroch et al. 2016	0.09	0.292	0.025	1.09	0.31	1356	294
Guo et al., 2017	0.09	0.292	0.025	1.09	0.31	1356	293
Zhong et al. 2017	0.09	0.292	0.025	1.09	0.31		
This Thesis	0.09	0.292	0.025	1.09	0.31	1356	293

$$\sigma_y = \left[1 + \left(\frac{\dot{\varepsilon}}{C}\right)^{\frac{1}{p}}\right]\left(\sigma_0 + \beta \cdot \varepsilon_{eff}^{p} \cdot \frac{E \cdot E_t}{E - E_t}\right) \tag{3.25}$$

where σ_y is the yield strength, $\dot{\varepsilon}$ is the strain rate, p and C are user-defined strain rate parameters, σ_0 is the initial yield strength, ε_{eff}^{p} is the effective plastic strain, E is the Young's modulus, E_t is the tangent modulus, β is the hardening parameter. The material model 3 "*Mat_Plastic_Kinematic" in LS-DYNA corresponding to the elasto-plastic material model was employed. The parameter values of the elasto-plastic model used in this thesis are listed in Table 3.2. It should be noted that the values of yield stress (360 GPa) and tangent modulus (43 GPa) are chosen by different combinations of those values found in the literature (i.e. yield stress 340-380 GPa and a tangent modulus 38-48 GPa).

Table 3.2. Parameters of the elasto-plastic model of OFHC copper employed in this Thesis.

Parameters	Value
Density	8.93 g/cm^3
Young's modulus	117 GPa
Poisson's ratio	0.30
Tangent modulus	43 GPa
Yield stress	360 GPa

For the piecewise linear isotropic plasticity model of the KDP crystal workpiece chosen in Chapter 4, the material type 24 (*Mat_Piecewise_Linear_Plasticity) was used. For implementing this material model in LS-DYNA, a curve of effective stress versus effective plastic strain is defined by a set of discrete points. More specifically, it can approximate a realistic non-linear stress-strain behaviour by a sequence of linear segments. The formulations used for calculating and updating the deviatoric stresses and plastic strain can be respectively found in Material Model 3 and Material Model Type 24 in the LS-DYNA Theory Manual (Hallquist, 2006) for the Johnson-Cook and elasto-plastic models. The values of discrete points used for KDP crystal material model are extracted from the stress-strain curve found in the corresponding literature using a software/tool named Engauge Digitiser. The detailed process is that an image file is imported and then digitised within Engauge Digitiser by placing points along axes and curves. The resulting data points can be directly transferred to relevant input files of LS-DYNA. The curve of effective stress versus effective plastic strain of the workpiece material may be defined by these data points. The adopted parameters for this material model are listed in Fig. 3.6. The detailed descriptions of the variables in Fig. 3.6 can be found in the LS-DYNA keyword user's manual (Hallquist, 2003).

```
*DEFINE_CURVE
$#    lcid      sidr       sfa       sfo      offa      offo    dattyp
         2         0  1.000000  1.000000     0.000     0.000         0
$#              a1                  o1
             0.000               0.12
             0.042               0.76
              0.35                1.2
             0.744               1.565
*MAT_PIECEWISE_LINEAR_PLASTICITY
         2  2.338E-6      38.7     0.230      0.12       0.0  10.0E+20         0
         0         0         2         0         0
         0         0         0         0         0         0         0         0
         0         0         0         0         0         0         0         0
```

Fig. 3.6. Parameters of Piecewise Linear Isotropic Plasticity Model employed in this Thesis.

3.4 Convergence study and dimension of diamond tips

A convergence study with respect to the SPH particle density is conducted in this section. The purpose of the convergence study is to reduce the errors in particle approximation and improve the accuracy of simulation results by reducing the influence of particle density (or particle number). Detailed explanations are as follows to elaborate on the information concerning the convergence study.

As discussed earlier in section 3.2.3, in the SPH method, the errors in particle approximation (also called particle inconsistency) are inherent and inevitable. One major reason for the errors in particle approximation is the irregularly distributed particles. Under ideal conditions where SPH particles are uniformly distributed, the particle approximation in discretised form exactly equals to the kernel approximation in continuous form and errors of particle approximation will not arise. However, for micro and nano-scale mechanical machining problems where large deformations occur, the particles are usually irregularly distributed. This will result in unbalanced particle contribution in particle approximation and thus increase errors of particle approximation. One approach to mitigate the errors in particle approximation due to irregularly distributed particles is enhancing the particle density (or the particle number), which can reduce the particle spacing and thus weaken the influences of unbalanced particle contribution and irregular distribution of particles. On the other

hand, larger particle number will require more computational efforts and costs. Therefore, there should be a trade-off between the accuracy of particle approximation and computational efforts.

In this context, a convergence study with respect to the SPH particle density was conducted based on a SPH nano-indentation model in (Guo et al., 2015). This SPH model of nano-indentation is reproduced in Chapter 4 as a benchmark to study the SPH simulation of nano-indentation. To investigate whether the maximum Von Mises stress converges to a certain value as the SPH particle density increases, a set of nano-indentation simulations with different particle densities were carried out, as illustrated in Fig. 3.7. The results of the convergence study indicated that the maximum von Mises stress began to exhibit a convergent trend once the particle density exceeded 6500 per μm^3. This suggested that beyond this value of particle density, the influence of particle density on the simulation results became minimal and could be neglected. Therefore, a particle density of 7000 per μm^3 (which approximates to the number of SPH particles as 150 × 150 × 120) was chosen in the SPH model of nano-indentation reproduced from Guo et al. (2015). This value of particle density was also selected as a trade-off between the accuracy of simulation results and computational efforts.

It is important to highlight that the particle density of 7000 per μm^3 adopted from the above convergence study is not generalisable and only valid for the specific material and shape of the indenter and specimen chosen in (Guo et al., 2015). However, this value of particle density was also employed in several SPH models in Chapter 4 and Chapter 5. This is because other SPH models in Chapter 4 and Chapter 5 also showed satisfactory accuracies of simulation results when using the particle density of 7000 per μm^3 in initial simulations trials. Strictly speaking, given the complexities in material models and geometric variability, it is necessary to conduct comprehensive convergence studies for various SPH models, tailored to the specific material properties and the distinct shapes of the indenter and specimen, to ensure the

reliability of the simulation outcomes.

It should be noted that the SPH models in different benchmark studies in different chapters have different sizes of dimension. More specifically, since the workpiece dimensions in different benchmark studies in Chapter 4 and Chapter 5 are of the similar order of magnitude, the SPH particle density of 7000 per μm^3 was chosen in Chapter 4 and Chapter 5. A particle density of 7000 per nm^3 was employed in Chapter 6. In addition, since the workpieces in Chapter 5 and Chapter 6 are discretised by SPH particles with varying densities, the particle densities of 7000 per μm^3 in Chapter 5 and 7000 per nm^3 in Chapter 6 are only valid for particles in and around the vicinity of the machining area. The densities of particles in proximity of the boundary area of workpiece in these two chapters are much smaller to reduce the computational cost. The ratio between the maximum particle size in the boundary area and the minimum particle size in the machining area is 5.

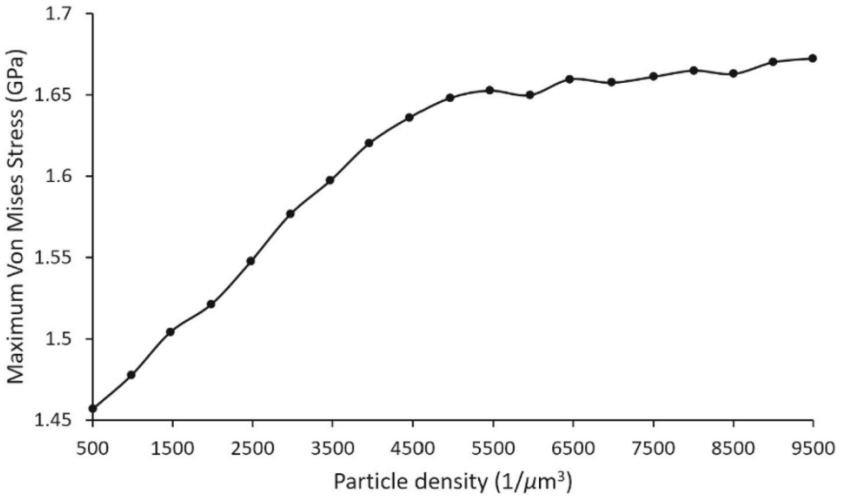

Fig. 3.7. The effect of particle density on maximum Von Mises stress during nano-indentation

As illustrated in Fig. 3.8, three types of diamond tips were employed as the micro and nano-scale indenter tips in Chapters 4-6 for different material deformation processes. They are Berkovich indenter in (Guo et al., 2015), conical indenter in (Islam et al., 2012)

and trirectangular tetrahedron indenter in (Xiao et al., 2019), respectively. The shape of the Berkovich indenter is a triangular pyramid with three edges having the same length and an angle of 115.1°, which can be calculated from (Guo et al., 2015). The conical indenter employed in Chapter 5 had a negative rake angle of 60°. The trirectangular tetrahedron indenter can be seen as a Berkovich indenter with its edges having an angle of 90°. The dimensions of these diamond tips were calculated and are summarised in Table 3.3. Here, *a*, *b*, *h* are the side length on the upper face, length of edges, and height, respectively. *r* represents the radius of the upper face of the conical indenter.

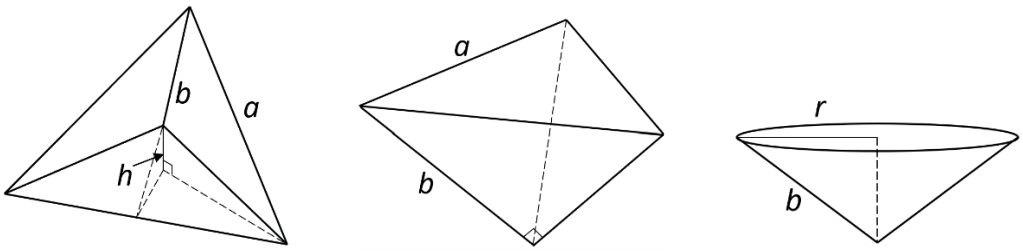

a) Berkovich indenter b) Trirectangular tetrahedron indenter c) Conical indenter

Fig. 3.8. Three types of diamond tips in this Thesis.

Table 3.3. Dimensions of different types of diamond tips.

Diamond tips	*a*(*r*)	*b*	*h*
Berkovich indenter	4 μm	2.37 μm	0.53 μm
Trirectangular tetrahedron indenter	8.06 nm	5.7 nm	3.29 nm
Conical indenter	519.62 nm	600 nm	300 nm

3.5 Concluding remarks

SPH is a mesh-free particle-based numerical method suitable for the simulation of micro and nano-scale mechanical machining. This is because the SPH method has an adaptive, meshfree and Lagrangian nature. More specifically, the SPH method employs particles to represent material, and the particle approximation in SPH is performed at every time step for the conservation equations to produce a set of ODEs in discretised Lagrangian form. This adaptive, meshfree and Lagrangian nature of the SPH method can be observed in the SPH formulation of governing equations.

This Chapter presented the detailed formulation of SPH approximations, which consists of the kernel approximation and the particle approximation. The kernel approximations of a function and its derivative are carried out in the continuum domain, and the particle approximations of a function and its derivative are carried out using discretised particles in the support domain. Two important observations from the SPH formulations are that the particle approximation converts the integral form of a function into the discretised summation over an arbitrary set of particles, and that the differential operation on a function or its derivative can be transmitted to a differential operation on the smoothing function using kernel approximation. These two essential observations about SPH formulations can be used to obtain discretised forms of governing conservation equations, which are then integrated into LS-DYNA to determine the interaction of SPH particles.

This Chapter also presented the calculation workflow of SPH simulations conducted in this thesis with LS-DYNA. The calculation cycle starts with the model establishment and initial setup in SolidWorks, followed by the generation of keyword input into LS-DYNA. The SPH formulation of governing conservation equations (integrated into LS-DYNA), material constitutive model and contact model are important elements in the calculation cycle. The material models and the contact model employed in this thesis were presented with some additional level of details, as they are vital parts of the

calculation workflow.

A convergence study was conducted as an introductory simulation to determine the optimal particle density for all subsequent simulations in the following Chapters. Dimension calculations of diamond tips employed for simulations in this thesis were also presented.

The following Chapters will provide detailed SPH simulations of micro and nano-scale tip-based material deformation, namely the nano-indentation, micro and nano-scale machining, and AFM-based dynamic ploughing lithography.

Chapter 4 SPH modelling of the nano-indentation process

4.1 Overview

The main objective of this chapter is to address the first knowledge gap of interest in this thesis, which is concerned with demonstrating the potential of the SPH method to model the material response during nano-indentation. To achieve this aim, the next section starts by reproducing an SPH model of nano-indentation reported in existing literature, which is the only research work published in the field of the SPH simulation of nano-indentation prior to the work reported in this chapter. The reproduction of this existing SPH model includes some details which were not available in the literature, such as the indentation speed, the implementation of stress-strain relationship in LS-DYNA and detailed modelling procedures. Next, in the following section, the simulation results of the reproduced SPH model are compared with those published in the literature with respect to three aspects, which are 1) the force-displacement response of the nano-indentation process, 2) distribution patterns and percentage difference of Von Mises stress and plastic strain and 3) the influence depth of the area where indentation-induced stress exists. Following this initial validation, an additional benchmark study is considered and modelled in the following section to further establish and refine the accuracy of the SPH model developed in this work. More specifically, the SPH model is extended to the simulation of micro-indentation. The results obtained are compared with FEM predictions and experimental results reported in existing literature. Based on this work, the SPH model of nano-indentation is considered to be reliable and is then employed to investigate the influence of the shape of the nano-indenter tip on material response in the context of a nano-indentation study available in existing literature. The final section presents the concluding remarks of this chapter.

4.2 SPH modelling

The computer implementation of SPH models with the ANSYS/LS-DYNA software was introduced in chapter 3. In this section, additional specific information is provided with respect to SPH simulations conducted in the context of nano-indentation only, which means that the motion between the tip and the sample is purely vertical. Focusing on nano-indentation in this chapter is of interest for the following reasons. First, nano-indentation is one of the most common techniques for the quantitative characterisation of materials, such as the extraction of hardness values, force-displacement response and other mechanical properties. Second and more importantly, nano-indentation is the first process step when conducting nano-scale machining with an AFM instrument, and thus the work conducted in this chapter for the SPH simulation of nano-indentation lays the foundations towards developing a more comprehensive model of the AFM tip-based nanomachining process in subsequent chapters.

As mentioned earlier, to the best knowledge of the author, reference (Guo et al., 2015) is the only research paper published in the field of the SPH simulation of nano-indentation. In this chapter, the SPH model for nano-indentation in (Guo et al., 2015) is reproduced for two reasons. First, this SPH model forms the basis for the validation of the initial SPH implementation work conducted in this research while enabling further investigations of the nano-indentation process. Second, some details of the SPH model for nano-indentation in (Guo et al., 2015) are not reported and it is necessary to clarify them in this thesis to make sure that the model can be easily reproduced by other researchers. For example, the convergence study in section 3.4 was conducted to determine the optimal particle density of the SPH model in (Guo et al., 2015).

The SPH model for nano-indentation was reproduced with the ANSYS/LS-DYNA software, as shown in Fig. 4.1. A Berkovich indenter made of diamond was modelled

to move vertically into the Potassium dihydrogen phosphate (KDP) workpiece to form a nano-indent. The dimension of the Berkovich indenter was already listed in Table 3.3 in the previous chapter. The diamond material was modelled with a density of 3.515 g/cm^3, a Young's modulus of 1140 GPa and a Poisson's ratio equal to 0.29. The dimension of the KDP workpiece was 8 × 8 × 6 μm^3. The stress-strain behaviour of the KDP workpiece can be found in Figure 5 in (Guo et al., 2015) and, as presented in section 3.3.3, the values of discrete points extracted from the stress-strain curve were listed in Fig. 3.6 in the previous chapter. It should be noted that the units of the density and Young's modulus in Fig. 3.6 were respectively 10^6 g/cm^3 and GPa. These were derived from the adopted μm-μg-μs unit system for length, mass and time in the model. The diamond nano-indenter was discretised with a FEM mesh and the KDP workpiece was represented by SPH particles. The three layers of SPH particles at the bottom of the workpiece were fixed for the whole six degrees of freedom. The Berkovich nano-indenter was first vertically indented into the sample to reach a given indentation depth of 500 nm, and then withdrawn from the sample along the same tool path. Considering the indentation speed was not reported in (Guo et al., 2015), a constant indentation speed of 100 m/s was employed in the reproduced SPH model. This high indentation speed is necessary for reducing the very large computational time required for the simulations. At the same time, as observed in references (Zhao et al., 2014; Li et al., 2021; Leroch et al., 2016; Guo et al., 2017), the accuracy and trend of the simulation results should not be compromised when using higher cutting speed in simulations instead of using actual experimental cutting speed values. Therefore, it is anticipated that this high indentation speed should accelerate simulations while maintaining the level of accuracy. The simulations were performed on Hawk Supercomputer in Wales and it took around two hours to compute using 128 cores.

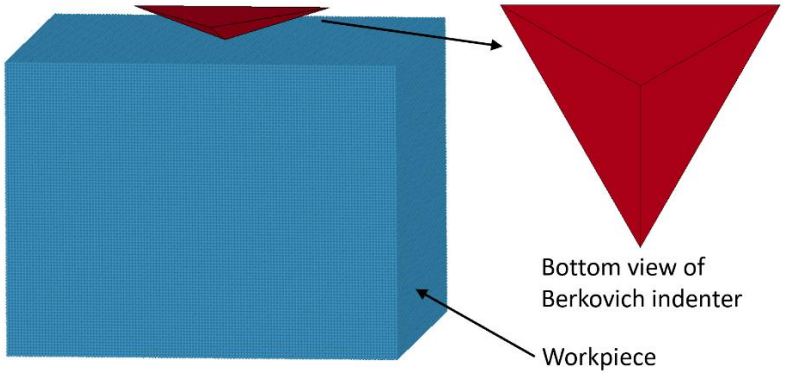

Fig. 4.1. Reproduced SPH model of nano-indentation.

4.3 Validation examination of the reproduced SPH model

After the reproduction of the SPH model of nano-indentation, the simulation results were compared with those reported in (Guo et al., 2015) to validate the accuracy of the model. The load-displacement response of an elasto-plastic material to sharp indentation is an important factor when characterising the nano-indentation process. Figure 4.2 shows the force-displacement response of the simulated nano-indentation process . It can be seen that there exists no contact force between the indenter and workpiece until the vertical displacement of the indenter reaches about 25 nm into the workpiece. This may be attributed to the following two reasons. First, the SPH particles generated in ANSYS/LS-DYNA software are located at the centre of the volume space each particle occupied, and thus there exists an initial gap between the indenter tip and workpiece whose value equals to the radius of each particle volume (6 μm ÷ 120 ÷ 2 = 25 nm). Second, the SPH particles may not be located directly below the indenter tip, and thus the indenter needs to travel an additional distance before its edge or side face comes into contact with a SPH particle. To compare the simulated force-displacement response with those reported in (Guo et al., 2015), the origin of the force-displacement curve in Fig. 4.2 should be at co-ordinates (0.025, 0). This point corresponds to the initial contact that occurs when the displacement of the indenter reaches 25 nm. The comparison of simulated force-displacement response with those

reported in (Guo et al., 2015) is shown in Fig. 4.3. It can be seen that compared with the SPH simulation result in (Guo et al., 2015), the force-displacement response obtained with the reproduced SPH model is closer to the reported experimental result during the entire nano-indentation process. Therefore, the reproduction of the SPH model of nano-indentation is considered to be successful for the prediction of the force-displacement response.

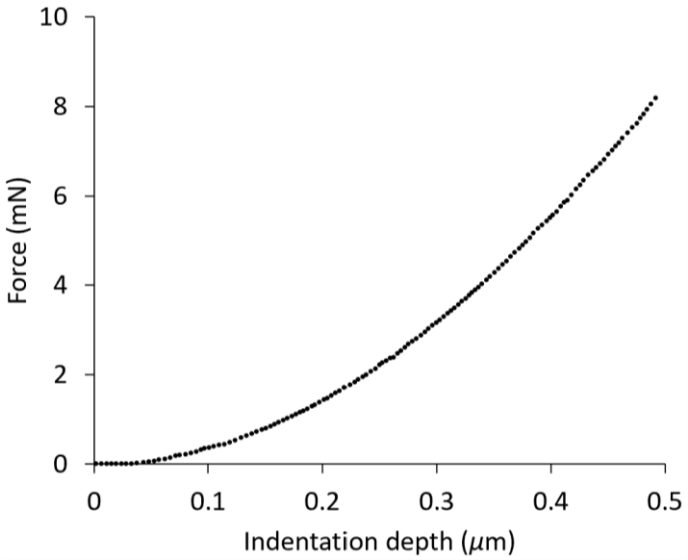

Fig. 4.2. Force-displacement curve in the reproduced model (without shift).

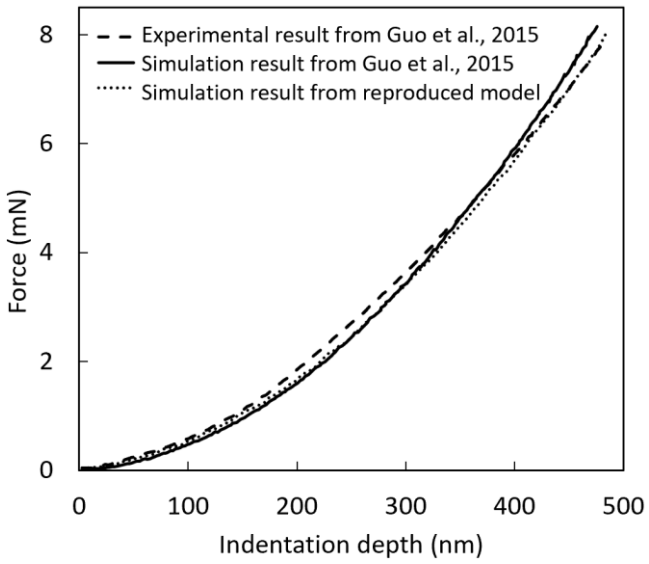

Fig. 4.3. Comparison of force-displacement curves from Guo et al. (2015) and reproduced model.

The second aspect of validation of the reproduced SPH model is the Von Mises stress and plastic strain occurring during nano-indentation. The distribution of Von Mises stress at different indentation depths is shown in Fig 4.4. The specific indentation depths used were specifically chosen for comparison purposes. It can be seen that the distribution patterns of Von Mises stress at these indentation depths are in good agreement with those reported in Guo et al. (2015). In addition, the maximum Von Mises stress always occurs around the indentation area during the indentation process, which results in stress concentration. This phenomenon is further clarified in Fig. 4.5, which is a zoomed-in image of the indentation area at an indentation depth of 418 nm. Figure 4.6 illustrates the distribution of plastic strain at the end of loading process, which corresponds to an indentation depth of 470 nm in Fig. 11 in (Guo et al., 2015). It can be seen that the distribution pattern of plastic strain at the end of loading process is also in good agreement with that reported in (Guo et al., 2015).

In addition to the distribution patterns of Von Mises stress and plastic strain, the maximum values of Von Mises stress and plastic strain were also compared for the validation of the reproduced SPH model. The comparison of maximum Von Mises stresses at different indentation depths is shown in Fig. 4.7. The corresponding percentage differences are listed in Table 4.1. These results indicate that the ability of the reproduced SPH model to predict the Von Mises stress is more satisfactory with a relatively large indentation depth. The percentage difference of the maximum Von Mises stress is relatively large (16.85%) when the indentation depth is small (h=88 nm).

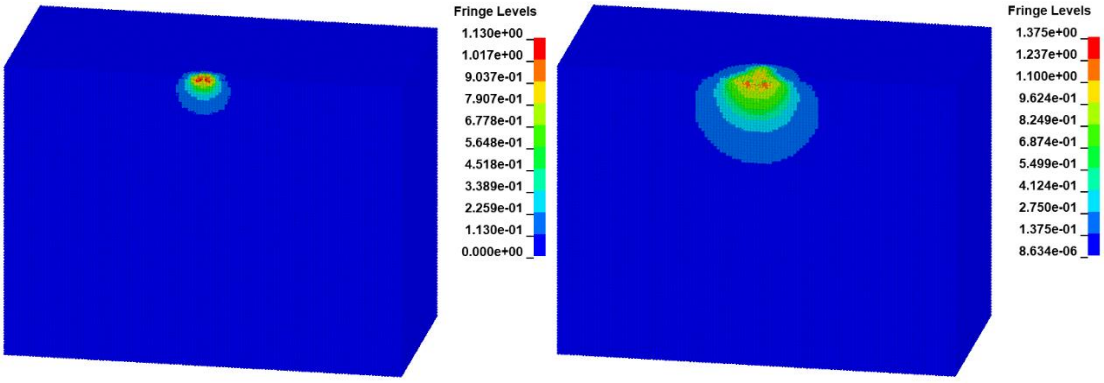

(a) h=88 nm (b) h=198 nm

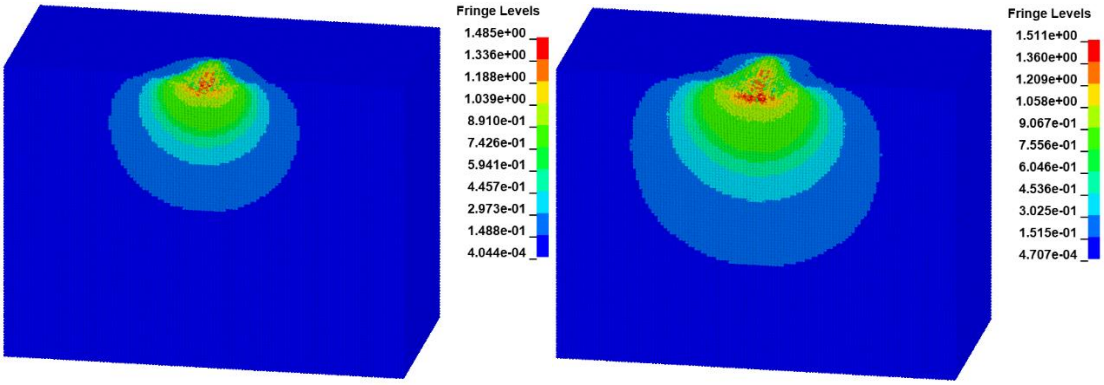

(c) h=308 nm (d) h=418 nm

Fig. 4.4. The distribution of Von Mises stress at different indentation depths.

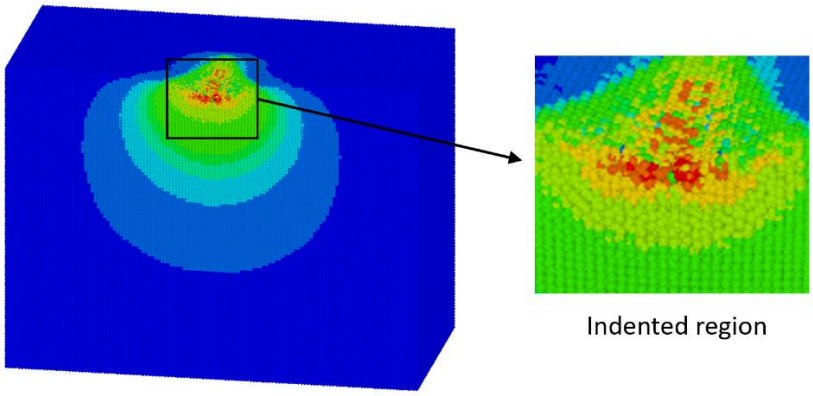

Fig. 4.5. The zoomed-in image of the indented region when h = 418 nm.

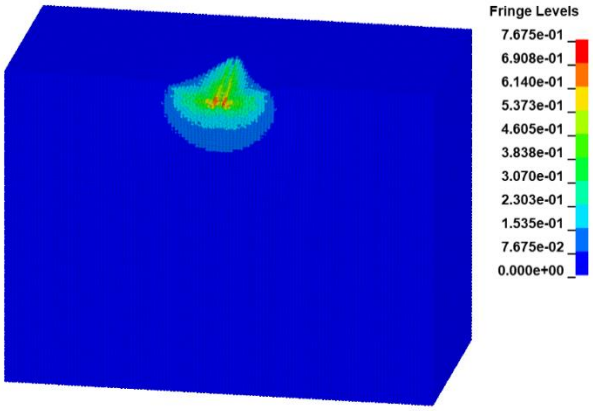

Fig. 4.6. The distribution of plastic strain at the end of loading process.

This large difference may be related to the existence of the initial gap between the indenter tip and workpiece in the reproduced SPH model. In the reproduced SPH model, when using SPH particles to discretise the workpiece material in ANSYS/LS-DYNA software, the generated SPH particles are located at the centre of the finite volume space each particle occupies, and thus a particle spacing exists and equals to the diameter of each particle. Therefore, there exists an initial gap between the indenter tip and workpiece whose value equals to the radius of each SPH particle. According to the convergence results presented in Chapter 3, this initial gap equals to 6 μm ÷ 120 ÷ 2 = 25 nm. This means that for a given specified indentation depth, the actual depth achieved in the reproduced SPH nano-indentation model is always smaller than the intended value. In addition, the difference between the actual depth achieved in the reproduced SPH nano-indentation model and the intended value is always 25 nm. If the intended indentation depth h is large, the discrepancy between the actual depth and the intended value has a relatively negligible impact. However, the influence of this difference becomes significant as h decreases. For example, for $h = 88\text{nm}$ in Fig. 4.7, the percentage difference between the actual depth and the intended depth is $25/88 \times 100\% = 28.4\%$, while this value is only 6.0% for $h = 418\text{nm}$. Therefore, the initial gap between the indenter tip and workpiece, which is inherent in the SPH nano-indentation model established in ANSYS/LS-DYNA software,

should be accounted for the high difference in maximum Von Mises stress for $h = 88\text{nm}$ in Fig. 4.7.

It should be highlighted that some detailed information on the SPH model in (Guo et al., 2015), such as the convergence study, particle density, particle number, were not reported in the literature. Therefore, the particle spacing and the initial gap between the indenter tip and workpiece in the SPH model in (Guo et al., 2015) cannot be exactly compared with those in the reproduced SPH model to quantitatively explain the high difference in maximum Von Mises stress for $h = 88\text{nm}$ in Fig. 4.7.

In addition, the percentage difference of the maximum plastic strain at the end of loading process is (0.814-0.7675)/0.814=5.71%, which is within reasonable acceptance range. Overall, it can be said that the distribution patterns and the percentage difference of Von Mises stress and plastic strain further validate the predictability and reliability of the reproduced SPH model.

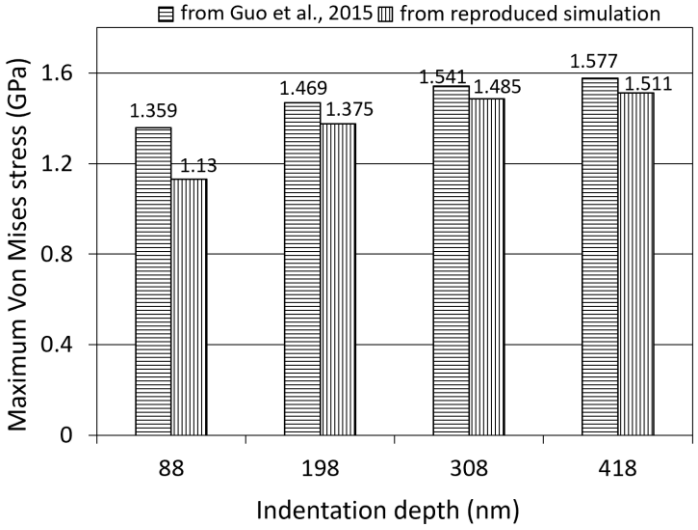

Fig. 4.7. Comparison of maximum Von Mises stress from (Guo et al., 2015) and reproduced simulation.

Table 4.1. Percentage differences of the maximum Von Mises stresses at different indentation depths.

Indentation depth (nm)	Percentage difference of the maximum Von Mises stress
88	16.85%
198	6.40%
308	3.63%
418	4.19%

It can be seen from Fig. 4.7 that the maximum Von Mises stress data from reproduced simulations are all smaller than those from the published literature. This may be attributed to the following reasons.

First, as discussed earlier, the actual depth achieved in the reproduced SPH nano-indentation model is always smaller than the intended value due to the existence of the initial gap between the indenter tip and workpiece. This may result in a smaller reproduced maximum Von Mises stress.

Second, in the reproduced SPH model of nano-indentation, an SPH particle may not be located directly below the indenter tip due to the existence of the particle spacing, and thus the indenter may need to travel an additional distance before its edge or side face comes into contact with an SPH particle. Therefore, for a given specified indentation depth in Fig. 4.7, the actual depth achieved in the reproduced SPH nano-indentation model is further decreased and this may also contribute to a smaller simulated maximum Von Mises stress.

The third approach used to validate the reproduced SPH model was to study the influence depth. This is the depth of the region where indentation-induced stress exists. To achieve this, a variable k, which is the ratio between the indentation depth (m) and corresponding influence depth (n), was used. For a specific indentation depth,

the variation on the variable *k* can reflect variations on the corresponding influence depth and the area where indentation-induced stress is present. Fig. 4.8 shows the variation of the variable *k* during the nano-indentation process. The variable *k* obtained from the reproduced simulations remains approximately constant, which means that the area where indentation-induced stress influences is nearly proportional to the indentation depth. The same observation can also be found from the values of the variable *k* reported in (Guo et al., 2015).

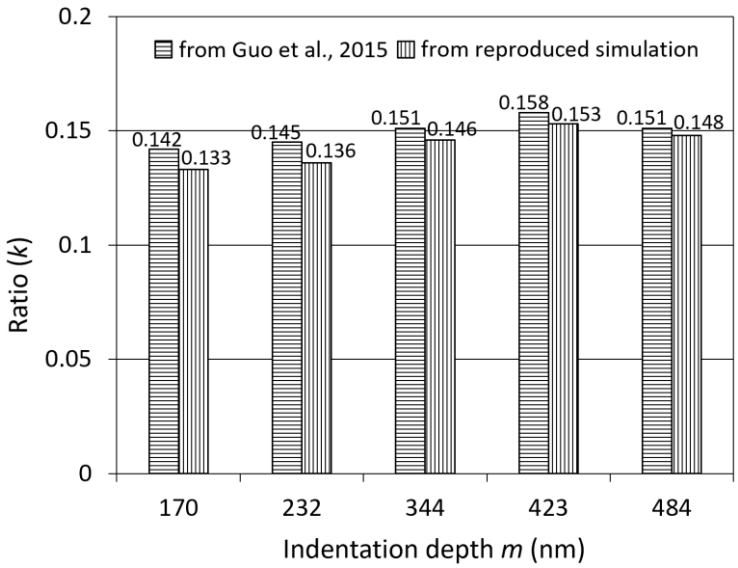

Fig. 4.8. Comparison of ratio between the indentation depth and influence depth of maximum Von Mises stress.

To compare the influence depth obtained from the reproduced simulation with that in Guo et al (106), the average value for the variable *k* was calculated and is listed in Table 4.2. It can be seen that the averaged value of variable *k* is 0.143 in the reproduced simulation, a reasonable percentage difference of 4.03% compared to the value of 0.149 in (Guo et al., 2015). Therefore, the reproduced SPH model has also been validated for the prediction of influence depth and the area where indentation-induced stress exists.

Table 4.2. Different ways to compare the variable *k*.

	From Guo et al. (106)	From reproduced simulation	Percentage difference
Average value	0.149	0.143	4.03%

From Fig. 4.8 and Table 4.2, it can be seen that the ratio *k* obtained from reproduced simulations are all smaller than those found in the published literature. This indicates that for a given indentation depth, the influence depth of maximum Von Mises stress obtained from reproduced simulations is larger than that found in the published literature. It should be noted that this finding is not entirely consistent with the results presented in Fig. 4.7 that the maximum Von Mises stresses obtained from reproduced simulations are smaller than those in the published literature. Possible reasons behind this observation are likely due to the definition and determination of the influence depth of the maximum Von Mises stress. Detailed explanations are as follows.

First, in the reproduced SPH model of nano-indentation, the influence depth of the maximum Von Mises stress is defined as the depth where indentation-induced stress corresponds to 0.3 GPa. The value of 0.3 GPa has been estimated and selected as it provides the most consistent alignment with the results presented in Figures 7 and 8 and Table 3 of the study by Guo et al. (2015). However, it is important to highlight that the concept of influence depth is not clearly and explicitly defined in (Guo et al. (2015)). Therefore, it is reasonable to observe some discrepancies between the influence depths obtained from reproduced simulations and those in the selected literature.

The second reason may be related to different particle resolutions in the two different SPH nano-indentation models. In the reproduced SPH model of nano-indentation, the number of particles is chosen as 150 × 150 × 120 and a particle density of 7000 per μm^3 is employed based on the convergence study. However, the number of particles

and the particle density are not provided in (Guo et al. (2015)). Therefore, these two different SPH nano-indentation models may have different particle resolutions. This can affect the determination of the influence depth of the maximum Von Mises stress since the influence depth is directly visually determined from stress distribution figures.

However, despite the observation that the influence depth obtained from reproduced simulations is larger than that found in the published literature, the reproduced SPH model of nano-indentation is still considered to display satisfactory accuracy for the prediction of the influence depth during nano-indentation. This is because the trend of variation of the variable *k* during the nano-indentation process is more important and useful for comparison and validation purposes, compared with the discrepancies of the values of variable *k* for a given indentation depth.

From the above validation study, the reproduced SPH model of nano-indentation is considered to display satisfactory accuracy for the prediction of the force-displacement response, stress and strain distribution, the maximum Von Mises stress and the influence depth during nano-indentation.

4.4 Comparison of the SPH model with FEM and experimental results

Following the validation study conducted in the section 4.3, this section further establishes and improves the accuracy of the validated SPH model. To achieve this, another benchmark study was considered but this time in the context of micro-indentation (Dao et al., 2001). The SPH model-based simulation results could then be compared with both the FEM-predicted and experimental results of (Dao et al., 2001).

The SPH model of micro-indentation developed was similar to the process followed in section 4.2. In (Dao et al., 2001), a three-dimensional finite element model incorporating a Berkovich indenter was constructed to simulate the micro-indentation

response of ductile materials, and the simulated FEM results were verified by instrumented indentation experiments. In this context, the implemented SPH model in Fig. 4.1 could be directly used, after simply adjusting its dimensions, to compare with the FEM implementation in (Dao et al., 2001). The diamond indenter had a Young's modulus of 1100 GPa and a Poisson's ratio of 0.07 (Dao et al., 2001). The experimental stress-strain data of both 7075-T651 aluminum and 6061-T6511 aluminum workpieces reported in (Dao et al., 2001) were extracted using the Engauge Digitizer and then employed as direct input for the SPH simulations. The adopted parameters for 7075-T651 aluminum are listed in Fig 4.9. As mentioned before, it should be noted that the units of the density and Young's modulus here are respectively 10^6 g/cm^3 and GPa, which are derived from the adopted μm-μg-μs unit system for length, mass and time in the model. The loading/unloading indentation speeds were chosen as 100 m/s to be consistent with the values established in section 4.2. The simulations were performed on the Hawk Supercomputer in Wales.

```
*DEFINE_CURVE
         2         0       1.0       1.0       0.0       0.0         0         0
          0.000805              0.00687
           0.00725              0.45868
          0.009483              0.49684
          0.014004              0.54608
          0.025409              0.59314
           0.04502              0.62966
          0.091134              0.68906
          0.164688               0.7325
          0.239557              0.77595
          0.346022              0.79587
*MAT_PIECEWISE_LINEAR_PLASTICITY
         22.85000E-6     70.15      0.28      0.12      0.01.00000E21       0.0
       0.0       0.0         2         0       0.0
       0.0       0.0       0.0       0.0       0.0       0.0       0.0       0.0
       0.0       0.0       0.0       0.0       0.0       0.0       0.0       0.0
```

Fig. 4.9. Adopted parameters for 7075-T651 aluminum.

Figure 4.10 shows the simulated micro-indentation response of 7075-T651 aluminum (in grey colour) using the above-mentioned SPH model, which is also compared with the FEM-predicted and experimental results reported in (Dao et al., 2001). It can be seen that the SPH model-based loading curve matches well with the FEM predictions

(in orange colour) and experimental results (in blue colour). However, there is an obvious discrepancy in unloading curves. In particular, for the SPH results with loading/unloading speed of 100 m/s, the slope of the unloading curve and the residual depth are both larger than those obtained with FEM simulations and experiments. To explore possible reasons related to this observation, several additional loading and unloading speeds (i.e. 10 m/s, 1 m/s and 0.1 m/s) were applied to the indenter, and corresponding SPH predictions of force-displacement curves were superimposed to the 100 m/s curves in Fig. 4.10. It can be seen that for the unloading response of the process, the slope of the unloading curve and the residual depth decrease as the loading/unloading speed decreases. These new observations may demonstrate potential relationship between the elastic recovery of ductile materials and unloading speeds.

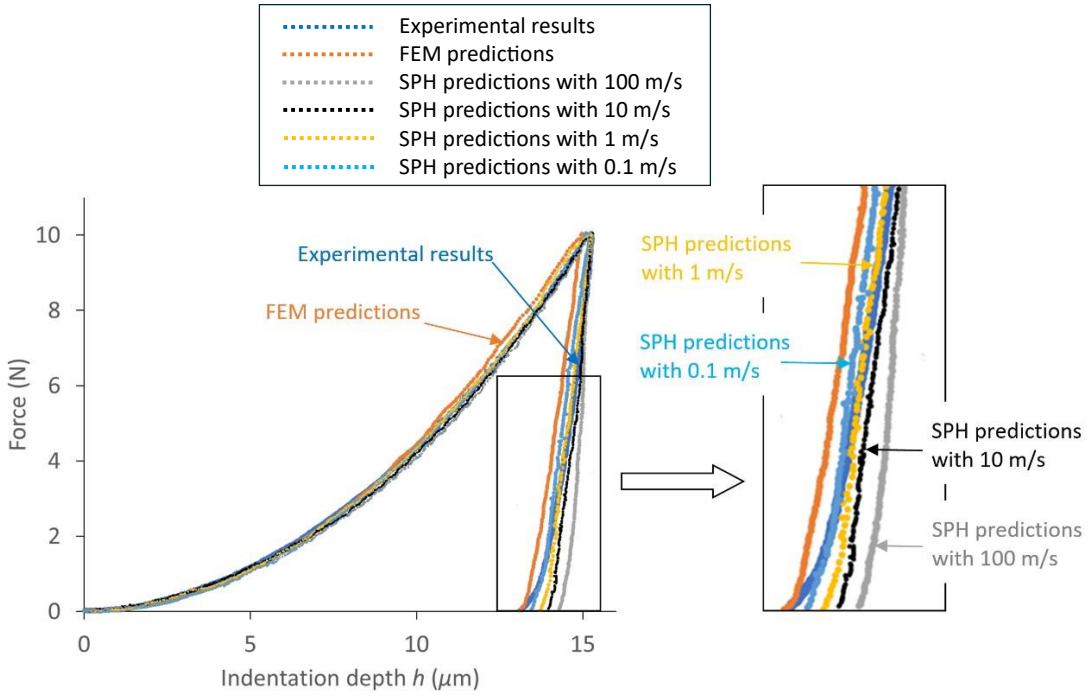

Fig. 4.10. Force-displacement curves of 7075-T651 aluminum from SPH simulations in this chapter and from FEM-predicted and experimental results in (Dao et al., 2001).

Figure. 4.11 presents the simulated micro-indentation response of the 6061-T6511 aluminum workpiece. For the loading process, only SPH predictions with a loading

speed of 100 m/s are presented for clarity purpose. Similar observations can be made as those seen in Fig. 4.11. In particular, 1) the SPH model-based loading curve matches well with the FEM predictions and experimental results, and 2) the SPH predictions of the unloading curve become closer to the experimental results as the unloading speed decreases. These different sensitivities between loading and unloading curves could be related to the material model employed in this chapter. More specifically, the stress-strain curves in Fig. 4 in (Dao et al., 2001) were obtained from uniaxial compression tests. This material model from compression tests may have different influence on material response during tensile and compressive processes.

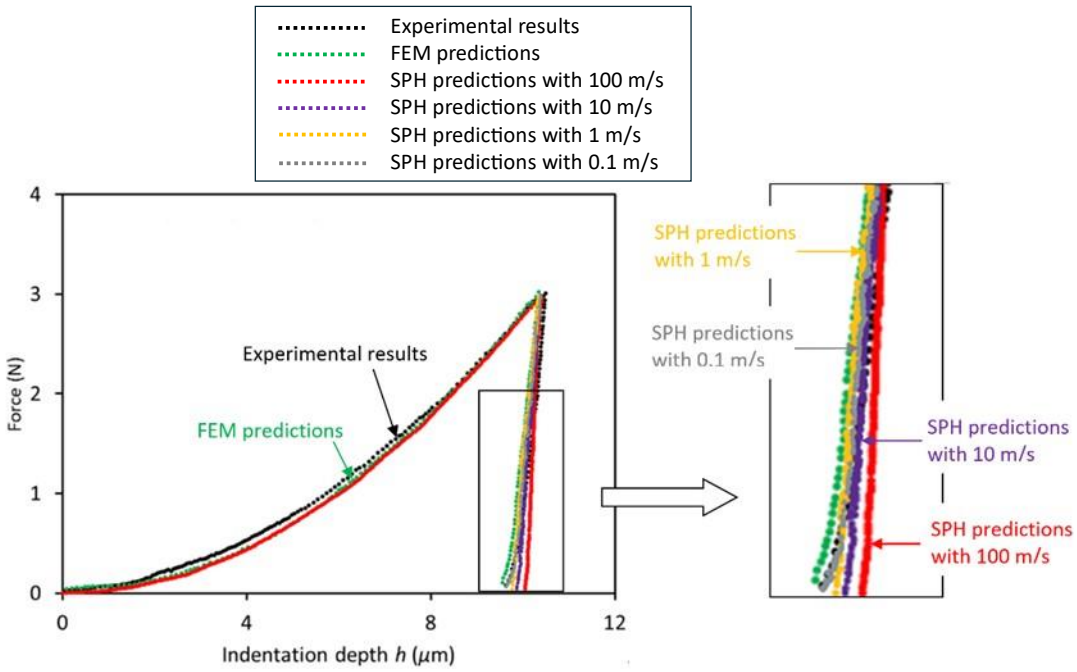

Fig. 4.11. Force-displacement curves of 6061-T6511 aluminum from SPH simulations in this chapter and from FEM-predicted and experimental results in (Dao et al., 2001).

Another explanation of the influence of loading/unloading speed on the material response could be related to possible fracture or failure inside the workpiece with a high loading speed. Fracture inside the workpiece may have an influence on material behavior. To confirm or exclude this possible explanation, energy maps (i.e. internal energy map, kinetic energy map and total energy map) during SPH simulation of

micro-indentation on the 6061-T6511 aluminum specimen with a loading and unloading speed of 100 m/s were obtained. These are plotted in Figs. 4.12 to 4.14. LS-DYNA allows tracking of the total energy of the system during a simulation. The total material energy against simulation time could help shed light onto varying behavior of the simulation at multiple indentation depths and unloading speeds: sudden variations of energy may indicate the onset of cracking inside the workpiece. It can be seen from Fig. 4.14 that the total energy increases during the loading process and keeps almost constant during unloading. There is no abrupt variation in the total energy map. Therefore, there should be no crack generated with a maximum indentation depth of 10 μm during micro-indentation on the 6061-T6511 aluminum specimen with a loading speed of 100 m/s. The same trend of total energy was observed with loading and unloading speeds of 10 m/s and 1 m/s. The difference was that values of internal energy, kinetic energy and total energy decreased as the speed decreased. Since the total energy map did not indicate any crack generation inside the workpiece, the influence of crack or fracture inside the workpiece should not be accounted for the varying behavior of the unloading response at multiple unloading speeds.

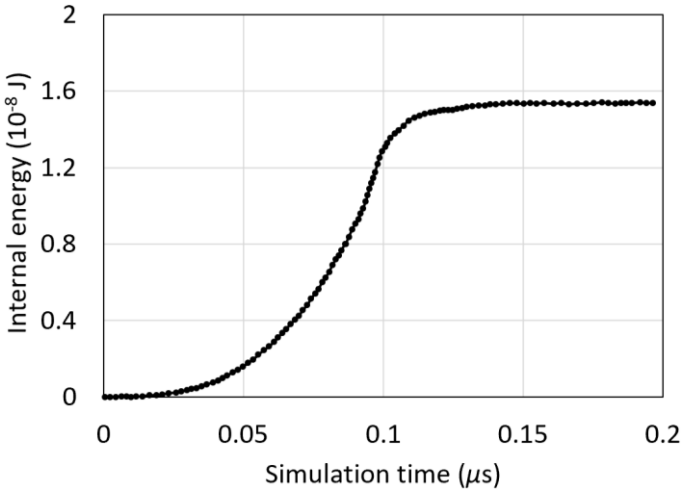

Fig. 4.12. Internal energy during SPH simulation of micro-indentation on the 6061-T6511 aluminum specimen with a speed of 100 m/s

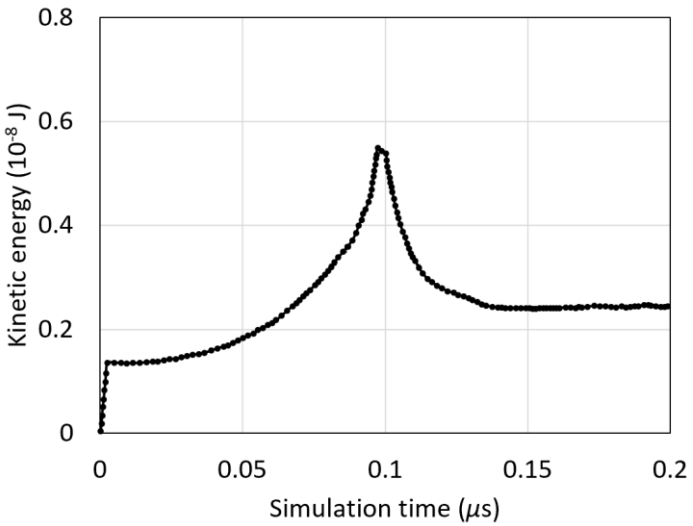

Fig. 4.13. Kinetic energy during SPH simulation of micro-indentation on the 6061-T6511 aluminum specimen with a speed of 100 m/s

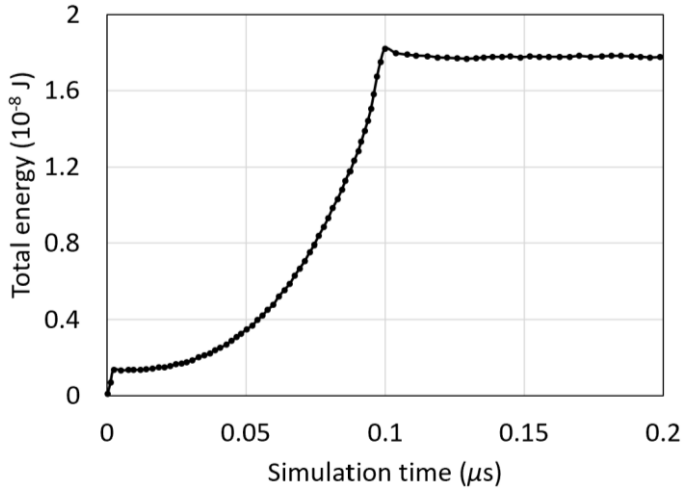

Fig. 4.14. Total energy during SPH simulation of micro-indentation on the 6061-T6511 aluminum specimen with a speed of 100 m/s

4.5 Investigation of effect of indenter tip on nano-indentation response

After the validation examination in section 4.3 and the further benchmark study of the SPH model in section 4.4, the implemented model was considered to be able to simulate the micro and nano-scale indentation process with a satisfactory level of accuracy. In this section, this model was employed to investigate the influence of the

shape of the nano-indenter tip on the material response in the context of the nano-indentation study reported in (Karimzadeh et al., 2014).

For this purpose, minor adjustments were made to the implemented SPH model in section 4.2 to reproduce the nano-indentation model reported in (Karimzadeh et al., 2014). In particular, in (Karimzadeh et al., 2014), nano-indentation tests were conducted on aluminum 1100, and a finite element model was employed to simulate this nano-indentation process. Both a sharp Berkovich indenter and a round-tip Berkovich indenter with a tip radius of 200 nm were used in (Karimzadeh et al., 2014). The primary adjustments to the implemented SPH model focussed on the shape of indenter tip and material parameters. The dimension and material parameters of the sharp Berkovich indenter can be found in Table 3.3 and section 4.2. The round-tip Berkovich indenter was established in SolidWorks via the following steps: (1) use "Lofted Boss/Base" option to develop a Berkovich indenter with a sharp tip, (2) establish a revolved spherical surface (with a radius of 200 nm) to model the spherical surface of the rounded tip, (3) split the sharp-tip Berkovich indenter by the revolved spherical surface, (4) delete the revolved spherical surface and the split sharp tip of the Berkovich indenter. Then the established round-tip Berkovich indenter (shown in Fig. 4.16) was imported from SolidWorks into ANSYS/LS-DYNA. Other parameters of the round-tip indenter were chosen as those of a standard sharp Berkovich indenter. The experimental stress-strain data of aluminum 1100 in (Karimzadeh et al., 2014) were extracted using the Engauge Digitizer and then employed as direct input for SPH simulations. The adopted parameters of aluminum 1100 are listed in Fig 4.15. The loading/unloading speeds for SPH simulations were chosen as 10 m/s. Different from the case of micro-indentation in section 4.4, the stress-strain data of aluminum 1100 in (Karimzadeh et al., 2014) was obtained from uniaxial tensile experiments. The influence of the indenter tip on SPH model-based nano-indentation responses and its comparison with FEM and experimental results in (Karimzadeh et al., 2014) are illustrated in Fig. 4.17.

```
*DEFINE_CURVE
         2         0       1.0       1.0       0.0       0.0         0         0
          0.000102            0.000381
          0.000582            0.049916
          0.001102            0.100077
          0.001703            0.131474
          0.002279             0.14969
          0.003643            0.168985
          0.005849            0.183777
          0.009921            0.189792
          0.019906            0.196689
          0.035787            0.201099
          0.055768            0.201552
          0.067823            0.198747
          0.075692             0.19453
          0.087151            0.182652
          0.093511            0.170737
          0.096063            0.149084
          0.096694            0.141171
*MAT_PIECEWISE_LINEAR_PLASTICITY
         22.70000E-6     75.31      0.33      0.15       0.01.00000E21       0.0
        0.0       0.0         2         0       0.0
        0.0       0.0       0.0       0.0       0.0       0.0       0.0       0.0
        0.0       0.0       0.0       0.0       0.0       0.0       0.0       0.0
```

Fig. 4.15. Adopted parameters for aluminum 1100.

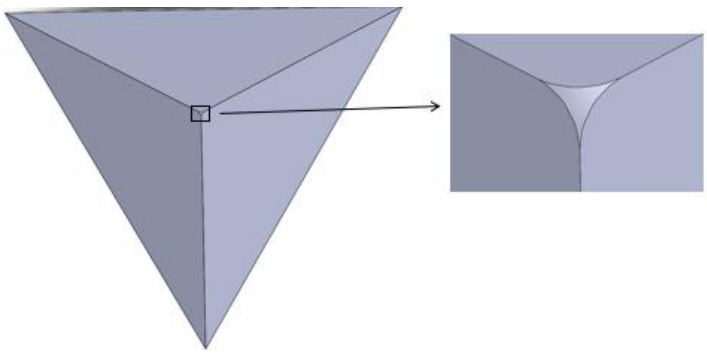

Fig. 4.16. The round-tip Berkovich indenter with a tip radius of 200 nm.

It can be seen from Fig. 4.17 that the SPH outcomes compared well with the FEM predictions results reported in (Karimzadeh et al., 2014), for sharp-tip indenter. In addition, the SPH results aligned very well with the experimental results with a round-tip indenter, which was not the case for the FEM predictions in (Karimzadeh et al., 2014). In addition, the resultant force with a round-tip indenter was noted to be always larger than that with a sharp-tip indenter. The primary reason could be the increase in contact area between the indenter and specimen surface when using a round-tip indenter. Another explanation could be the increase in friction force with blunt

indenters. It should be noted that the discrepancy in unloading curves in Fig. 4.17 is smaller than that in Fig. 4.10 and Fig. 4.11. Considering that the stress-strain data of the workpiece used here were recorded using uniaxial tensile experiments and not using experimental uniaxial compression as was the case in section 4.3.2, this can be seen as another support for the hypothesis in section 4.3.2 that the discrepancy of the unloading material responses could be related to the employed material model.

It can also be seen from Fig. 4.17 that the round-tip Berkovich indenter with a tip radius of 200 nm is better for nano-scale machining on aluminum 1100 compared to the standard sharp Berkovich indenter. This is because the SPH-predicted resultant force obtained using a round-tip Berkovich indenter is much closer to the experimental results in the literature, compared with the SPH-predicted resultant force obtained using a sharp Berkovich indenter.

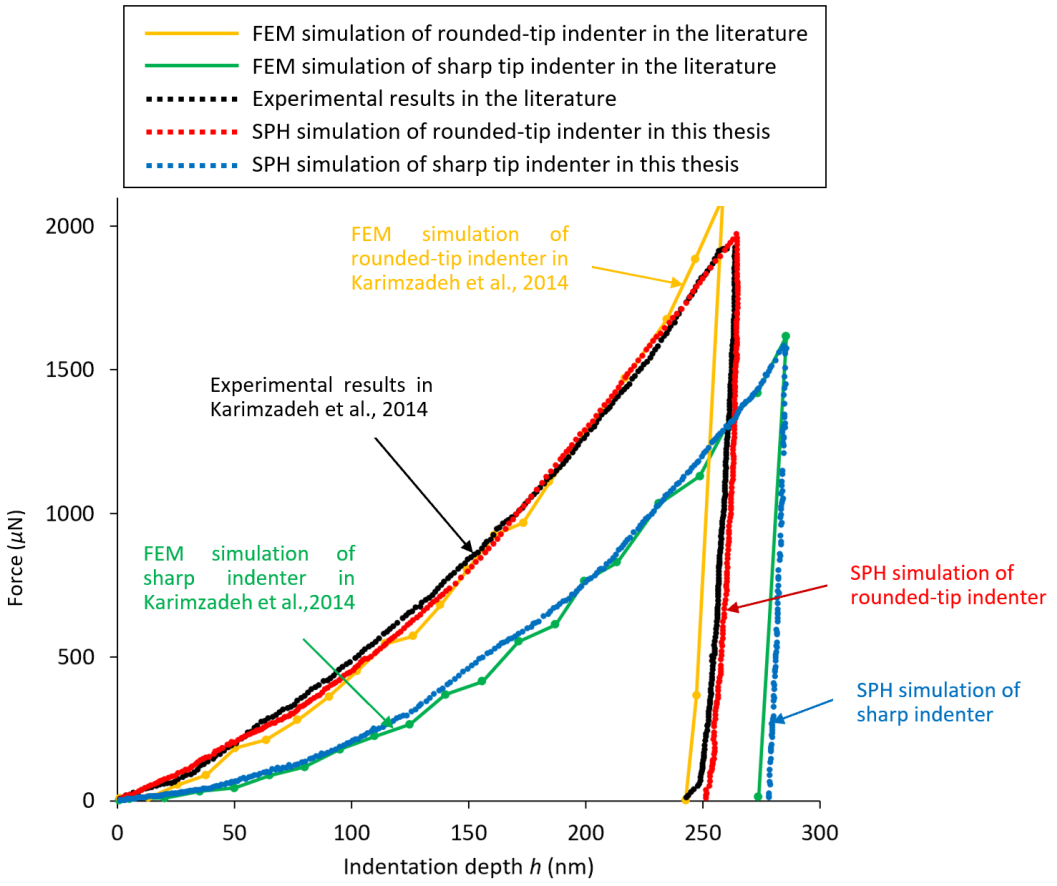

Fig. 4.17. nano-indentation responses obtained from SPH simulations and the literature.

Based on 1) the validation examination of the implemented SPH model of nano-indentation, 2) the benchmark study in the context of micro-indentation and 3) the investigation of the influence of indenter tip on material responses, it can be said that the implemented SPH model can be used to predict the resultant force during nano-indentation, especially during the loading process, and investigate the influence of simulation conditions on material response during nano-indentation. However, the influence of loading/unloading speed on unloading response needs to be further investigated. In reality, the unloading process may not always be considered as highly important when it comes to the simulation and prediction of nanoscale material deformation processes. Therefore, for all intents and purposes, it is suggested that the implemented SPH model can be used to simulate and investigate not only the nano-indentation process but that it represents a reliable basis to further model nanoscale machining, which is the focus of the next chapter.

4.6 Concluding remarks

This chapter aimed to address the first knowledge gap of interest, which is concerned with demonstrating the potential of the SPH method to model the material response during nano-indentation. To achieve this, an SPH model of nano-indentation reported in (Guo et al., 2015) was reproduced using the LS-DYNA software. Subsequent investigations included 1) the validation examination of the implemented SPH model of nano-indentation, 2) the benchmark study of the implemented SPH model in the context of micro-indentation and 3) the investigation of the influence of indenter tip on material responses.

For the validation examination of the implemented SPH model, the predictions obtained matched well with the results in (Guo et al., 2015) from three aspects. First, regarding the force-displacement response, the percentage differences between SPH

predictions and experimental results were within reasonable and acceptable range. Compared with the SPH simulation results in (Guo et al., 2015), the SPH predictions obtained in this chapter were closer to the reported experimental results during the entire nano-indentation process, especially when the indentation depth exceeded 400 nm. Second, the distribution patterns of Von Mises stress and plastic strain were in good agreement with those in (Guo et al., 2015), and the percentage differences of the maximum Von Mises stresses at different indentation depths were within 7% with a relatively large indentation depth. Third, the variation in the influence depth and the region where indentation-induced stress exists was verified to be consistent with that in (Guo et al., 2015) by comparing the average value of a pre-defined variable *k*. These three aspects of observation validated the accuracy of the reproduced SPH model of nano-indentation.

It is important to clarify that, based on the investigations presented by Guo et al. (2015), additional investigations were conducted, primarily focusing on three areas. First, additional details related to the simulations presented by Guo et al. (2015), including material properties, contact models, indentation speed and inputs into LS-DYNA, have been incorporated into this chapter to enhance clarity and understanding of the SPH model of nano-indentation reported in the existing literature. Second, the SPH model was applied to two additional cases involving hard metallic workpiece materials to provide further evidence that SPH simulations are viable in micro- and nano-indentation applications. Third, a convergence study of the SPH nano-indentation model in (Guo et al., 2015) was discussed in section 3.4, including the influence of particle density (particle number), to establish the nature of accuracy level. Stable responses and convergent parameters regarding particle density were achieved. This point was not discussed in (Guo et al., 2015) but was essential to ensure the level of accuracy of the SPH model.

The accuracy of the implemented SPH model of nano-indentation was further established and refined in the context of the micro-indentation study reported in (Dao et al., 2001). For the loading part of micro-indentation, the SPH model-based simulation results compared well with the FEM-predicted and experimental results. For the unloading part, the slope of the unloading curve and the residual depth decreased as the loading/unloading speed decreased. The material model derived from compression or tensile tests was seen to be an influential factor leading to the difference of sensitivities between loading and unloading curves.

For the investigation of the influence of indenter tip on nano-indentation responses, the SPH outcomes compared well with the FEM predictions and experimental results reported in (Karimzadeh et al., 2014) on an aluminum 1100 workpiece, for both sharp-tip indenter and round-tip indenter. The force-displacement response obtained with the implemented SPH model was generally closer to experimental results and compared well with the FEM predictions in (Karimzadeh et al., 2014). These observations provide enhanced confidence about the reliability of the SPH simulation of the nano-indentation process and investigation of the factors that influence the nano-indentation process using the SPH method.

In summary, the feasibility study conducted in this chapter suggests that the SPH method has the potential to model the nano-indentation process with reliable accuracy. This work lays the foundations towards developing a more comprehensive SPH model of nanoscale deformation processes in chapter 5 and chapter 6. The next chapter, which builds on the results gained in this chapter, extends the complexity of the implemented SPH model by considering the influence of the lateral motion between the indenter and the sample following initial nano-indentation.

Chapter 5 The effect of constitutive material models on SPH modelling of nano-machining

5.1 Overview

The main objective of this chapter is to compare the influence of adopted constitutive material models on the simulated cutting and normal forces as well as the machined topography during nano-machining. This chapter aims to address the second knowledge gap identified in this Thesis. According to the literature review in chapter 2, among the research efforts dedicated to the SPH simulation of nano-machining on metallic substrates, the majority of the work dealt with implementing the Johnson-Cook model to describe the flow stress of the machined material. In this chapter, a comparison of material responses during nano-machining of copper is reported when the process is simulated using SPH with two different material models, namely the Johnson-Cook and the elasto-plastic models. To achieve this, the next section starts with the reproduction of an SPH model of nano-machining in existing literature published by Islam and co-workers (Islam et al., 2012; Islam and Ibrahim, 2011). These two particular research studies were selected as benchmarks because they not only investigated the effects of nano-machining conditions on material responses using SPH but also provide comprehensive experimental data to compare with. The following section investigates the simulation results based on the following three aspects: (1) cutting and normal forces with different material models and depths of cut, (2) effect of the cutting speed on forces and its dependence on adopted material models and (3) effect of adopted material models on the surface topography of machined nano-groove. Overall, the simulation results show that the selection of the Johnson-Cook model is preferable for the SPH modelling of the nano-machining process. The final section presents the concluding remarks of this chapter.

5.2 SPH modelling of the nano-machining process

Following the SPH modelling of the nano-indentation process in Chapter 4, this chapter extends the complexity of the implemented SPH model by considering the influence of the lateral motion between the indenter and the sample. This motion, which results in the actual machining of nano-grooves, is restricted to a single line trajectory here. In the context of nano-machining of single nano-grooves, this chapter aims to address the second knowledge gap identified in this thesis, which is concerned with comparing the influence of adopted material models on the material response with a specific focus on the predicted surface profile of machined grooves.

Similar procedures as those already presented in chapter 4 were adopted here to reproduce an SPH model of nano-machining reported in existing literature (Islam et al., 2012). Among the research efforts in the field of SPH simulations of micro and nano-scale mechanical machining listed in Table 2.3, the SPH model and processing conditions for nano-machining used in (Islam et al., 2012) were selected as the benchmark in this chapter for the following reasons. First, copper is a more common material when studying micro and nano-scale mechanical machining, and it is the workpiece material employed in (Islam et al., 2012). Second, as mentioned in section 2.4, the prediction of surface profile on metallic materials is an essential objective in the simulation of nano-scale machining and in the fabrication of nano-grooves. In (Islam et al., 2012), Islam and co-workers simulated the nano-machining process on copper and investigated the effects of nano-machining conditions on material responses. There was also an experimental work conducted by the same authors with a specific focus on the surface profile of machined grooves reported in (Islam and Ibrahim, 2011). In addition, the experimental data of the surface profile of machined grooves reported in (Islam and Ibrahim, 2011) is more comprehensive than those in (Leroch et al., 2016; Varga et al., 2017) which were already listed in Table 2.3, and thus judged to be more reliable to validate the SPH simulations conducted in this thesis.

Therefore, the second knowledge gap was studied in this chapter based on the experimental results in (Islam et al., 2012; Islam and Ibrahim, 2011). In particular, the SPH simulation results for cutting and normal forces in section 5.3 are compared with the experimental forces reported in (Islam et al., 2012). The simulated cross-sectional profiles of machined grooves in section 5.5 are compared against the experimental results reported in (Islam and Ibrahim, 2011).

The SPH model for nano-machining was reproduced with the LS-DYNA software, as illustrated in Fig. 5.1. A conical nano-indenter, instead of a Berkovich indenter, was modelled to move vertically into a copper workpiece to reach a given depth of cut, and then moved horizontally and parallel to the surface at this depth to generate a scratch. The dimension of the conical indenter was already listed in Table 3.3, and the indenter had the same tip radius of 100 nm as those used in nano-machining simulations and experiments in (Islam et al., 2012; Islam and Ibrahim, 2011). This diamond indenter had the same material parameters as those of the Berkovich indenter used in Chapter 4. The copper specimen had dimensions of $10 \times 10 \times 0.8\ \mu m^3$. Only the first half length of the specimen is displayed in Fig. 5.1. As mentioned earlier, the flow stress of the copper workpiece material was described using two different approaches for comparison purpose, namely the Johnson-Cook and the elasto-plastic material models. The material model 15 "*Mat_Johnson_Cook" and material model 3 "*Mat_Plastic_Kinematic" in LS-DYNA were employed to represent the plastic behaviour for the OFHC copper workpiece, and the parametric values used in the present simulations were listed in Table 3.1 and Table 3.2.

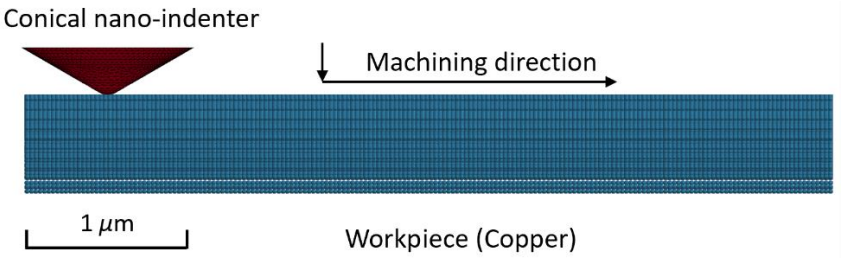

Fig. 5.1. SPH simulation model for nano-machining

The indenter was designed, constructed and meshed in the ANSYS environment first using a FE meshing scheme, and then imported into the LS-DYNA software. The workpiece was discretised solely using SPH particles with LS-DYNA. In order to improve the computational efficiency without sacrificing the accuracy of simulation results, the copper workpiece was discretised by SPH particles with varying densities. In particular, the discretisation of the workpiece was made finer in and around the vicinity of the machining area and coarser in proximity of the bottom and side boundaries of workpiece. Thus, the radius of SPH particles within the workpiece varied from 0.02 μm to 0.1 μm. The three layers of SPH particles at the bottom of the copper workpiece were fixed in the whole six degrees of freedom.

A machining speed of 10 m/s was chosen for most simulations, except when studying the influence of machining speed, reported later in section 5.4, for which three different simulated machining velocities were investigated, namely 100 m/s, 10 m/s, and 1 m/s. It is acknowledged that these values are higher than those typically encountered during nano-machining experiments, especially when nano-machining is implemented on Atomic Force Microscope instruments. However, as mentioned in the previous chapter, the use of a higher range of cutting speed in this thesis for reducing computational time is deemed to be reasonable in terms of expected accuracy. In addition, the three selected values of simulated machining velocity also cover an acceptable range of velocities for the SPH-based micro and nano-scale mechanical machining reported in the literature in section 2.3.4.

5.3 Analysis of forces during nano-machining

In this section, the influence of adopted material models on the machining forces was investigated by comparing the simulated cutting and normal forces. Fig. 5.2 and Fig. 5.3 display the comparison of simulated cutting and normal forces for the two different material models and two cutting depths (i.e. 100 nm and 150 nm). It can be seen from

these figures that for both constitutive models, the simulated normal force drops sharply from an original peak value and then stays relatively stable during the nano-machining process. This peak point at the beginning of machining corresponds the maximum force at the end of the initial nano-indentation step. The normal force during nano-machining is also always lower than the maximum normal force of nano-indentation. Regarding the simulated cutting force, after an initial sharp increase once the machining motion begins, the values reached generally show a slight increasing trend during nano-machining, but still remain lower than the normal force in all simulations. This is also the case for the experimental results. In addition, for both constitutive models, the simulated normal and cutting forces increase as the depth of cut increases, as observed with the experimental data. Despite discrepancies in the actual force values obtained between the simulated and experimental results, these are still within the same order or magnitude and can be considered to be in reasonable agreement. Thus, it can be said that the SPH model could be used as a suitable first approximation to predict the cutting and normal forces during nano-machining. It is also important to note that the material properties for the specific copper substate used in the experimental work discussed in (Islam et al., 2012) are not available. Hence it is not feasible to perform an exact quantitative comparison with the experimental data reported here.

It can also be seen from Fig. 5.2 and Fig. 5.3 that the experimental normal forces vary significantly more than those obtained with SPH. This is likely to be caused by inherent material defects and the possible influence of surface topography in practice. It is reported in (Islam and Ibrahim, 2011) that the copper specimens were obtained following several preparation processes, including electro discharge machining, polishing, ultrasonic cleaning, and electroplating. These techniques may introduce some material defects (such as cracks) and side effects (such as hardening) in the workpiece. In addition, the nano-machining experiments were performed using the

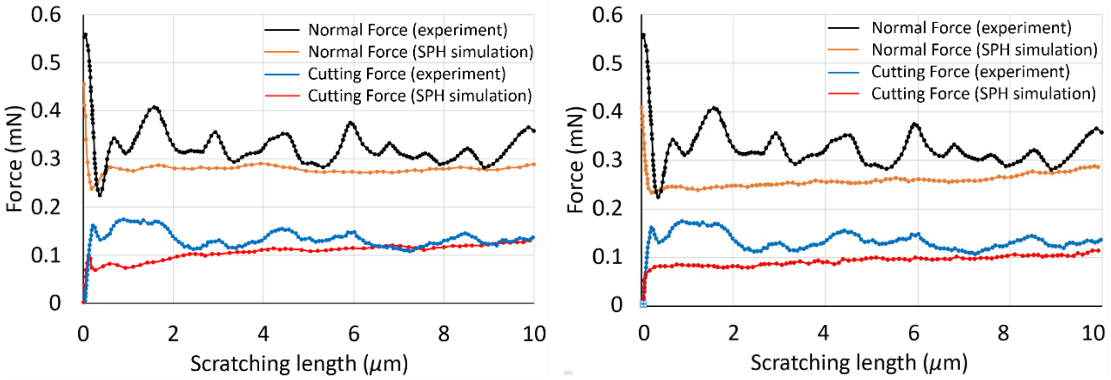

(a) (b)

Fig. 5.2. Simulated and experimental forces for 100 nm depth of cut using (a) a Johnson-Cook model and (b) an elasto-plastic model.

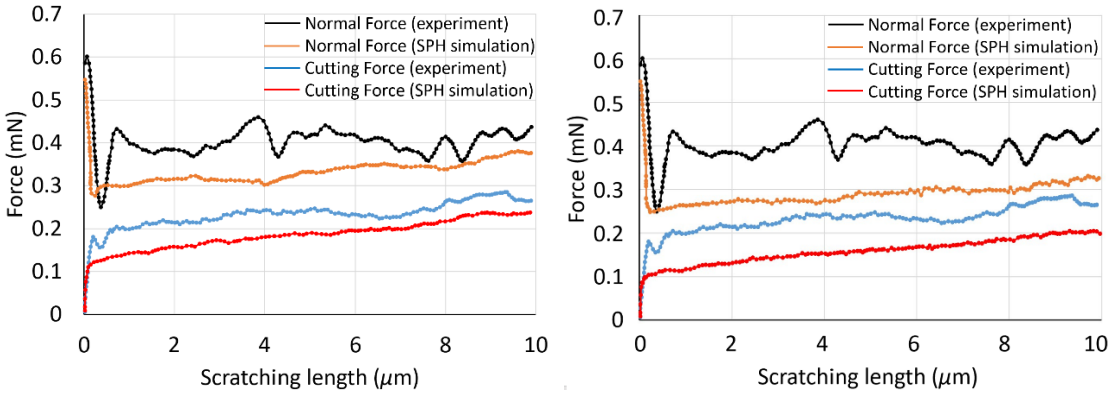

(a) (b)

Fig. 5.3. Simulated and experimental forces for 150 nm depth of cut using (a) a Johnson-Cook model and (b) an elasto-plastic model.

displacement-controlled mode, which means that the depth of cut remained constant for a given nano-machining test. Due to the unpredictable location of material defects and the fact that the displacement-controlled mode was adopted, the experimental normal force is likely to undergo some degree of fluctuation. The normal force fluctuation obtained with SPH simulations is more negligible due to the finer discretisation in the contact area and the fact that defects and surface topography are not taken into account.

One possible reason behind the fact that simulated forces were always lower than the experimental ones may be due to the absence of contact friction in the SPH model.

Another likely contributing factor behind this observation should be related to the lateral size effect (LSE). In particular, Kareer et al. (2016) reported the existence of the LSE for nano-machining on single crystal copper whereby the scratch hardness increases with the reduction in the depth of penetration of the indenter. It is important to highlight that the LSE was not incorporated in the SPH model of nano-machining used in this paper and that this should be the focus of future investigations.

With respect to the comparison of the simulated cutting and normal forces between the two material models, it can be seen that these are slightly smaller in the case of the elasto-plastic model when compared with those obtained using the Johnson-Cook model. This means that the discrepancy between simulated and experimental forces is larger when using the elasto-plastic constitutive model.

5.4 The effect of cutting speed

In addition to the influence of adopted material models on the machining forces, the effect of cutting speed and its dependence on adopted material models are discussed in this section. Fig. 5.4 and Fig. 5.5 illustrate the effect of the cutting speed and material model on the simulated normal and cutting forces. The three cutting speeds chosen, 100 m/s, 10 m/s and 1 m/s, were simulated for a depth of 150 nm for both constitutive models. Although these machining speeds are higher than typical experimental velocities as discussed earlier, it can be said that the general trend is still reasonable when considering the Johnson-Cook material model. In particular, it can be seen from Fig. 5.4 (a) and Fig. 5.5 (a) that the cutting and normal forces become larger as the cutting speed increases. This is attributed to the fact that the Johnson-Cook material model is strain rate sensitive. It should be noted that these observations are also consistent with the simulation results reported by (Guo et al., 2017). In contrast, this strain rate dependance is not observed, as expected, when using the elasto-plastic material model (see Fig. 5.4 (b) and Fig. 5.5 (b)).

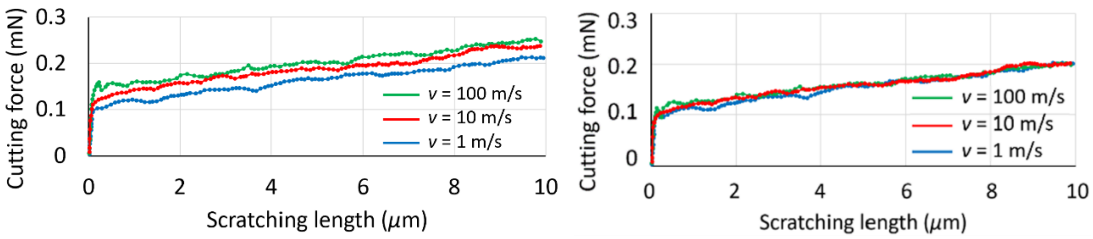

(a) (b)

Fig. 5.4. Effect of speed on cutting force for 150 nm depth of cut using (a) a Johnson-Cook model and (b) an elasto-plastic model.

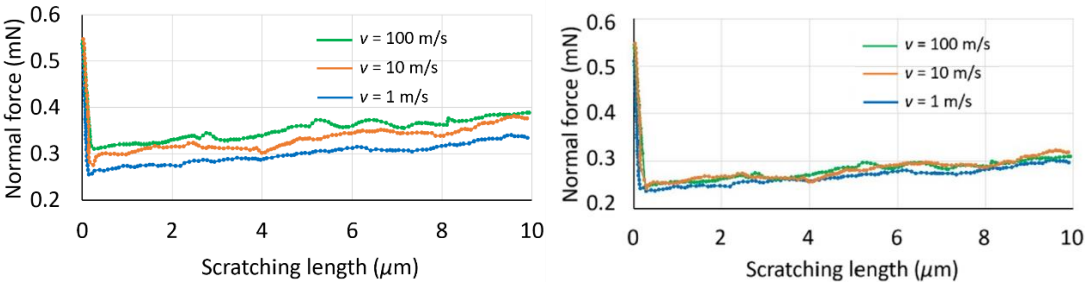

(a) (b)

Fig. 5.5. Effect of speed on normal force for 150 nm depth of cut using (a) a Johnson-Cook model. and (b) an elasto-plastic model.

It can also be noted from Fig. 5.4 that the cutting force increases gradually with the increasing machining length. The possible reasons could be the occurrence of pile up and material accumulation in front of the indenter during nano-machining. In particular, the simulated surface topography, reported next in section 5.5, shows that the machining width and volume of pile up increase with the machined length.

5.5 Machined surface profile during nano-machining

In this section, the influence of adopted material models on the predicted surface profile of machined grooves is studied. Fig. 5.6 shows the simulated machined surface topographies at a cutting depth of 150 nm for both material models. In both cases, a machined groove is formed along the machining direction and pile-ups are also generated on both sides of the cut groove. It is also observed in Fig. 5.6 (a) that a few SPH particles separated away from the surface. This unrealistic result may be

attributed to the large machining speed used in the simulations. However, this phenomenon is not obvious in Fig. 5.6 (b). This is because the values of yield stress and tangent modulus for the elasto-plastic model were chosen by different combinations of those found in literature to obtain a machined surface with a minimum number of SPH particles which separated from the surface. Therefore, the separated particles in Fig. 5.6 (a) could also be related to the values of the parameters used in Table 3.1 which can be more fine-tuned in the future. It can be also seen from Fig. 5.6 that no obvious crack and chip are identified along the machined groove. Therefore, the ploughing mechanism was the dominant mode of surface generation for these nano-machining simulations. This is also in line with the fact that, for the corresponding simulation data reported in Fig. 5.3 earlier, the values of the normal force were always higher than those of the cutting force.

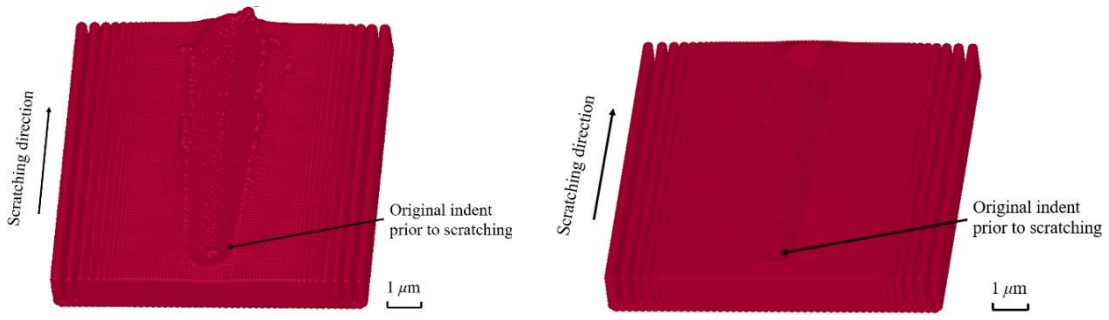

(a) (b)

Fig. 5.6. 3D view of machined surface at 150 nm depth of cut using (a) a Johnson-Cook model and (b) an elasto-plastic model.

Fig. 5.7 shows the two-dimensional cross-sectional profiles of the machined grooves which were simulated in Fig. 5.6. These cross-sectional profiles can be visualized using the LS-Prepost software. The simulated grooves illustrated in Fig. 5.7 have been scaled down unidirectionally only in the width direction (with a reduction ratio of 1:3) for clarity purpose. The nodal coordinates of interest were obtained from Fig. 5.6 at a

machining length of 5 μm. This length corresponds to the mid-point of the total machining distance and is considered to be a reasonable location to obtain a representative profile of the simulated nano-grooves. It can be seen that the geometry of the pile-up on both sides of groove is almost identical due to the axi-symmetric shape of the conical indenter. Fig. 5.8 presents a slightly magnified geometries of the cross-sectional profiles from Fig. 5.7, where experimental results found in (Islam and Ibrahim, 2011) are also superimposed. It can be seen from this figure that the machining width at the cutting length of 5 μm using the Johnson-Cook model is 1.62 μm, slightly larger than the experimental value of 1.24 μm, while the simulated machining depth is 114 nm, very close to the experimental value of 112 nm. The percentage differences of groove width and groove depth are 31% and 2%, respectively for the Johnson-Cook model when compared to the experimental data from (Islam and Ibrahim, 2011). In the case of the elasto-plastic model, the machining width and depth are 1.84 μm and 101 nm. This represents percentage differences of 48% and 10%, respectively, against the experimental groove dimensions. In addition, Table 5.1 presents the machining depth and width for different material models and different machining distances at intervals of 2 μm. The consideration of this additional data aims to help reduce the error caused by the randomness of selecting a machining distance of 5 μm. The percentage differences of the averaged groove width and depth are 25% and 2%, respectively for the Johnson-Cook model when compared to the experimental data. While these two quantities are 44% and 11% for the elasto-plastic model. Therefore, it can be said that the cross-sectional profile of the simulated nano-groove using the Johnson-Cook model is closer to experimental results compared with that obtained using the elasto-plastic model.

(a) (b)

Fig. 5.7. Cross-sectional profile of machined nano-groove at 150 nm depth of cut using (a) a Johnson-Cook model and (b) an elasto-plastic model. (with a scaling ratio of 1:3 in the width dimension)

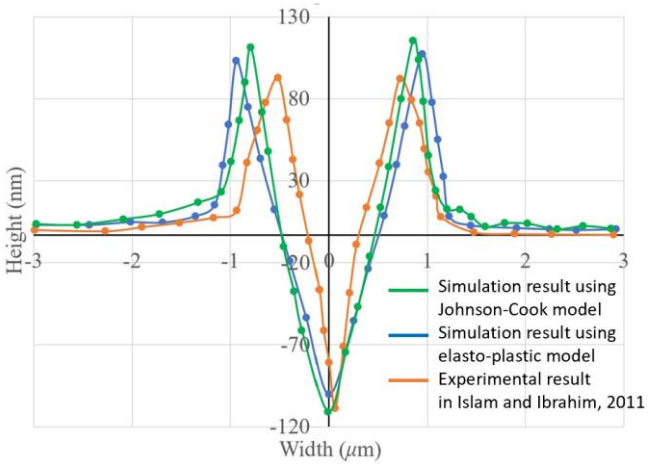

Fig. 5.8. Comparison of cross-sectional profiles of machined nano-grooves.

Table 5.1. Machining depth and width for different material models and machining distances.

Machining distance (μm)	Johnson-Cook model		Elasto-plastic model	
	Machining depth (nm)	Machining width (μm)	Machining depth (nm)	Machining width (μm)
2	109	1.32	98	1.56
4	117	1.54	100	1.82
6	115	1.66	103	1.88
8	116	1.68	100	1.89
Averaged value	114	1.55	100	1.79
Experimental dimensions	112	1.24	112	1.24
Percentage difference	2%	25%	11%	44%

5.6 Concluding remarks

This chapter aimed to address the second knowledge gap which motivated this research. This knowledge gap is concerned with comparing the influence of adopted material models on the material response with a specific focus on the predicted surface profile of machined grooves. A nano-machining model of copper was implemented using SPH to complement existing literature with a specific view to study the influence of the selected material constitutive model. This was achieved by considering the Johnson-Cook and an elasto-plastic model and by analysing their effect on the simulated cutting and normal forces as well as on the surface topography of machined nano-scale groove. The simulated data were also compared against experimental results available in the literature.

Some conclusions that were drawn from this chapter are summarised as follows.

- As expected, the cutting and normal forces increased as the machining speed increased when using the Johnson-Cook constitutive model while the machining speed had no influence on the simulated forces in the case of the elasto-plastic material model.

- The utilisation of the Johnson-Cook constitutive model in the SPH simulations led to cutting and normal forces which were higher than those obtained with the elasto-plastic model and closer to those observed experimentally.

- The cross-sectional profile of simulated nano-groove using the Johnson-Cook model was also closer to experimental results compared to that obtained when implementing the elasto-plastic model. For this reason, and also based on the analysis of the simulated forces, it can be said that the selection of the Johnson-Cook model is preferable for the SPH modelling of the nano-machining process.

This chapter also verified the feasibility of the SPH method to simulate the nano-machining process. This work lays the foundations towards developing a novel SPH model in the context of AFM tip-based dynamic ploughing lithography (DPL) in the next chapter. In particular, such SPH model for simulating AFM tip-based DPL should enable the modelling of nanoscale dots and grooves, which are the result of vibrating the indenter in vertical direction while machining in the horizontal direction.

Chapter 6 SPH modelling of AFM-based dynamic ploughing lithography

6.1 Overview

The main objective of this chapter is to address the third knowledge gap of interest in this Thesis. This knowledge gap is concerned with simulating AFM probe-based dynamic ploughing lithography (DPL) using the SPH method with a view to further reveal machining mechanisms and to predict the surface generation process. As discussed in Chapter 2, dynamic ploughing lithography conducted with an AFM instrument is a promising machining technique for fabricating nano-scale surface structures. However, none of the SPH-based studies reported in Chapter 2 focused on simulating this specific process. To achieve the aim of this chapter, Section 6.2 starts by the development of an AFM-based DPL model with the SPH method. This original SPH model is developed such that its results can be compared to an already existing AFM-based DPL model presented by Xiao et al. (2019) but deployed using MD simulation. Next, in Section 6.3 and at the beginning of Section 6.4, the SPH-predicted results are compared with those of the published MD simulation study with respect to two aspects. These are 1) the quantitative comparison of the forces during DPL and 2) the qualitative comparison of the simulated surface topography. For the rest of Section 6.4, the SPH-predicted surface topographies were then qualitatively investigated from the following three aspects: (1) the influence of the vibration amplitude on dimensions of the simulated nano-grooves, (2) the presence of periodic nanostructures simulated with vibration periods ranging from 0.4 nm to 4 nm and (3) the evaluation of the profile of periodic nanostructures along two different viewing directions. In Section 6.5, the influence of the vibration period on the roughness profile and roughness value was investigated for periods smaller than 1 nm. This value was selected in this section because the waviness profile with longer wavelengths was introduced with periods larger than 1 nm and this could affect the calculation of the roughness value. The final section presents the concluding remarks of this chapter.

6.2 SPH model of AFM-based dynamic ploughing lithography

Dynamic ploughing lithography conducted with an AFM instrument is a promising mechanical machining technique for fabricating nano-scale surface structures. Based on the SPH study of nano-scratching presented in Chapter 5, this section now aims to present the development of a novel SPH model in the context of AFM probe-based DPL. As mentioned in Section 2.2, with AFM-based DPL, the cantilever of the AFM probe is driven to oscillate in the vertical direction at a high frequency while scratching in the horizontal direction. This motion can be employed to produce nano-grooves and more complex structures such as nano-dots.

One machining process similar to AFM-based DPL is vibration assisted nano machining. Vibration assisted nano machining is a machining method in which external vibrations are applied to the workpiece in order to address issues related to the traditional micro and nano-scale tip-based material deformation process, such as large cutting forces, excess tool wear, slow machining speed and low throughput. For example, utilising ultrasonic vibration assisted micro machining, the achievement of ductile cutting in the processing of brittle materials was realised, while also leading to a reduction in cutting forces experienced during the diamond cutting operations (Zhou et al., 2002). Park et al. (2014) applied planar vibrations to the workpiece to generate an elliptical motion in the XY plane while implementing AFM probe-based nano-scale machining. The authors found that the incorporation of XY planar vibration assisted machining significantly enhanced the efficiency and accuracy of fabrication. This improvement was achieved by decreasing the tool's interaction time with the workpiece and the instantaneous depth of cut. Geng et al. (2018) integrated high frequency reciprocating motions of the workpiece, which was realised by a piezoelectric actuator, into a commercial AFM instrument. The introduction of high frequency reciprocating vibrations into the workpiece realised a theoretical cutting speed over 5 m/min at the tool-workpiece interface and thus enhanced the throughput of the AFM probe-based

nano-scale machining. Although AFM probe-based DPL only involves high frequency vibration of the AFM probe in the vertical direction, it shares similarities with vibration assisted nano machining in terms of the aim of improving the machining process by introducing high frequency vibrations. More specifically, as discussed in Chapter 2, the high frequency vibration of the AFM probe in AFM-based DPL could reduce the interaction force between the tip and sample, alleviate the tip wear and weaken the influence of the lateral force on the variation of cantilever deflection.

In order to help evaluate the output of the SPH model developed in this work, the AFM-based DPL model reported in (Xiao et al., 2019) by Xiao and co-workers, which is based on MD simulation, was selected as the benchmark study.

Fig. 6.1 shows the schematic diagram of the AFM-based DPL process investigated in this chapter. The AFM tip, mounted at the free end of the cantilever, serves as the nano-scale cutting tool. In practice, the cantilever is driven by a piezoelectric actuator to generate the vertical vibration of the probe. At the same time, the AFM probe is actuated to move horizontally in the direction parallel to the sample surface. The coordinate system to describe the tip motion was defined in such a way that the x-axis provided the direction of horizontal machining, and that the z-axis was the vertical direction, i.e. perpendicular to the workpiece surface. The direction of the y-axis conformed to the right-handed rule. The origin of the coordinate system was taken at the tip of the AFM probe. It should be noted that this defined coordinate system (see Fig. 6.1) was employed for all the SPH models of AFM-based DPL in this chapter. The AFM tip shape was a trirectangular tetrahedron, which can be seen as a corner of a cube in Fig. 6.2. This trirectangular tetrahedron has three edges with length of 5.7 nm, three base lengths of 8.06 nm, three faces with right angle triangles, and a height of 3.29 nm. Here, the height refers to the distance between the vertex and the base face of the AFM probe. The workpiece was made of single crystal copper with dimension of $20 \times 18 \times 12$ nm^3.

The AFM probe was simulated to vibrate with a high frequency in the vertical direction while machining with a constant speed in the horizontal direction, resulting in a sinusoidal tool trajectory. It should be noted that the mathematical expression of this sine curve was not reported in (Xiao et al., 2019). Thus, this expression was extracted from the data provided in Fig. 2 in (Xiao et al., 2019). Based on this analysis, it was found that this sinusoidal curve could be expressed as follows:

$$\begin{aligned} x &= v_x \cdot t \\ z &= \frac{A}{2}\sin\left[\frac{2\pi}{T}\left(x + \frac{T}{4}\right)\right] - \frac{A}{2} \end{aligned} \tag{6.1}$$

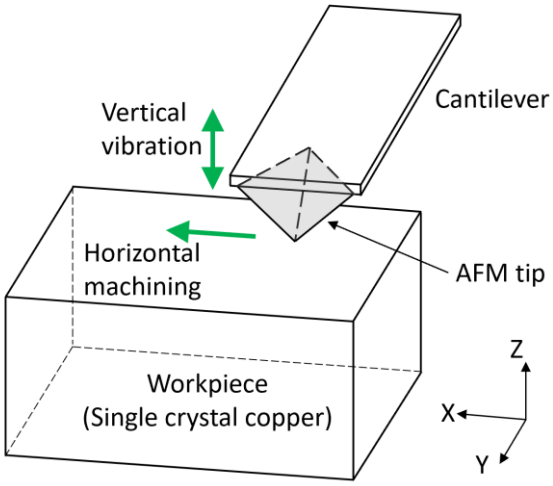

Fig. 6.1. Schematic diagram of AFM-based dynamic ploughing lithography.

For the initial purpose of comparing the outcome of the model developed in this work with that of (Xiao et al., 2019), the value of the simulation parameters in equation (6.1) are listed in Table 6.1. Therefore, the mathematical expression of the tool trajectory can be expressed as that in equation (6.2). This equation also indicates a vertical vibration speed of 80 m/s for the AFM probe tip. Considering that the original location

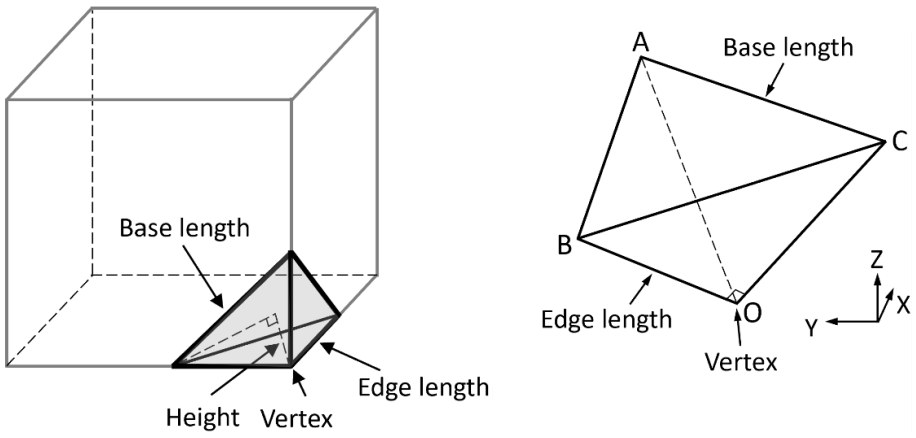

Fig. 6.2. (a) A corner of a cube to illustrate the shape of a trirectangular tetrahedron. (b) The AFM probe with the shape of a trirectangular tetrahedron employed in this chapter.

of the AFM probe tip was 1 nm above the workpiece and that its vibration amplitude was 4 nm, the depth of dynamic ploughing was 3 nm. The total ploughing distance simulated in (Xiao et al., 2019) was 8 nm. It should be noted that the vibration period in Table 6.1 represents the period of length when characterising the periodicity of the triangular wave tool trajectory, as conventionally employed in the existing literature.

Table 6.1. Simulation parameters of the tool trajectory.

Parameters	Value
Horizontal speed v_x	2 m/s
Simulation time t	0-4 ns
Vibration amplitude A	4 nm
Vibration period T	0.2 nm

$$\begin{aligned} x &= 2t \ \ (nm) \\ z &= 2\sin(10\pi x + 0.5\pi) - 2 \ \ (nm) \end{aligned} \tag{6.2}$$

In initial simulations trials, it was found that the computing time needed when using a sinusoidal tool trajectory was about 1.5 times longer than that when using a tool trajectory of a triangular wave. Considering that more than 30 sets of SPH simulations

were performed in this chapter, a triangular wave tool trajectory was finally selected to approximate the sinusoidal tool trajectory. Future investigations should be carried out on 1) the reason of different simulation time caused by different prescribed motions as input in LS-DYNA and 2) SPH simulations of AFM-based DPL using a tool trajectory of sinusoidal curve.

The AFM probe tip was made of diamond and had the same material parameters as those of the Berkovich indenter used in Chapter 4. According to the conclusions made in Chapter 5, the selection of the Johnson-Cook model is preferable for the SPH modelling of the nano-scratching process on copper compared to the elasto-plastic model. Therefore, the material model 15 "*Mat_Johnson_Cook" in LS-DYNA was employed to represent the plastic behaviour for the OFHC copper workpiece, and its parameter values were already listed in Table 3.1. Fig. 6.3 shows the implemented SPH model of AFM-based DPL in the ANSYS/LS-DYNA software. The workpiece was discretised by SPH particles with varying densities using the same distribution pattern as that in Chapter 5. The three layers of SPH particles at the bottom of the OFHC copper workpiece were fixed for the whole six degrees of freedom.

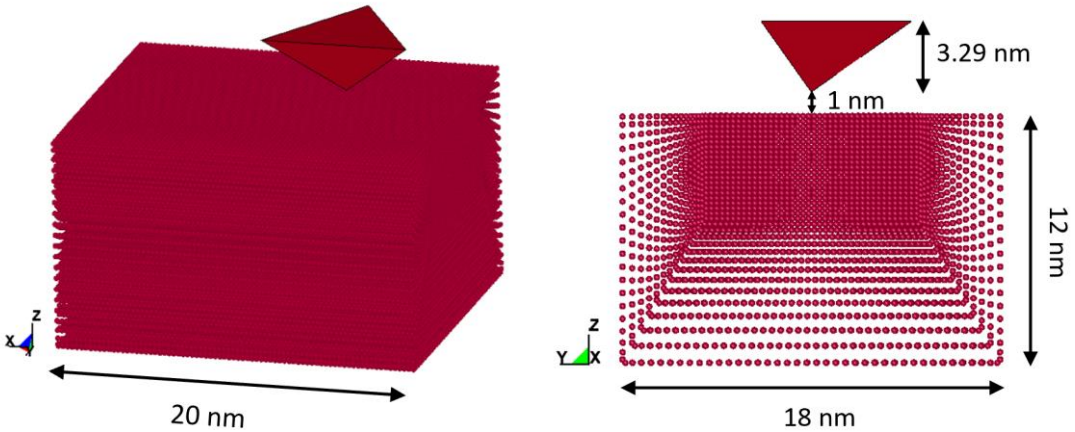

(a) (b)

Fig. 6.3. SPH model of AFM-based DPL (a) the top view and (b) the front view.

6.3 Force analysis

The forces obtained in the dynamic ploughing simulations are presented in Fig. 6.4 to Fig 6.6 for a vibration period of 0.2 nm. It should be noted that the resultant force was sampled and recorded at each peak and valley of the triangular tool trajectory in LS-DYNA. Therefore, the curve of sampled resultant forces in Fig. 6.4 showed a triangular waveform. Similar observations were made for the cutting force component and normal force component. It can also be seen from Fig. 6.4 that the resultant force initially increased sharply before decreasing to a stable fluctuation with a peak value of 0.8 μN. The first peak in the normal force and resultant force corresponds the maximum impact force caused by the first nano-indentation process with an indentation speed of 80 m/s. In addition, the first peak in the normal force and resultant force was relatively large compared with the value of forces during the rest of the process. This may be because AFM-based DPL can be regarded as a series of successive nano-indentation processes, and thus the amount of material being processed during the first nano-indentation was much larger than those during subsequent nano-indentations due to the overlapping area of material being processed. In contrast, the cutting force was quite small at the end of this initial nano-indentation step, according to the first peak in Fig. 6.5. The period of forces in Fig. 6.4 to Fig 6.6 was equal to the period of dynamic ploughing lithography of 0.2 nm.

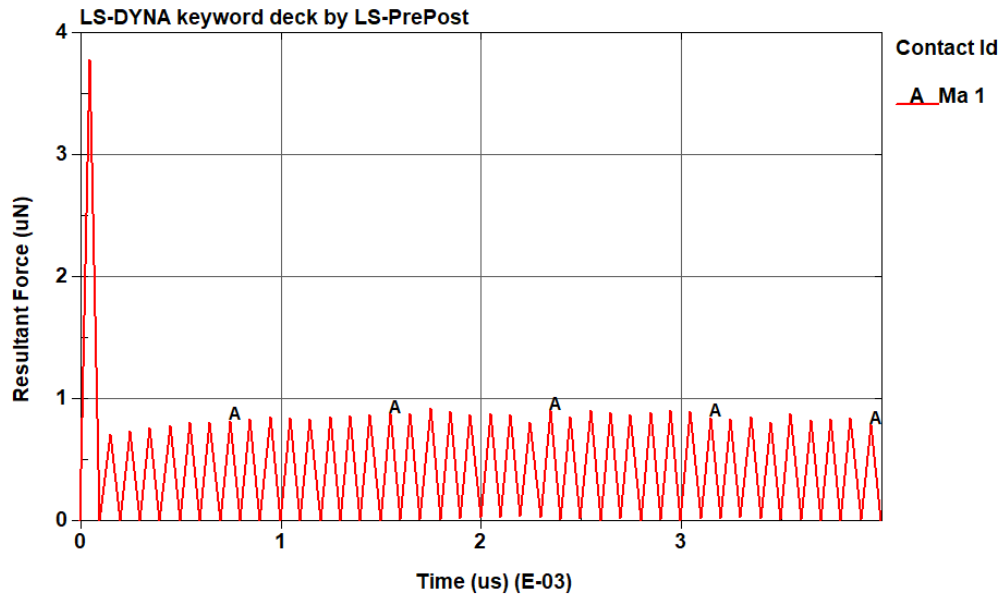

Fig. 6.4. Simulated resultant force during dynamic ploughing.

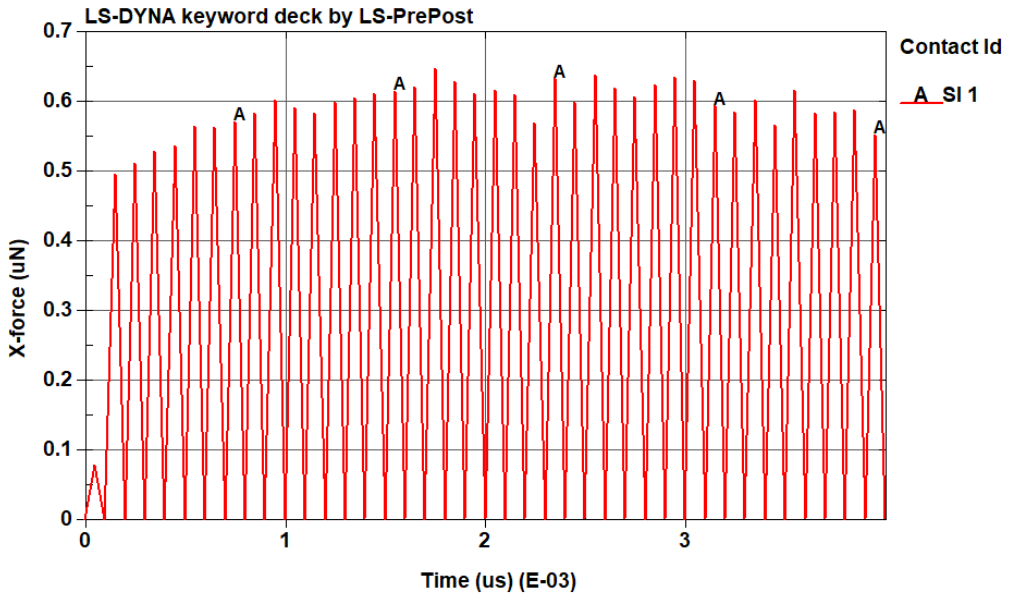

Fig. 6.5. Simulated cutting force during dynamic ploughing.

Several discrepancies between the simulated forces using SPH in this chapter and the MD simulation reported in (Xiao et al., 2019) were observed. First, as can be seen from Fig. 6.6, the normal force during dynamic ploughing simulated by SPH was positive, which was not the case for the MD predictions in (Xiao et al., 2019). In (Xiao et al., 2019), the normal force was negative when the AFM probe moved in the upward

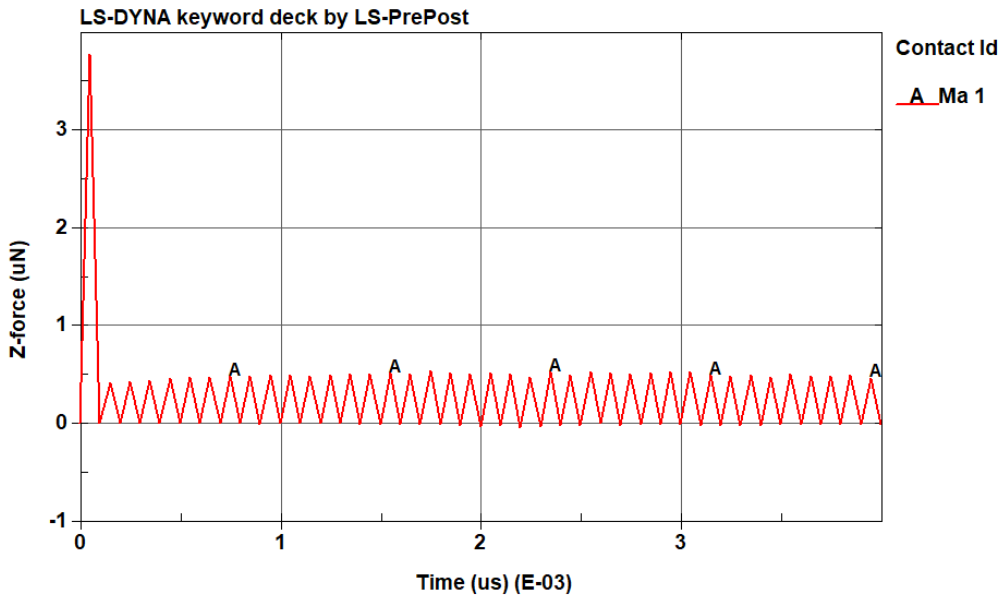

Fig. 6.6. Simulated normal force during dynamic ploughing.

direction, indicating the presence of material adhesion between the tip of the AFM probe and the workpiece material. Second, it is quite obvious that the simulated forces using SPH were much larger than those obtained using MD in (Xiao et al., 2019). Quantitative comparisons between the average SPH-predicted and MD-predicted resultant forces are given in Fig. 6.7. It can be seen that the average value of the SPH-predicted resultant force was 401 nN, significantly larger than the MD-predicted value of 65 nN, while the averaged peak value of the SPH-predicted resultant force was 801 nN, larger than the MD-predicted value of 239 nN. The ratios between the values of these two columns in Fig. 6.7 were 6.17 and 3.35, respectively. The MD-predicted resultant force in (Xiao et al., 2019) was not superimposed in Fig. 6.4 due to the obvious contrast between the SPH and MD-predicted values. Since the averaged values of the cutting force and normal force were not provided in (Xiao et al., 2019), only the resultant force was compared in Fig. 6.7.

The discrepancies between the SPH-predicted and MD-predicted forces could be related to the material models employed in these two numerical methods. First, the workpiece materials used were not exactly the same. The single crystal copper with a

crystal orientation of (0 0 1) was used as the workpiece material in the MD simulations in (Xiao et al., 2019), while the OFHC copper with Johnson-Cook parameters in Table 3.1 was employed in all of the SPH simulations throughout this chapter. Second, it is important to note that the material properties for the single crystal copper used in the MD simulations from (Xiao et al., 2019) are not available. Hence, it is not easy to perform an exact quantitative comparison with the MD results. Moreover, it was found in Chapter 2 that a single crystal copper workpiece was commonly used for MD simulations while for SPH simulations the OFHC copper was the most common of the metallic materials. Therefore, a question remains as to whether the Johnson-Cook parameters for the OFHC copper can be directly used in the SPH simulation of AFM-based DPL on a single crystal copper workpiece. It is emphasised that the reason for these discrepancies between the SPH-predicted and MD-predicted forces should be further investigated in order to potentially improve the predictability and reliability of the implemented SPH model of AFM-based DPL. Since the accuracy of the implemented SPH model for AFM-based DPL needs to be further validated, the subsequent investigations in the following sections are mainly qualitative.

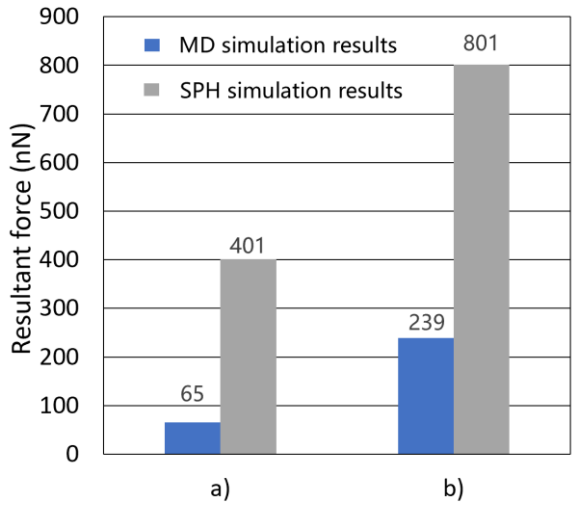

Fig. 6.7. Comparison of SPH-predicted and MD-predicted resultant force with respect to (a) averaged value of the resultant force and (b) averaged value of peaks of the resultant force.

6.4 Machined surface profile

6.4.1 Influence of the driving amplitude on the nano-groove dimensions

Fig. 6.8 shows the surface topography simulated with the SPH model for AFM-based DPL implemented in Section 6.2. The vibration amplitude and period of the AFM tip in this simulation were 4 nm and 0.2 nm, while the horizontal speed and simulation time remained that same as those listed in Table 6.1. It can be seen from Fig. 6.8 that apparent material accumulation was found at the end of the simulated nano-groove. Therefore, it could be said that ploughing was the dominant mechanism of surface generation for the simulated dynamic ploughing process, although it would be important to confirm this by simulating the process over a longer distance to confirm that. The SPH particles separated away from the surface are likely to be caused by the large simulation speed in the vertical direction (i.e. 80 m/s). In addition, material accumulation was observed on the right side of the AFM probe, which should be related to the asymmetrical geometry of the AFM probe along the direction of horizontal machining. These above observations of simulated surface topography are consistent with those in (Xiao et al., 2019).

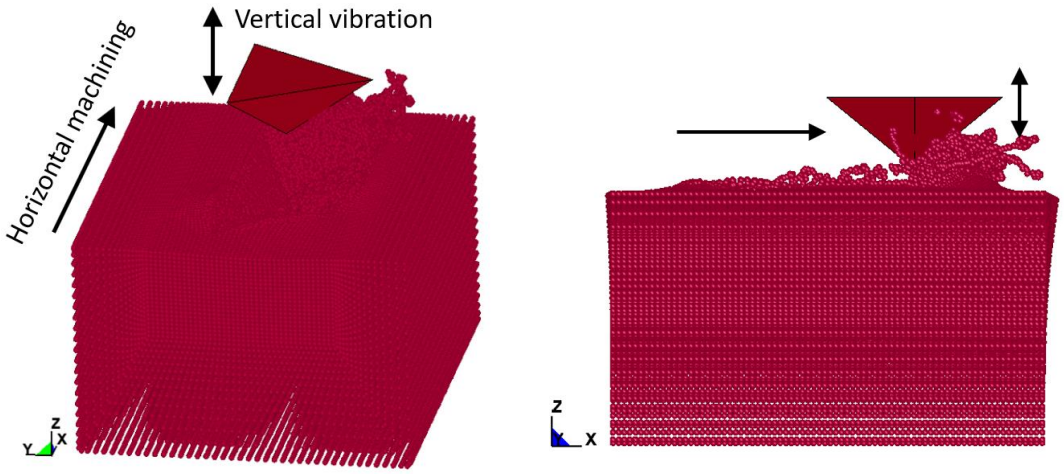

(a) (b)

Fig. 6.8. Simulated surface topography at the end of the dynamic ploughing lithography process (a) the front view and (b) the right view.

Fig. 6.9 shows the cross-sectional profiles of the simulated nano-grooves with four different amplitudes. It can be seen that the depth and width of the nano-groove increased as the amplitude of vertical vibration increased. The height of the pile-up slightly increased as the amplitude increased from 2 nm to 4 nm. Indeed, the heights of these pile-ups with vibration amplitudes of 4 nm and 5 nm were almost the same. This may be because the depth of cut with an amplitude of 5 nm is 4 nm (considering the initial gap of 1 nm between the tip and the workpiece), which is already larger than the height of the AFM tip (i.e. 3.29 nm). In this case, the effective height of the cutting tool equals the entire height of the AFM tip (see Fig. 6.3 (b)) and thus will not increase as the vibration amplitude increases. Therefore, the volume of removed material would not show an obvious increasing trend when the amplitude exceeds 5 nm. Fig. 6.10 presents the influence of vibration amplitude on the depth and width of the simulated nano-groove. It should be noted from Fig. 6.10 that the depth of the nano-groove simulated with an amplitude of 4 nm was 2.7 nm, which was larger than that obtained by the MD simulation in (Xiao et al., 2019) (i.e. 1.7 nm). This discrepancy indicates the difference in the simulated elastic recovery of the workpiece material and is likely to be caused by the different material models and parameters adopted in these two numerical methods. Similar to the discussion in Section 6.3, it is emphasised that the reason for this discrepancy between the SPH-predicted and MD-predicted groove depth should be further investigated in order to potentially improve the predictability and reliability of the implemented SPH model of AFM-based DPL.

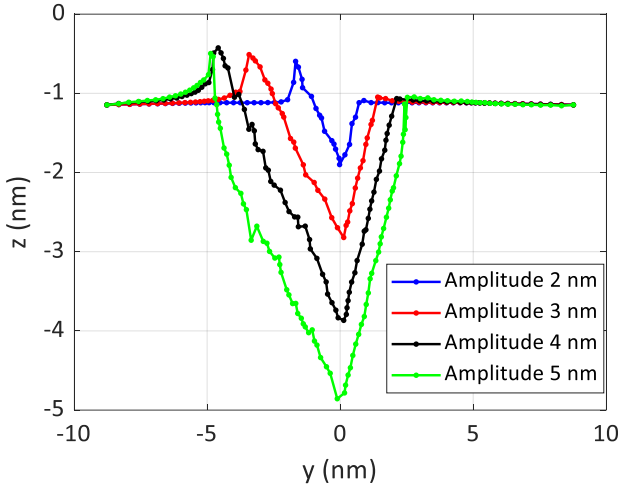

Fig. 6.9. Cross-sectional profiles of simulated nano-grooves with different amplitudes of dynamic ploughing.

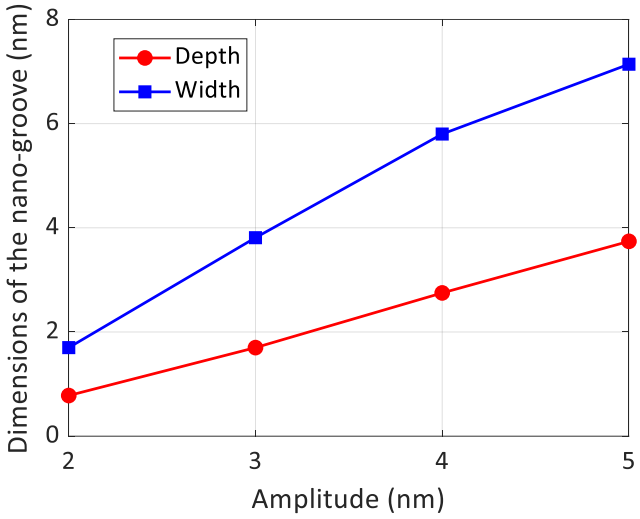

Fig. 6.10. Influence of the amplitude on dimensions of the simulated nano-grooves.

6.4.2 Influence of the period on the simulated surface topography

To investigate the influence of the period of the vertical vibration on the simulated surface topography, 20 sets of SPH simulations were performed with values of the period ranging from 0.2 nm to 4.0 nm, at intervals of 0.2 nm. Fig. 6.11 shows the top view of some representative simulated surfaces. It can be seen that periodic 3D nanostructures were observed on the bottom surface of the machined nano-grooves

along the machining direction. When the period of vertical vibration smaller than 1 nm, the phenomenon of periodic nanostructures was not obvious (as can also be seen in Section 6.5) and the simulated nano-grooves were quite similar to those obtained by nano-machining in the previous chapter. The possible reason behind this observation is that the period in this case was much smaller than the depth of dynamic ploughing (i.e. 3 nm) and the dimensions of the AFM probe. Therefore, the formation of periodic 3D nanostructures was difficult due to the geometry of the AFM probe. With periods larger than 1.0 nm, periodic 3D nanostructures were observed (see Fig. 6.11(c-h)). In this case, machined features can be regarded as overlapping nano-indents at intervals of the value of the period. Therefore, the period of these nanostructures should be the same as the period of the dynamic ploughing.

Several additional observations are noted in Fig. 6.11. First, ploughing was the dominant mechanism of surface generation for AFM-based DPL. There was no obvious chip formation during the dynamic ploughing lithography process. Despite the pile-up at the end of the machining process, its height was almost lower than 2 nm, that is, still lower than the height of the AFM tip (i.e. 3.29 nm). This observation is consistent with that displayed in Fig. 4 in (Xiao et al., 2019). Thus, it can be said that the dominant mechanism of material deformation during AFM-based DPL is ploughing. Second, the volume of pile-up at the end of the machining surface decreased as the period of dynamic ploughing increased. This may be because a larger volume of material was removed from the workpiece with a smaller period of vibration, leading to a larger volume of pile-up at the end of the machining surface. Third, for simulated surfaces with periods larger than 1.0 nm, material accumulation was observed on the left side of each edge of the nanostructure. One possible reason for this observation is that the AFM-based DPL with a relatively large period can be regarded as successive nano-indentation processes, and thus the material on the edges of the nanostructure was extruded by subsequent indentation processes and then accumulated on the left side of the edges. This phenomenon is displayed in a more apparent way in Fig. 6.13.

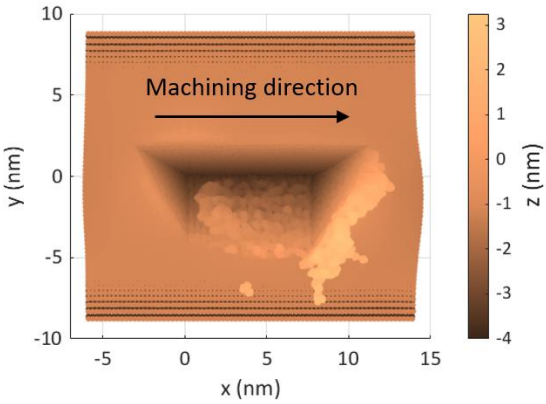

(a) T=0.4 nm

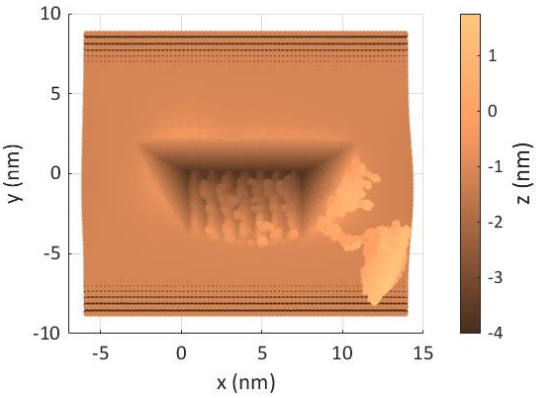

(b) T=1.0 nm

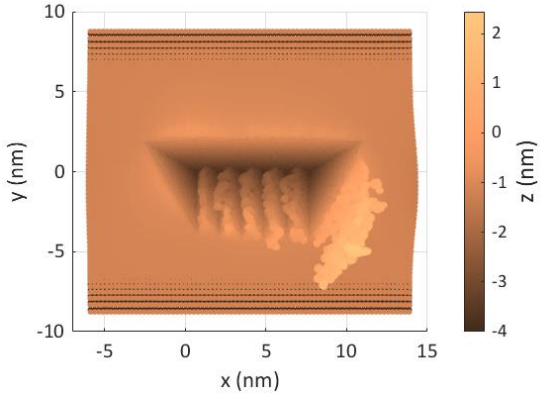

(c) T=1.4 nm

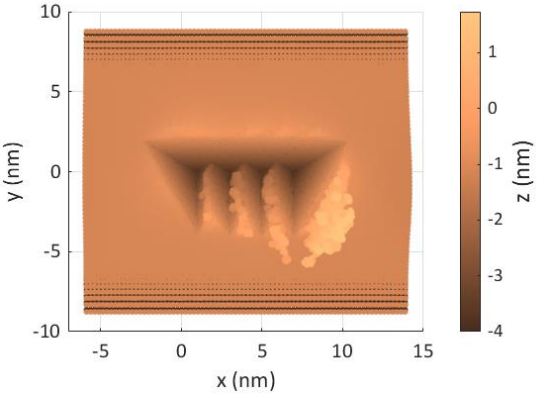

(d) T=2.0 nm

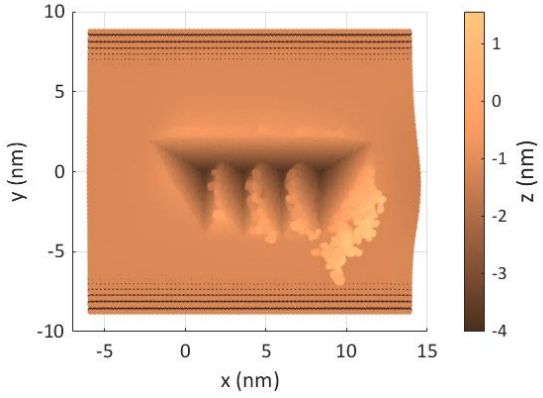

(e) T=2.4 nm

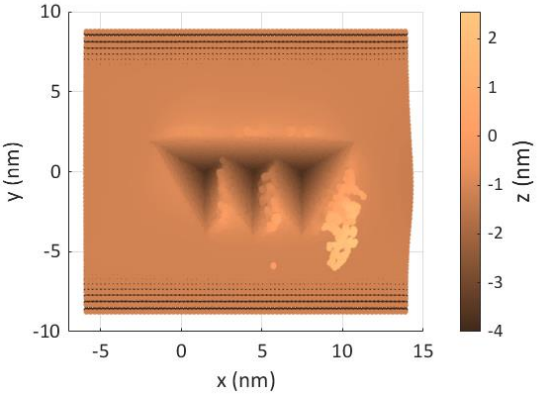

(f) T=3.0 nm

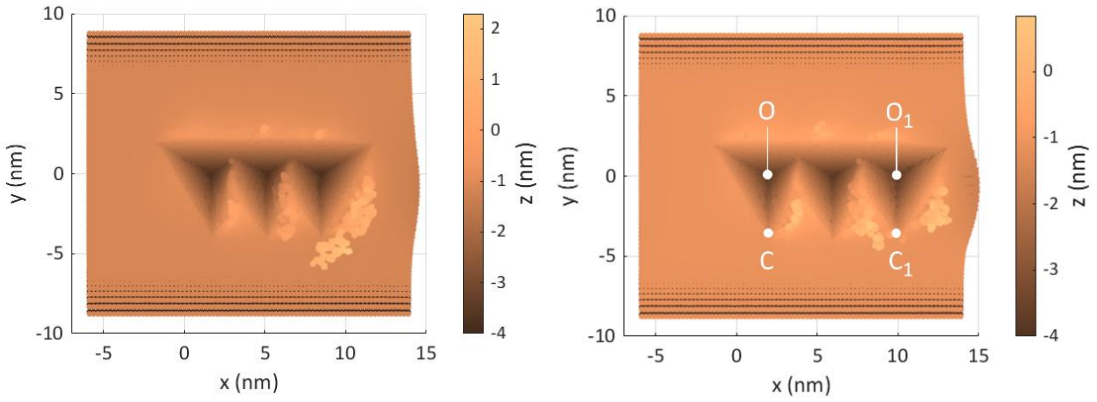

(g) T=3.4 nm (h) T=4.0 nm

Fig. 6.11. Top view of periodic nanostructures simulated with different periods (T) of dynamic ploughing.

Fourth, for the simulated surface with a period of 0.4 nm, the removed workpiece material remained on surface at the bottom of the nano-groove. This could affect the evaluation of the surface profile and surface roughness of the simulated nano-groove in later sections.

The quantitative characterisation of the simulated periodic 3D nanostructures is essential for fabricating complex 3D nanostructures with predictable and reliable dimensions. To achieve this, the simulated nanostructures were quantitatively described within a vertical cross sectional plane (as illustrated by the red transparent plane in Fig. 6.12 (a)), which has a y-axis co-ordinate of zero. More specifically, two planes were employed to extract a 3D cross section of the simulated nanostructure. It should be noted that this 3D cross section had a thickness of 0.5 nm along the y direction and contained two layers of SPH particles (as shown in Fig. 6.12 (b)).

Fig. 6.13 shows the 2D cross sections of the periodic 3D nanostructures on the vertical plane. Similar observations can be made as those seen in Fig. 6.11. In particular, 1) with a period of 0.4 nm, the simulated nano-grooves were similar to those obtained by nano-machining and no periodic nanostructures were formed, 2) with periods

larger than 1.0 nm, periodic nanostructures with triangular-shaped waveforms were obtained and the period of nanostructures was the same as that of the dynamic vibration, and 3) the triangular waveforms of nanostructures with periods larger than 1.0 nm were not isosceles but inclined slightly to the left side of the peaks. It should be noted that in the assessment of the profile waveform of the simulated nanostructures, the separated material on the left side of each peak was removed to improve the accuracy of the waveform profile. However, considering that it was not always easy to distinguish separated material from deformed material (see Fig. 6.13 (b)-(d)), inaccuracies could not be avoided when determining the position of the apex of the triangle waveform.

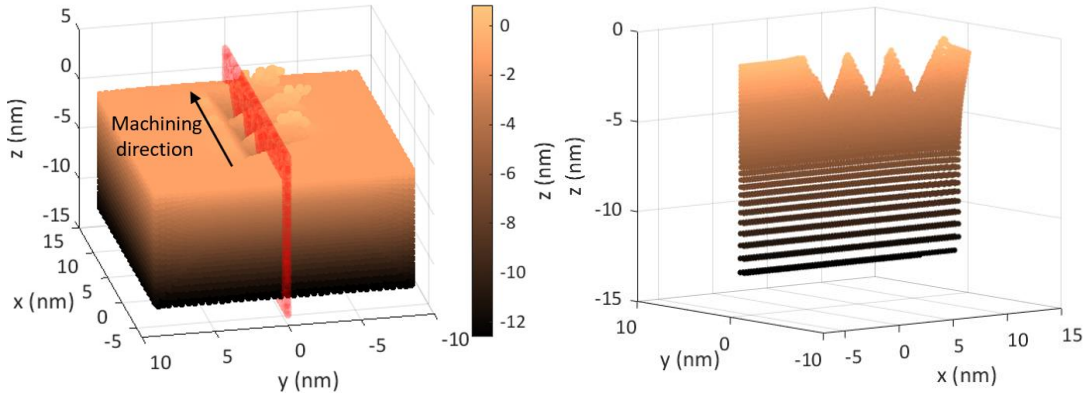

(a) (b)

Fig. 6.12. (a) The vertical cross sectional plane used to evaluate the profile waveform of the simulated nanostructures. (b) 3D view of the resulting periodic profile waveform.

Fig. 6.14 presents the height and depth of the triangular-shaped waveform nanostructures simulated with different periods of dynamic vibration. It should be noted that for each profile in Fig. 6.13, the height and depth here were evaluated in each successive “peak-valley” element and the resulting values were averaged to help reduce the error caused by the randomness of selecting a single “peak-valley” element. It can be seen that the depth of the triangular-shaped waveform nanostructures remains approximately constant about 2.7 nm, which is smaller than the ploughing

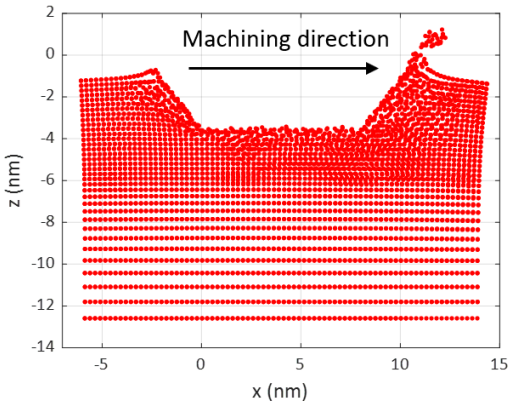

(a) T=0.4 nm

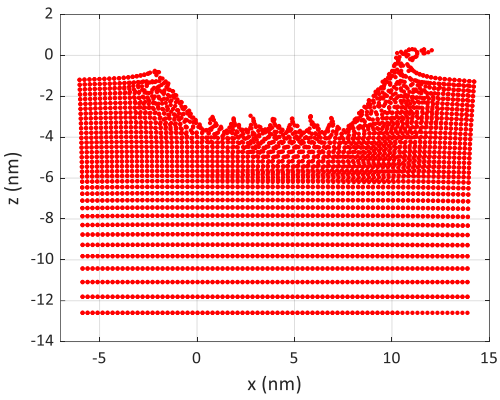

(b) T=1.0 nm

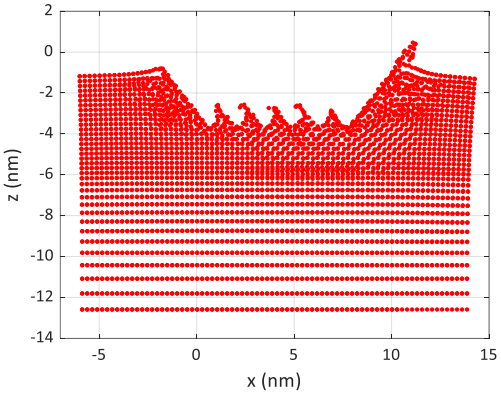

(c) T=1.4 nm

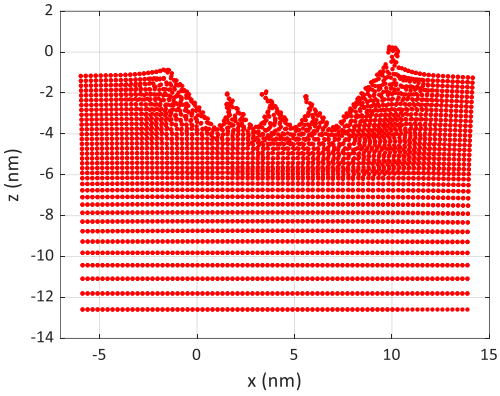

(d) T=2.0 nm

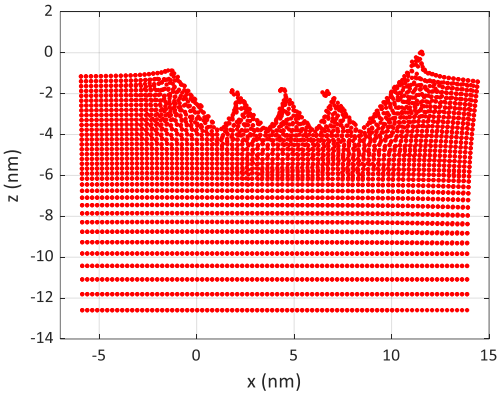

(e) T=2.4 nm

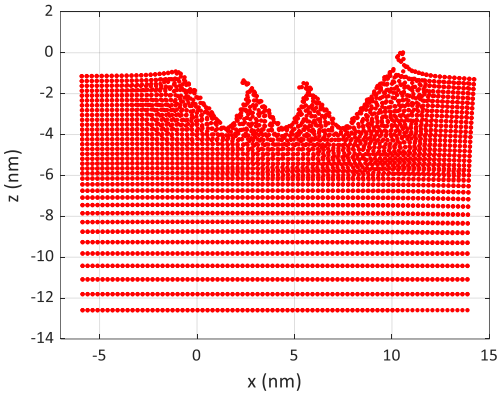

(f) T=3.0 nm

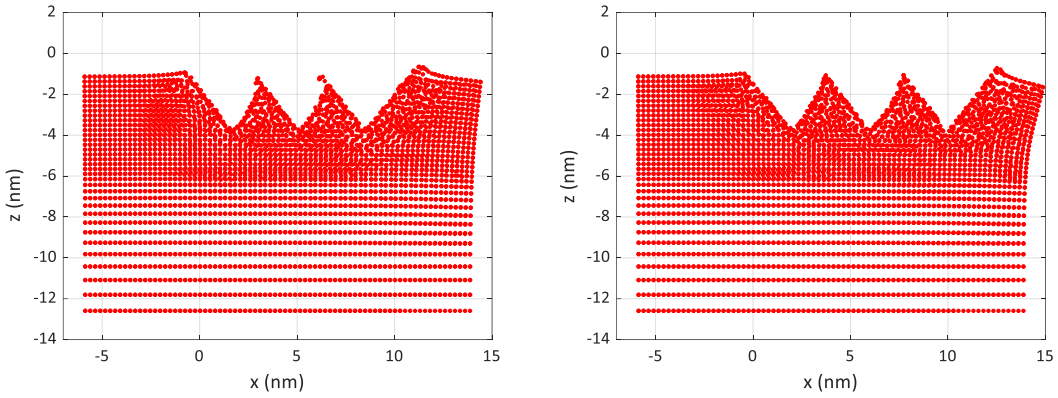

(g) T=3.4 nm (h) T=4.0 nm

Fig. 6.13. 2D view of the periodic profile waveforms using the vertical plane.

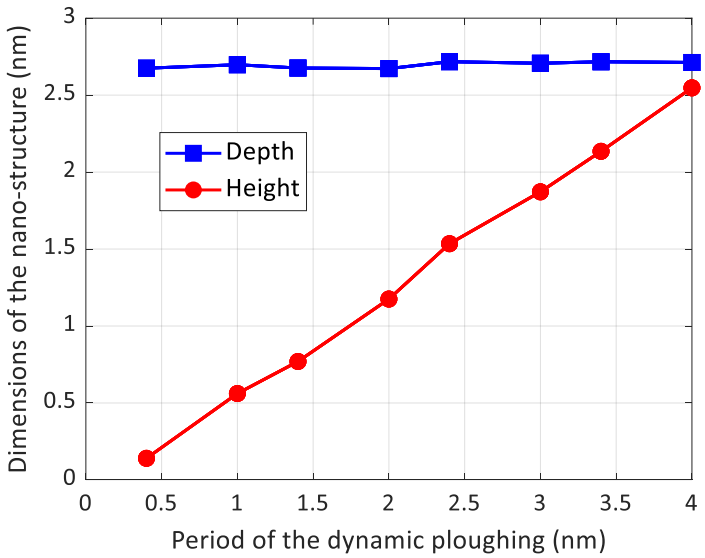

Fig. 6.14 Relationship between dimensions of the simulated nanostructures and the vibration period assessed on the vertical plane.

depth of 3 nm. The increase in the height of nanostructures is almost proportional to the increase in the period of dynamic ploughing. This observation indicates the possibility of employing AFM-based DPL for fabricating triangular-shaped waveform nanostructures with the desired combination of period and height.

For the rest of this section, the height and triangular profiles of the periodic nanostructures were also assessed within an inclined cross sectional plane (as illustrated by the blue transparent plane in Fig. 6.16 (a)), which is perpendicular to the edge of periodic nanostructures. This additional work is based on the following considerations. In biosensor and microfluidic chip scenarios, the triangular-shaped waveform nanostructures can be used to fabricate triangular-shaped nanowires. For example, as reported by Huang et al. (2013), magnetic zigzag nanowires were fabricated on triangular-shaped silicon trenches by electron beam lithography, electron beam evaporation, and lift-off processes. In this design, the stray field generated by the triangular shape of the magnetic nanowires can actively attract the magnetic cells for detection. Therefore, the locations of the peaks and valleys (i.e. the height and cross sectional profiles) of the triangular-shaped nanowires should play an important role in cell detection with this zigzag biosensor. In this context, the dimensions (i.e. height and triangular profiles) of the same periodic nanostructures were examined within different cross sections for the rest of this section, which could contribute to the fabrication of triangular-shaped nanowires with desired dimensions using electron beam lithography or other micro and nano-scale machining technologies. Particularly, the same periodic nanostructures were examined within an inclined plane which is perpendicular to the edge of periodic nanostructures.

It should be noted that the height of a simulated nanostructure assessed within the vertical plane is the maximum height (h_{max}) that can be obtained, and that the height assessed within an inclined plane which is perpendicular to the nanostructure edge is the minimum height (h_{min}). As illustrated in Fig. 6.15, these two values determined the range of the height of the triangular-shaped profile that a simulated periodic nanostructure had in different cross sections. The dashed lines in Fig. 6.15 represent the side face and edges of the simulated nanostructure.

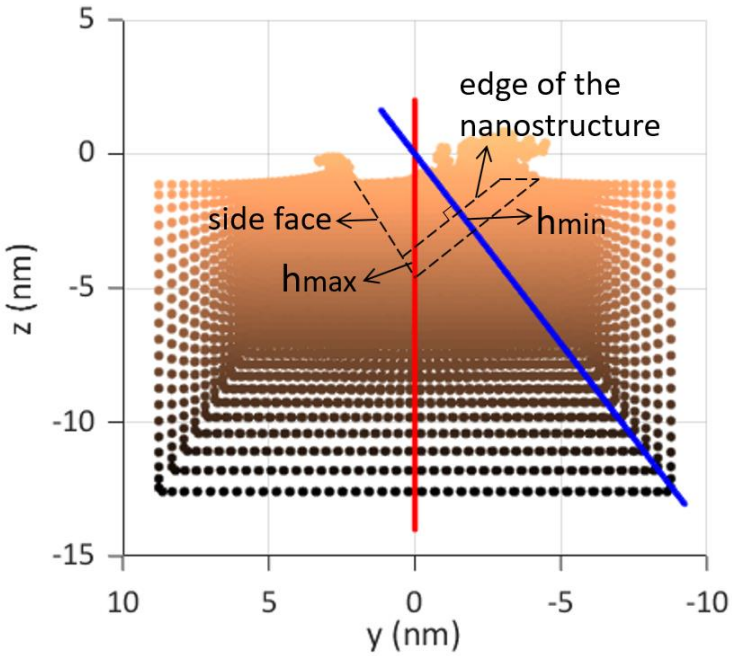

Fig. 6.15. Cross sectional planes to examine the triangular-shaped profile of the simulated nanostructure (the front view). The red plane represents the vertical cross sectional plane in Fig. 6.12 (a) and corresponds the maximum height of the nanostructure profile (h_{max}). The blue plane represents the cross sectional plane perpendicular to the nanostructure edge in Fig. 6.16 (a) and corresponds the minimum height of the nanostructure profile (hmin). h_{min} and h_{max} defined the range of the height of the triangular-shaped nanostructure in different cross sections. The dashed lines represent the side face and edges of the simulated nanostructure.

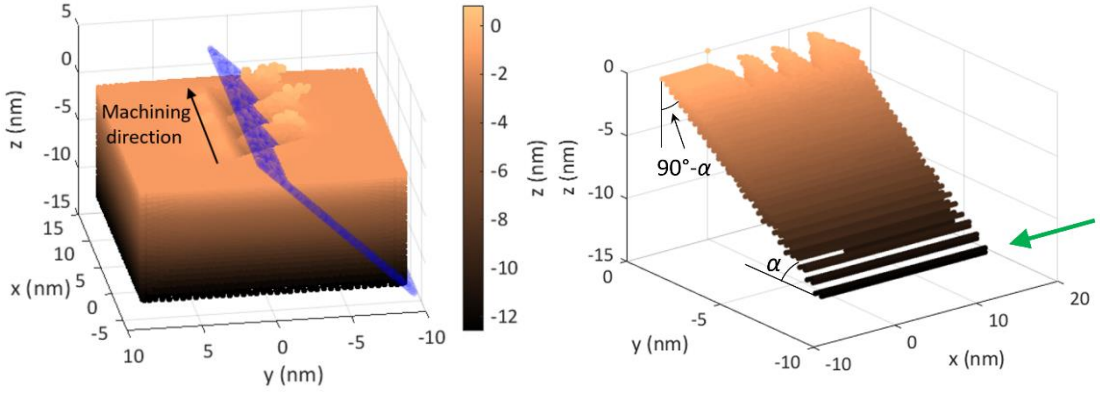

(a) (b)

Fig. 6.16. (a) The inclined cross sectional plane to evaluate the profile waveform of the simulated nanostructure. (b) 3D view of the resulting periodic profile waveform.

Fig. 6.16 (b) shows the 3D cross section of the simulated nanostructure extracted with two inclined planes. This 3D cross section had a thickness of 0.9 nm and contained three layers of SPH particles. In order to calculate the value of the minimum height (h_{min}) of the nanostructure displayed in Fig. 6.16 (b), the SPH particles in Fig. 6.16 (b) were rotated about the x-axis by an angle α until the 3D cross section was parallel to the xy plane. The coordinates of rotated SPH particles can be calculated by the following equation:

$$\begin{aligned} x' &= x \\ y' &= y\cos(-\alpha) - z\sin(-\alpha) \\ z' &= y\sin(-\alpha) + z\cos(-\alpha) \end{aligned} \tag{6.3}$$

where (x, y, z) and (x', y', z') are the original and transformed coordinates of SPH particles, respectively. α is the rotation angle about the x-axis which can be calculated as α = 90°-arctan(3.29/4.65) = 54.72°. This was obtained by calculating the vector OC = (0, -4.65, 3.29) in Fig. 6.2. -α indicates the clockwise rotation when looking in the direction of the negative x-axis (see the green arrow in Fig. 6.16 (b)).

Fig. 6.17 shows the 2D cross sections of the periodic 3D nanostructures evaluated on the inclined cross sectional plane. Several observations are noted in Fig. 6.17. First, irregular patterns were observed at the bottom of the simulated nano-groove when T=0.4 nm and 1.0 nm in Fig. 6.17 (a)-(b), which was not the case for the profiles when T=0.4 nm and 1.0 nm in Fig. 6.13 (a)-(b). The possible reason could be the occurrence of material accumulation at the bottom of the nano-groove during the DPL process. In particular, it can be seen from Fig. 6.11 (a) that the removed material mainly remained on the inclined side surface of the nano-groove, and that a small amount of removed material accumulated near the lowest valley of the nano-groove. As a result, irregular patterns were observed on the cross-sectional profile within the inclined cross sectional plane, but not on the profile within the vertical plane. These irregular patterns also made it difficult to accurately determine the profiles of the 2D cross sections in Fig. 6.17 (a)-(b). Second, for periods larger than 1.0 nm, such a

phenomenon of material accumulation on the surface of the nano-grooves was not apparent, and the workpiece material around the profile peaks shifted slightly to the left side of each peak, resulting in the inclination of the peaks of the periodic nanostructures. Third, the profiles in Fig. 6.17 were much more straight and smoother than those in Fig. 6.13. This observation still existed when decreasing the thickness of the 3D cross section in Fig. 6.16 to 0.5 nm. The discrepancies in the profiles in Fig. 6.13 and Fig. 6.17 could be investigated in future work.

Figure 6.18 shows the influence of the period on the minimum height (hmin) of simulated nanostructures assessed on the inclined cross sectional plane. The maximum height (hmax) of simulated nanostructures assessed on the vertical plane in Fig. 6.14 was also superimposed here. It can be seen that for a period smaller than 1.5 nm, hmin and hmax evaluated on two planes were almost the same. For a period larger than 1.5 nm, hmin was slightly smaller than hmax. This is consistent with the fact that the profiles of nanostructures within the vertical intersection plane have a larger area of triangular waveforms. The theoretical relationship between hmax and hmin can be expressed mathematically as $hmin = hmax \cdot \cos(90°-\alpha) = 0.816 \cdot hmax$ (see Fig. 6.12 (b) and Fig. 6.16 (b)). However, from simulation results in Fig. 6.18, hmin was closer to hmax probably due to the error in determining the evaluated profiles of nanostructures on cross sectional planes.

Overall, Fig. 6.18 indicates the possibility of employing AFM-based DPL for fabricating triangular-shaped waveform nanostructures with desired and specified heights ranging from hmin to hmax. As mentioned before, this could contribute to the fabrication of triangular-shaped biosensor nanowires with desired heights using electron beam lithography or other micro and nano-scale machining technologies.

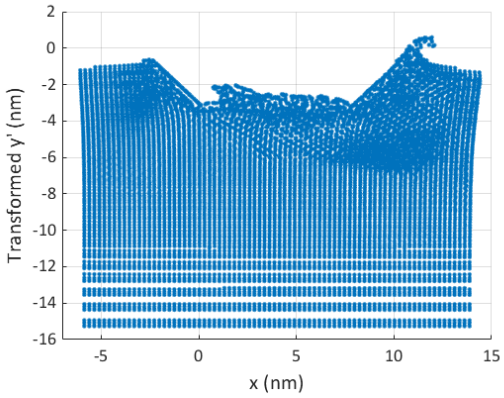

(a) T=0.4 nm

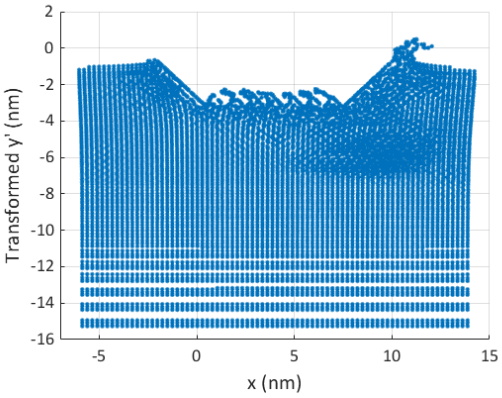

(b) T=1.0 nm

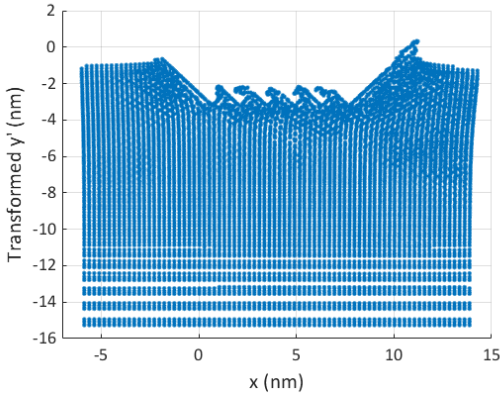

(c) T=1.4 nm

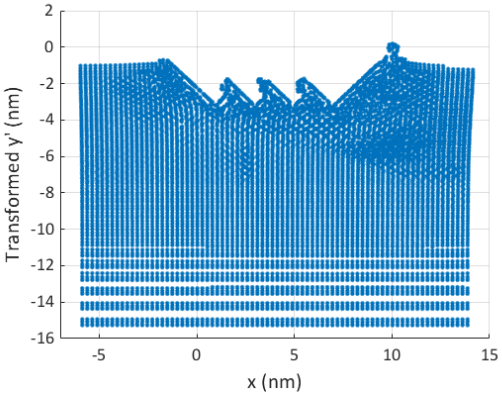

(d) T=2.0 nm

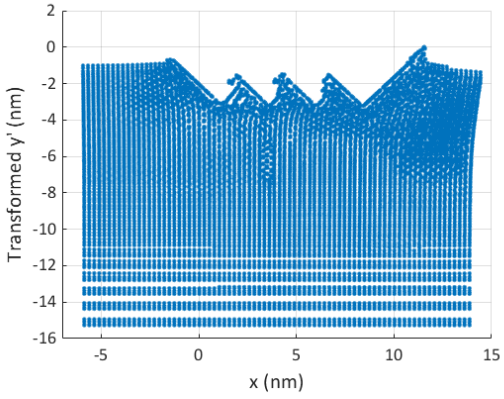

(e) T=2.4 nm

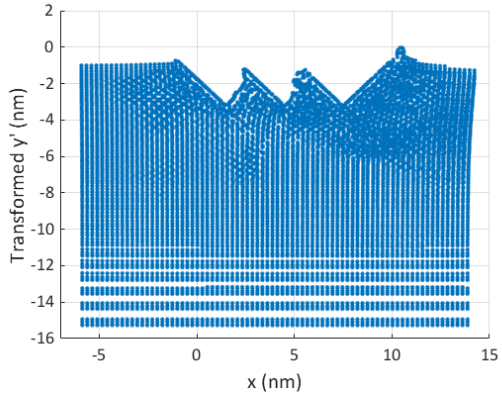

(f) T=3.0 nm

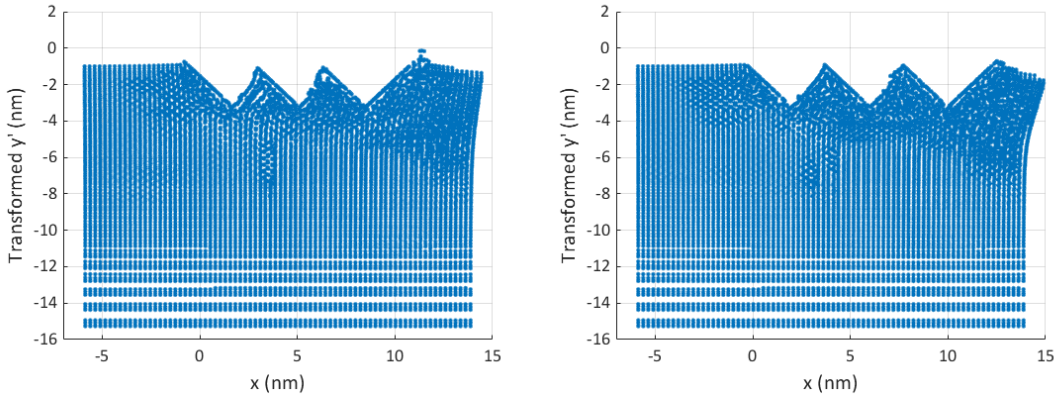

(g) T=3.4 nm (h) T=4.0 nm

Fig. 6.17. 2D view of the periodic profile waveforms using the inclined cross sectional plane.

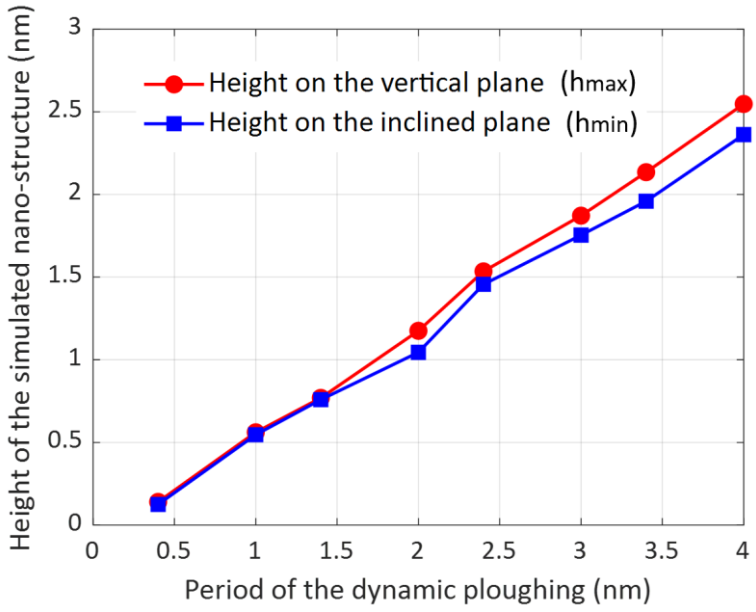

Fig. 6.18. Influence of the period on the minimum height (h_{min}) of simulated nanostructures assessed on the inclined cross sectional plane. The maximum height (h_{max}) of simulated nanostructures assessed on the vertical plane in Fig. 6.14 was also superimposed here.

6.5 Generated surface roughness

Surface quality can affect the performance and functional characteristics of nano-grooves, and thus it is essential to evaluate the surface topography resulting from micro and nano-scale mechanical machining. Among the surface profile parameters defined to measure the surface quality, the arithmetical mean deviation of the roughness profile *Ra* is probably the most commonly used parameter. Such roughness profile is normally obtained by discarding the long wavelength component (which corresponds to the waviness profile) and very short wavelength component (Leach, 2001). Fig. 6.19 illustrates how to determine the arithmetical mean deviation of roughness profile *Ra*. A mean line is first defined in such a way that its z-axis co-ordinate equals the average of the co-ordinate values $Z(x)$. Then the *Ra* value is calculated as the mean deviation of the ordinate values Z_n from the mean line. This is expressed mathematically with:

$$R_a = \frac{|Z_1| + |Z_2| \cdots + |Z_n|}{n} \tag{6.4}$$

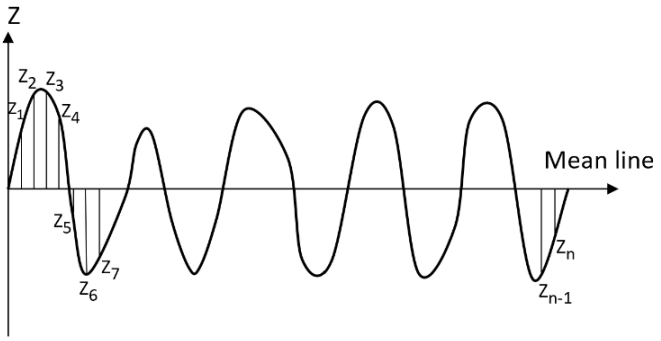

Fig. 6.19. Determination of the arithmetical mean deviation *Ra* of roughness profile.

Fig. 6.20 presents the roughness profile of the simulated nano-groove with a period of 0.2 nm. The sampling length for the roughness profile was equal to the dynamic ploughing distance of 8 nm. It should be noted that the assessed roughness profile was extracted using the vertical cross sectional plane instead of the inclined plane for

two reasons. First, it was found in the previous section that the difference in dimensions of the simulated nanostructures evaluated from these two planes was not significant. Second, unusual conditions were not likely to be observed on the roughness profile (see Fig. 6.13) extracted using the vertical plane, such as burrs on the left side of periodic edges and material accumulation on the surface at the bottom of the nano-groove. This could help obtain more accurate roughness profiles and *Ra* values. The mean line was determined by averaging the z-axis co-ordinates of discrete points on the roughness profile. The roughness value *Ra* could then be calculated using equation (6.3) with Matlab.

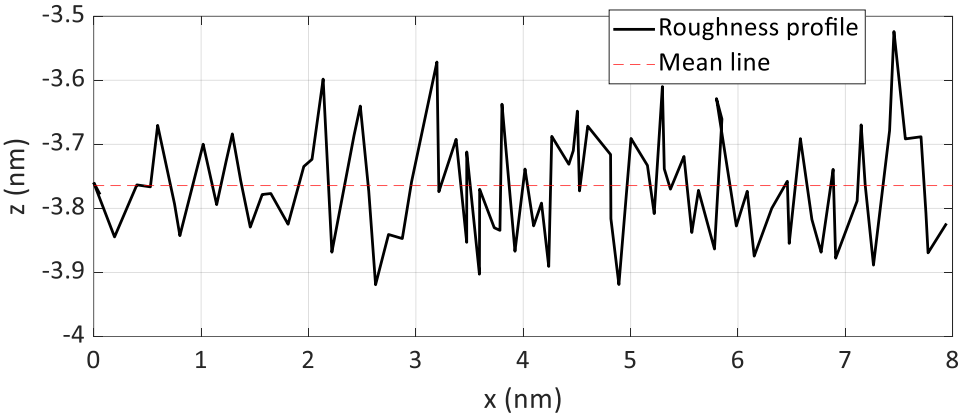

Fig. 6.20. Roughness profile of the nano-groove simulated with T=0.2 nm.

It was seen earlier from Fig. 6.11 that when the period T is larger than 1.0 nm, nanostructures exhibited clearly visible repetitiveness and thus a waviness profile was present. Therefore, the surface roughness was investigated here only for periods smaller than 1.0 nm due to the resolution of the available simulated data points. As shown in Fig. 6.21 and Fig. 6.22, 10 sets of SPH simulations of DPL were performed with period values ranging from 0.1 nm to 1.0 nm, at intervals of 0.1 nm. Several observations are made from Fig. 6.21 and Fig. 6.22. First, even with periods smaller than 1.0 nm, the simulated surfaces at the bottom of nano-grooves still showed some degree of repetitiveness. These periodic features repeated at a distance equal to the value of the period. Second, the overall height of the pileup at the end of the machined

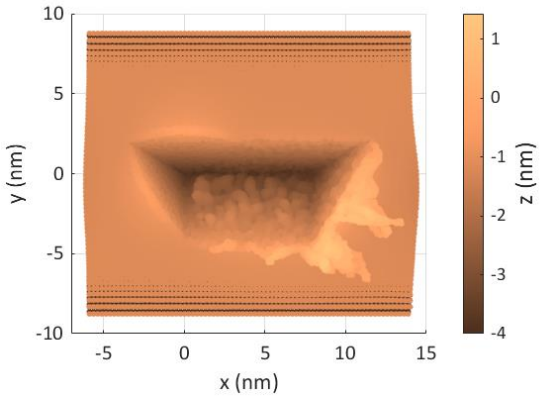

(a) T=0.1 nm

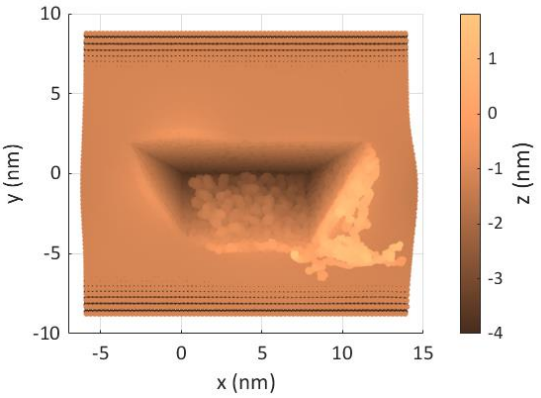

(b) T=0.2 nm

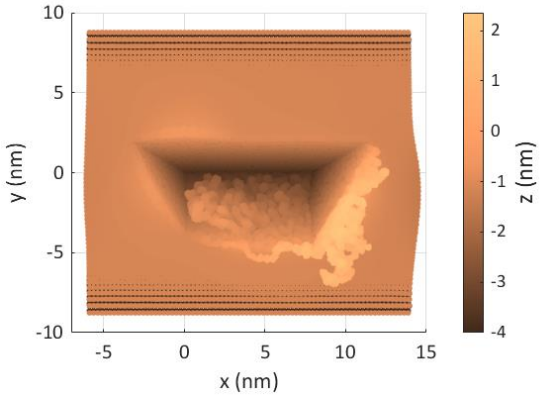

(c) T=0.3 nm

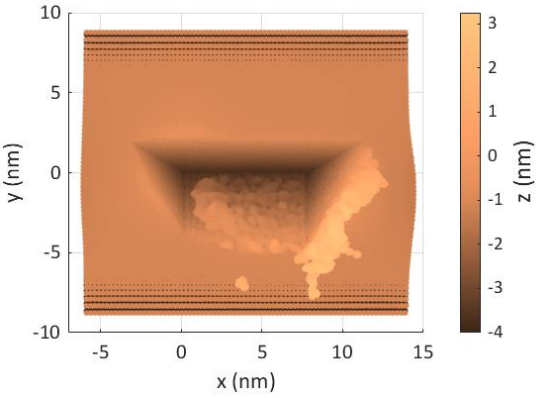

(d) T=0.4 nm

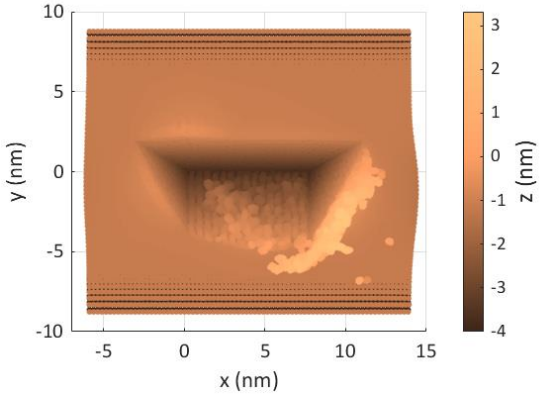

(e) T=0.5 nm

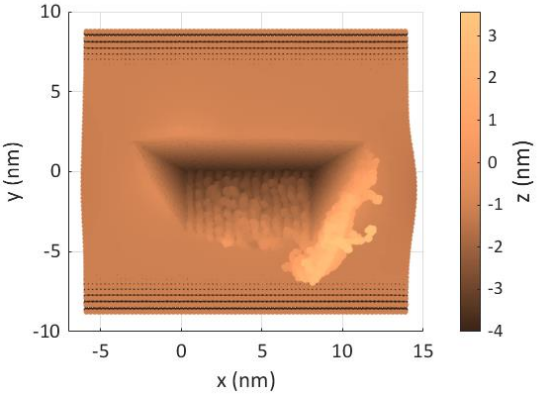

(f) T=0.6 nm

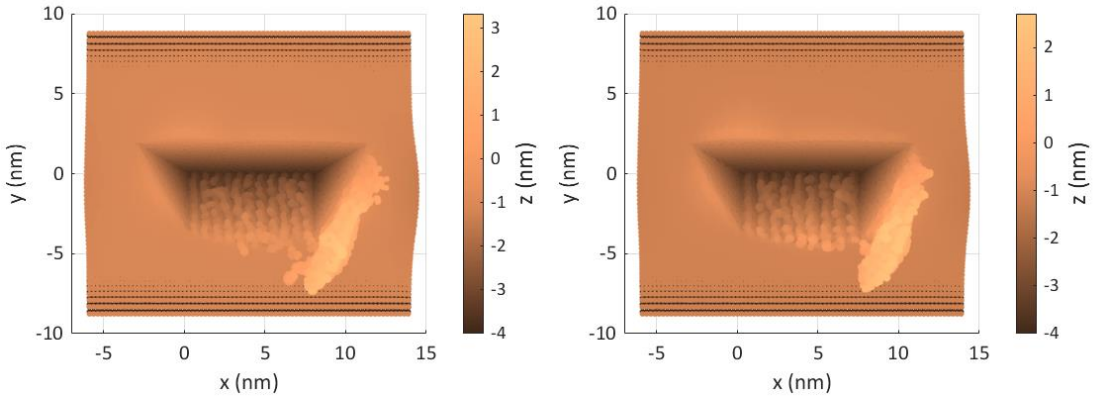

(g) T=0.7 nm (h) T=0.8 nm

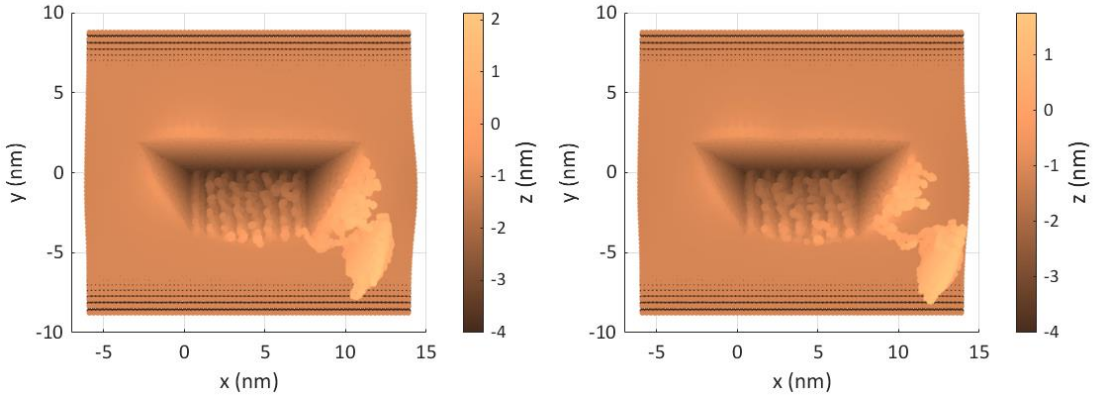

(i) T=0.9 nm (j) T=1.0 nm

Fig. 6.21. Top view of nano-grooves simulated with periods smaller than 1.0 nm.

surface in Fig. 6.21 was larger than that in Fig. 6.11. As discussed in Section 6.4.2, one possible reason is likely due to the larger volume of material removed by dynamic ploughing when using a small period of vibration. Third, the removed workpiece material remained on the bottom of nano-grooves with periods smaller than 0.5 nm, but this problem was not observed for nearly all of the roughness profiles in Fig. 6.13 probably due to the employment of the vertical plane.

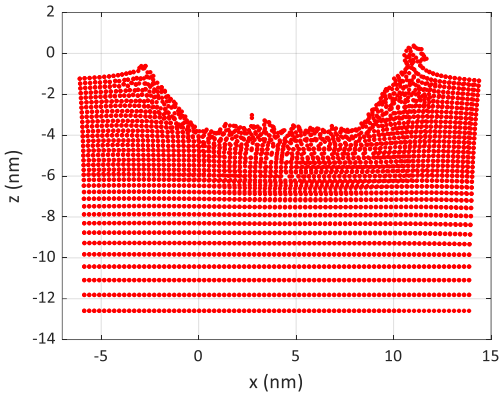

(a) T=0.1 nm

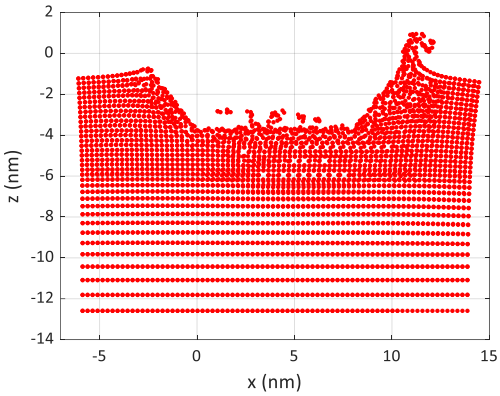

(b) T=0.2 nm

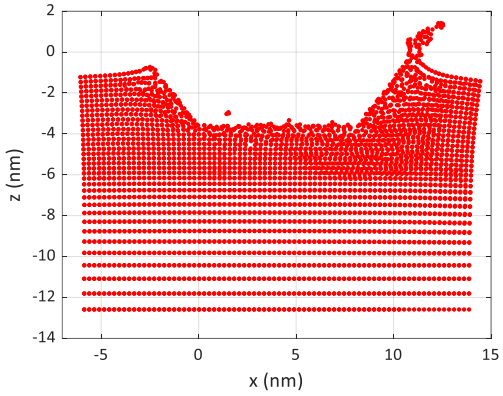

(c) T=0.3 nm

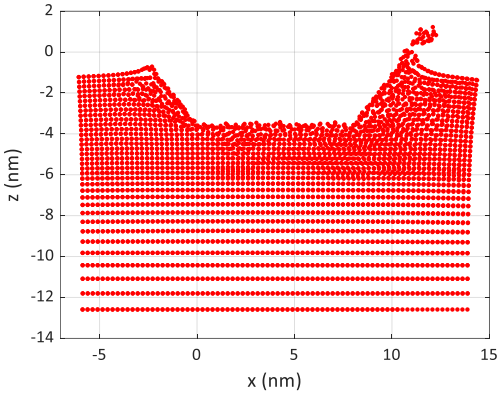

(d) T=0.4 nm

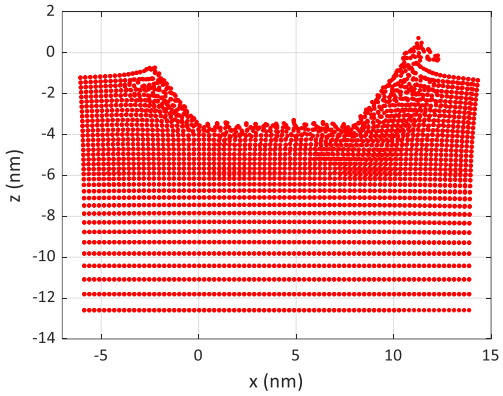

(e) T=0.5 nm

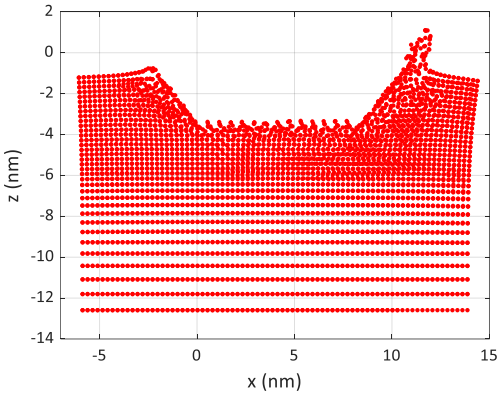

(f) T=0.6 nm

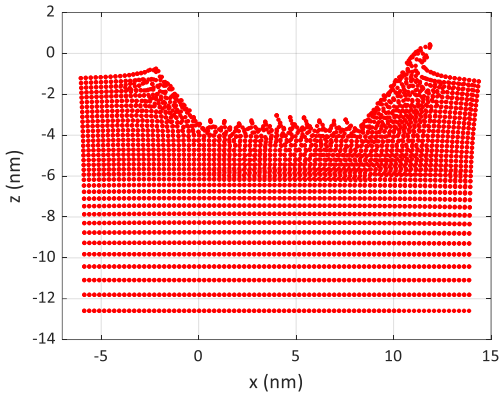

(g) T=0.7 nm

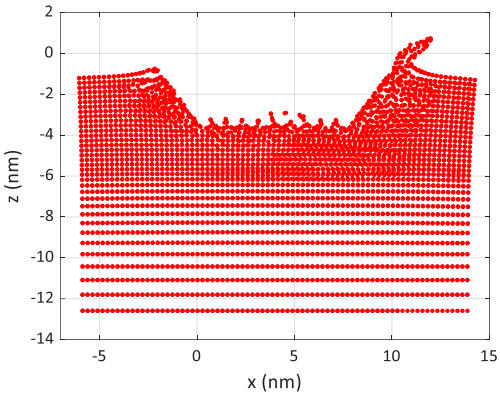

(h) T=0.8 nm

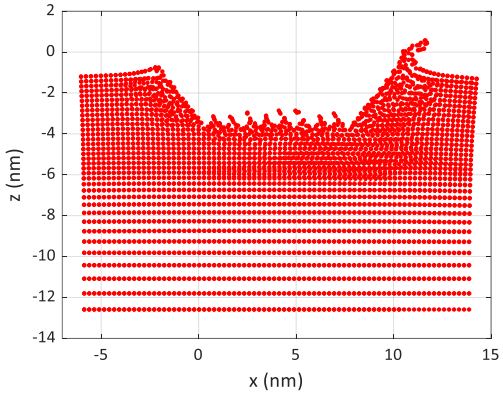

(i) T=0.9 nm

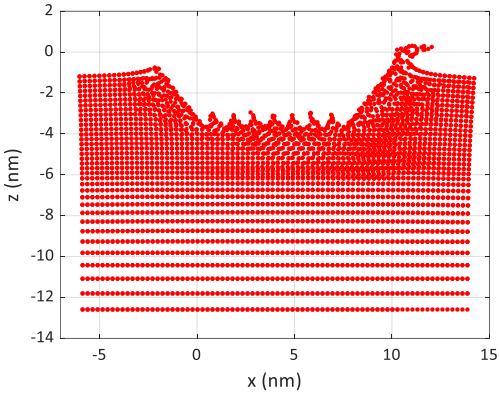

(j) T=1.0 nm

Fig. 6.22. 2D view of roughness profiles of nano-grooves obtained using the vertical plane

Fig. 6.23 shows the roughness values *Ra* calculated from the roughness profiles in Fig. 6.22. It can be seen that the *Ra* value showed an increasing trend with the increasing period of dynamic ploughing, which is generally consistent with the appearances of the roughness profiles in Fig. 6.22. It should be noted however the *Ra* value for the period of 0.1 nm does not match this trend as it was relatively large. This is likely to be caused by the error in the determination of the roughness profile from Fig. 6.22 (a). More specifically, considering the remaining material on the bottom of the nano-groove in Fig. 6.21 (a), it was not easy to decide which points in Fig. 6.22 (a) should be counted as the points on the roughness profile. For this reason, large errors and

inaccuracies were introduced when determining the roughness profile and the roughness value *R*a with the period of 0.1 nm. However, the removed material and deformed material can be distinguished relatively easily with the period of 0.2 nm, as illustrated in Fig. 6.22 (b). This could reduce the errors in the determination of the roughness profile compared with the case with the period of 0.1 nm for this set of simulations.

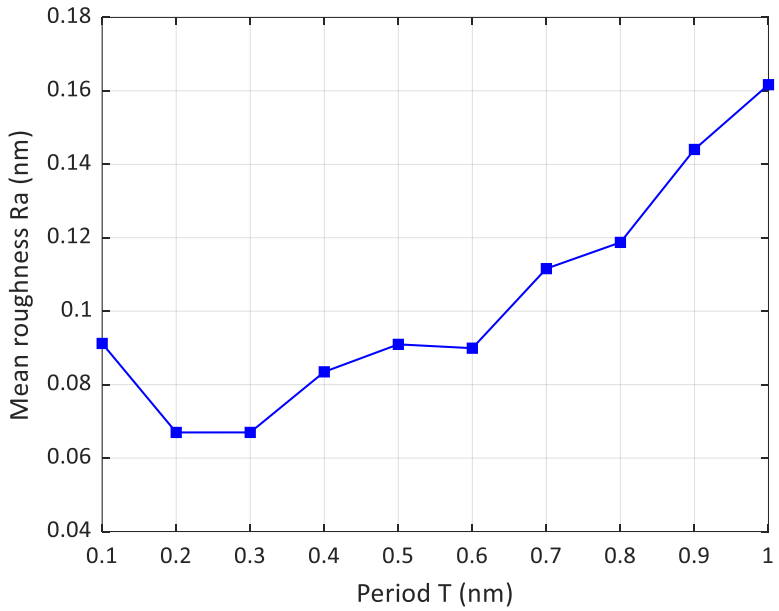

Fig. 6.23. Influence of the vibration period on the surface roughness of simulated nano-grooves.

6.6 Concluding remarks

This chapter aimed to address the third knowledge gap identified in this research, which is concerned with the feasibility of employing SPH modelling to simulate the AFM probe-based dynamic ploughing lithography process. The following conclusions were drawn from the work conducted in this chapter.

- Quantitative comparisons showed apparent discrepancies between the SPH-predicted results obtained here and the MD-predicted results presented by

Xiao et al. (2019). In particular, the averaged value of the SPH-predicted resultant force was 6.17 times larger than that of the MD-predicted resultant force. In addition, the depth of the nano-groove simulated by SPH was 2.7 nm, larger than that obtained by MD in (Xiao et al., 2019) (i.e. 1.7 nm). These discrepancies between SPH-predicted and MD-predicted results should be further investigated in order to potentially improve the predictability and reliability of the implemented SPH model of AFM-based DPL. For this reason, subsequent attempts made to simulate the AFM-based DPL process using the SPH method in this chapter were mainly qualitative.

- When the period of dynamic ploughing lithography exceeded 1.0 nm, a nanostructure that repeated at a given spatial frequency was clearly visible to generate a periodic surface. The period of this nanostructure was equal to that of the simulated DPL process. The periodic nanostructure can be regarded as a series of successive “nano-bundles” placed on the side surface at the bottom of the simulated nano-groove. This indicates the possibility of fabricating 3D periodic nanostructures with the aid of AFM-based dynamic ploughing lithography.

- When the period of dynamic ploughing lithography exceeded 1.0 nm, the simulated periodic nanostructure had a triangular-shaped profile waveform. This waveform did not consist of isosceles triangles as these were inclined slightly to the left side of each peak. This triangular-shaped profile waveform was assessed using two different viewing directions. The first view direction was perpendicular to a vertical cross sectional plane. The second view direction was parallel to the edges of the periodic nanostructure, which was the direction of the predominant surface pattern. It was found that the appearance of the profile was not significantly affected by the viewing directions, but the height of the triangular profile waveform evaluated with

the inclined cross section plane was smaller than that obtained with the vertical plane. Overall, the observations made theoretically confirm the possibility of employing AFM-based DPL for fabricating triangular-shaped waveform nanostructures with the desired combination of period and height. In addition, the desired height could be selected within a specified range from h_{min} to h_{max} where h_{min} and h_{max} refer to the height of the nanostructure evaluated on the inclined cross sectional plane and that on the vertical plane, respectively.

- When the period of dynamic ploughing lithography was smaller than 1.0 nm, the bottom of the simulated nano-groove still showed some degree of repetitiveness but these repetitive features were relatively small. The roughness profile and corresponding roughness *Ra* value were evaluated for each period of simulated. The *Ra* value showed an increasing trend with the increasing DPL period. This observation was generally consistent with the qualitative appearances of the corresponding roughness profiles.

In summary, the study conducted in this chapter can be seen as a first attempt to simulate the AFM probe-based DPL process using the SPH method. Although the suitability of applying the implemented SPH model to quantitatively simulate the AFM probe-based DPL needs to be further investigated, the qualitative investigations in this chapter may still shed light on the possibility of employing AFM-based DPL for (1) fabricating triangular-shaped waveform nanostructures with desired period and height and (2) fabricating periodic nanostructures with desired profile waveforms (such as a sine wave) and desired dimensions by combining different tool trajectories and (horizontal) machining directions.

Chapter 7 Conclusions, contributions and future work

7.1 Conclusions

The conclusions from this Thesis are drawn and summarised as follows.

The implemented SPH model of nano-indentation can be used to predict the resultant force and investigate the influence of simulation conditions on material response during nano-indentation in the following aspects: (1) the initial validation examination of the implemented SPH model of nano-indentation, (2) the benchmark study in the context of micro-indentation and (3) the investigation of the influence of indenter tip on material responses. The SPH-predicted resultant force was noted to be larger when using a blunt tip indenter than when using a sharp indenter. In addition, the load-displacement curve simulated with the implemented SPH model of nano-indentation was generally closer to the experimental results compared to the FEM-generated data reported in literature.

In the SPH simulations of nano-machining on copper, the simulated forces and the cross-sectional profile of simulated nano-groove using the Johnson-Cook constitutive model were closer to experimental results compared to that obtained when implementing the elasto-plastic model. Thus, the selection of the Johnson-Cook model is preferable for the SPH modelling of the nano-machining process. In addition, the implemented SPH model could be used as a suitable first approximation to predict the cutting and normal forces during nano-machining, considering that the discrepancies in the actual values obtained between the simulated and experimental results are within the same order or magnitude.

The SPH-predicted surface topography of AFM-based DPL showed that 3D periodic nanostructures were clearly visible with a relatively large vibration period. In addition, the period of the generated nanostructure was subject to the period of dynamic ploughing and the height of the generated nanostructure was slightly different in different viewing directions. This observation is significant because it sheds light on the possibility of employing AFM-based DPL for fabricating 3D periodic nanostructures with triangular-shaped or sinusoidal profile waveforms. In addition, the dimensions (i.e. the height and period) of these nanostructures with triangular-shaped or sinusoidal profile waveforms could be controllable by adjusting the vibration period, the shape of the nano-indenter and the machining direction during AFM-based DPL.

7.2 Contributions

The main contributions associated with the identified research gaps are summarised.

Research gap 1: Investigation of the feasibility of employing SPH modelling for simulating the nano-indentation process.

Contributions:

1. An SPH model of nano-indentation reported in existing literature was reproduced. The complementary work produced in this research in comparison with the published SPH model consisted in the indentation speed, the implementation of the stress-strain relationship in LS-DYNA, detailed modelling procedures and a convergence study to determine the optimal particle density.
2. An additional benchmark study in the context of micro-indentation was modelled to further establish and refine the accuracy of the implemented SPH model of nano-indentation. This was realised by comparing the SPH-predicted force-displacement responses with the FEM-predicted and experimental outcomes reported in existing literature.

3. The implemented SPH model of nano-indentation was employed to investigate the influence of the shape of the nano-indenter tip on material responses

Research gap 2: Comparison of the influence of adopted material models on the material response during micro and nano-scale machining, with a specific focus on the predicted surface profile of machined grooves.

Contributions:

1. An SPH model of nano-machining of copper with two different material models, namely the Johnson-Cook and the elasto-plastic models, was implemented.
2. The effect of these two material models on the simulation results was analysed from the following aspects: (1) simulated cutting and normal forces with different cutting depths, (2) the effect of the cutting speed on simulated forces and (3) the surface topography of machined nano-scale groove.

Research gap 3: Investigation of the feasibility of employing SPH modelling to simulate the AFM probe-based dynamic ploughing lithography (DPL) process.

Contributions:

1. Based on the implemented SPH models of nano-indentation and nano-machining, the work reported in Chapter 6 can be seen as an original attempt to simulate the AFM probe-based DPL process using the SPH method.
2. The developed SPH model of AFM probe-based DPL was evaluated by comparing SPH-predicted results with MD results published in the literature from the perspectives of (1) quantitative comparison of the forces during dynamic ploughing and (2) qualitative comparison of the simulated surface topography.
3. The SPH-predicted surface topographies of AFM probe-based DPL were comprehensively investigated from the following aspects: (1) the presence of some machining phenomena such as pile-ups, material accumulation and periodic nano-scale patterns, (2) the influence of the vibration amplitude on dimensions of

the simulated nano-grooves, (3) the influence of the vibration period on the topographies and dimensions of generated periodic nanostructures and (4) the evaluation of the waveform profile of generated periodic nanostructures from two different viewing directions.

4. The roughness profiles and roughness values of the simulated nano-grooves were assessed for different periods of dynamic ploughing.

7.3 Uncertainty analysis for model predictions using SPH

In Chapter 4, the uncertainty in model predictions and sensitivity to process parameters were evident in three key aspects during the validation examination of the implemented SPH model of nano-indentation. First, discrepancies in the maximum Von Mises stress, with percentage differences up to 16.85% at small indentation depths, highlighted the model's sensitivity to the initial gap between the indenter tip and workpiece. This sensitivity demonstrated the need for precise definition of SPH model boundaries established in ANSYS/LS-DYNA. Second, the force predictions of the implemented SPH model within the context of micro-indentation exhibited sensitivity to unloading speeds, with obvious discrepancies observed in unloading curves at varying speeds. The material model, derived from uniaxial compression tests, may not accurately represent material behavior in tensile processes, affecting the model's accuracy during micro-indentation. This illustrated the need for material models that account for different loading and unloading conditions to enhance the reliability of SPH predictions. Third, the high indentation speed of 100 m/s, while necessary for reducing computational time, may have affected the accuracy of the unloading response, suggesting a potential area for further investigation to refine model predictions.

Chapter 5 explored the influence of constitutive material models on the simulated cutting and normal forces, as well as the machined topography during nano-machining.

In the analysis comparing the Johnson-Cook and elasto-plastic models, it was evident that the Johnson-Cook model provided results closer to experimental data in existing literature, suggesting a higher sensitivity of the SPH model predictions to the selected material model. The simulated cutting and normal forces were found to be smaller than experimental results in existing literature, possibly due to the absence of contact friction and the lateral size effect in the SPH model. This discrepancy highlighted the uncertainty in force predictions without considering these factors, thereby emphasizing the need for model refinement to include these factors. In addition, the influence of the cutting speed on simulated forces was only observed with the Johnson-Cook model, which indicated a model-specific sensitivity to process parameters.

In Chapter 6, the uncertainty in model predictions was pronounced in the comparison between SPH-predicted and MD-predicted forces (in existing literature) during AFM-based DPL. The SPH model overestimated the resultant force by a factor of 6.17 compared to MD predictions, suggesting a significant uncertainty in the force prediction. The depth of the SPH-predicted nano-groove (2.7 nm) was larger than that obtained by MD (1.7 nm), further indicating the model's sensitivity to the choice of numerical method and employed parameters. The vibration amplitude and vibration period during AFM probe-based DPL were identified as critical parameters influencing the dimensions and profile of simulated nano-grooves. The increase in roughness value (*R*a) with the increasing DPL period revealed the model's sensitivity to the process parameter of the period, affecting the surface quality of the simulated periodic nanostructures. These findings demonstrate the need for a comprehensive investigation into the reasons behind the discrepancies between SPH and MD predictions to enhance the reliability of the SPH model in predicting the outcomes of the AFM-based DPL process.

7.4 Recommendations for future work

The recommendations for future work are summarised as follows.

Improving the reliability of unloading responses of the SPH model for nano-indentation: The implemented SPH model of nano-indentation exhibited slightly varying behaviour of the unloading response at different unloading speeds. As discussed in Chapter 4, the influence of crack or fracture inside the workpiece should not be accounted for this observation. Therefore, further investigations should be conducted on the influence of loading/unloading speed on unloading response.

Enhancing the SPH model for nano-machining through the incorporation of contact friction and size effects: In the implemented SPH model of nano-machining, the contact friction and lateral size effect were not taken into account. In order to improve the accuracy of the SPH-predicted forces, one possible avenue of further research is to introduce the contact friction and lateral size effect to the SPH model of nano-machining.

Manufacturing diverse 3D periodic nanostructures with predictable profile waveforms through investigating simulation conditions in AFM-based DPL: The reason for the discrepancies between the SPH-predicted and MD-predicted forces and groove depth should be further investigated in order to potentially improve the predictability and reliability of the implemented SPH model of AFM-based DPL. This could be related to the adopted material models between these two numerical methods. Besides, since a simplified tool trajectory of a triangular wave, instead of a sinusoidal tool trajectory, was used in this Chapter to simulate the dynamic motion of the AFM probe, further investigations should be conducted on simulating the AFM-based DPL using a sinusoidal tool trajectory. Finally, the influence of simulation conditions (i.e. the vibration period, the vibration amplitude, tool trajectory, shape of the nano-indenter and the machining direction) on the AFM-based DPL process should

be systematically investigated, with an objective of fabricating 3D periodic nanostructures with desired and controllable profile waveforms (such as a sine wave).

References

Anand, R., & Patra, K., 2014, Modeling and simulation of mechanical micro-machining—A review. Machining Science and Technology, 18(3), 323-347.

Aurich, J., Engmann, J., & Schueler, G., 2009, Micro grinding tool for manufacture of complex structures in brittle materials. CIRP Annals - Manufacturing Technology, 58(1), 311–314.

Benz, W., and Asphaug, E., 1995, Simulations of brittle solids using smooth particle hydrodynamics. Computer Physics Communications, 87(1), 253-265.

Binnig, G., Quate, C., & Gerber, C., 1986, Atomic force microscope. Physical review letters, 56(9), 930.

Bonet, J., and Kulasegaram, S., 2000, Correction and stabilization of smooth particle hydrodynamics methods with applications in metal forming simulations. International Journal for Numerical Methods in Engineering, 47(6), 1189-1214.

Cai, M., Li, X., & Rahman, M., 2007, Study of the mechanism of nanoscale ductile mode cutting of silicon using molecular dynamics simulation. International Journal of Machine Tools and Manufacture, 47(1), 75-80.

Calamaz, M., Limido, J., Nouari, M., Espinosa, C., Coupard, D., Salaün, M., & Chieragatti, R., 2009, Toward a better understanding of tool wear effect through a comparison between experiments and SPH numerical modelling of machining hard materials. International journal of refractory metals and hard materials, 27(3), 595-604.

Câmara M., Rubio J., & Abrão A., 2012, State of the art on micromilling of materials, a review. Journal of Materials Science and Technology, 28(8): 673–685.

Cao, J., Wu, Y., Li, J., & Zhang, Q., 2016, Study on the material removal process in ultrasonic-assisted grinding of SiC ceramics using smooth particle hydrodynamic (SPH) method. The International Journal of Advanced Manufacturing Technology, 83, 985-994.

Chang, H., Fivel, M., Rodney, D., & Verdier, M., 2010, Multiscale modelling of indentation in FCC metals: from atomic to continuum. C R Phys 11(3–4):285–292.

Chang, T., Hong, K., & Lai, Y., 2016, ZnO-based microcavities sculpted by focus ion beam milling. Nanoscale Research Letters, 11(1): 319–325.

Cheng, K., Luo, X., Ward, R., & Holt, R., 2003, Modeling and simulation of the tool wear in nanometric cutting. Wear, 255(7-12), 1427-1432.

Cheng, K., and Huo, D., 2013, Micro cutting: fundamentals and applications. John Wiley & Sons, Chichester.

Cheung, C., and Lee, W., 2000, Modelling and Simulation of Surface Topography in Ultra-Precision Diamond Turning, Proceedings of the Institution of Mechanical Engineers, Part B: Journal of Engineering Manufacture, 214(6), 463-480.

Chuzhoy, L., DeVor, R., & Kapoor, S., 2003, Machining simulation of ductile iron and its constituents, Part 2: Numerical Simulation and Experimental Validation of Machining. Journal of Manufacturing Science and Engineering, 125(2), 192-201.

Chuzhoy, L., DeVor, R., Kapoor, S., & Bammann, D., 2002, Microstructure-level modelling of ductile iron machining. Journal of Manufacturing Science and Engineering, 124(2), 162-169.

Dao, M., Chollacoop, N., Van Vliet, K., Venkatesh, T., & Suresh, S., 2001, Computational modeling of the forward and reverse problems in instrumented sharp indentation. Acta Mater, 49(19), 3899–3918.

Devlin, N. R., Brown, D. K., and Kohl, P. A., 2009, Patterning decomposable polynorbornene with electron beam lithography to create nanochannels. Journal of Vacuum Science & Technology. B, 27(6), 2508- 2511.

Dimov, S., Brousseau, E., Minev, R., and Bigot, S., 2012, Micro- and Nano-Manufacturing: Challenges and Opportunities. Proceedings of the Institution of Mechanical Engineers, Part C: Journal of Mechanical Engineering Science, 226(1), 3-15.

Dornfeld D., Min S., Takeuchi Y., 2006, Recent advances in mechanical micromachining. CIRP Annals - Manufacturing Technology, 55(2): 745–768.

Duan, N., Yu, Y., Wang, W. and Xu, X., 2017. Analysis of grit interference mechanisms for the double scratching of monocrystalline silicon carbide by coupling the FEM and SPH. International Journal of Machine Tools and Manufacture, 120, 49-60.

Duan, N., Yu, Y., Wang, W. and Xu, X., 2017. SPH and FE coupled 3D simulation of monocrystal SiC scratching by single diamond grit. International Journal of Refractory Metals and Hard Materials, 64, 279-293.

Egashira K. and Mizutani K., 2002, Micro-drilling of monocrystalline silicon using a cutting tool. Precision Engineering, 26(3): 263–268.

Elkaseer, A., and Brousseau, E. B., 2013, Modelling the surface generation process during AFM probe-based machining: simulation and experimental validation. Surface Topography: Metrology and Properties, 2(2), 025001.

Engstrom, D. S., Porter, B., Pacios, M., and Bhaskaran, H., 2014, Additive Nanomanufacturing - A Review. Journal of Materials Research, 29(17), 1792-1816.

Fang, F. Z., Wu, H., & Liu, Y. C., 2005, Modelling and experimental investigation on nanometric cutting of monocrystalline silicon. International Journal of Machine Tools and Manufacture, 45(15), 1681-1686.

Fang, F. Z., Zhang, X. D., Gao, W., Guo, Y. B., Byrne, G., & Hansen, H. N. (2017). Nanomanufacturing—Perspective and applications. Cirp Annals, 66(2), 683-705.

Fang, F., & Xu, F., 2018, Recent advances in micro/nano-cutting: effect of tool edge and material properties. Nanomanufacturing and Metrology, 1, 4-31.

Flórez García, L. C., González Rojas, H. A., & Sánchez Egea, A. J., 2020, Estimation of specific cutting energy in an S235 alloy for multi-directional ultrasonic vibration-assisted machining using the finite element method. Materials, 13(3), 567.

Fu, G., Sun, F., Huo, D., Shyha, I., Sun, F., & Fang, C., 2021, FE-simulation of machining processes of epoxy with Mulliken Boyce model. Journal of Manufacturing Processes, 71, 134-146.

Gallet, C., Lacome, J. L., 2002, S.P.H.: A Solution to Avoid Using Erosion Criterion DYNAlook.

Gao, S., and Huang, H., 2017, Recent advances in micro- and nano-machining technologies. Frontiers of Mechanical Engineering, 12(1), 18–32.

Geng, X., Dou, W., Deng, J., Ji, F. and Yue, Z., 2017. Simulation of the orthogonal cutting of OFHC copper based on the smoothed particle hydrodynamics method. The International Journal of Advanced Manufacturing Technology, 91(1), 265-272.

Geng, Y., Brousseau, E., Zhao, X., Gensheimer, M., & Bowen, C., 2018, AFM tip-based nanomachining with increased cutting speed at the tool-workpiece interface. Precision Engineering, 51, 536-544.

Geng, Y., Yan, Y., Brousseau, E., Yu, B., Qu, S., Hu, Z., & Zhao, X., 2016, Processing Outcomes of the AFM Probe-Based Machining Approach with Different Feed Directions, Precision Engineering, 46, 288- 300.

Geng, Y., Yan, Y., Brousseau, E., & Sun, Y., 2017, AFM tip-based mechanical nanomachining of 3D micro and nano-structures via the control of the scratching trajectory. Journal of Materials Processing Technology, 248, 236-248.

Geng, Y., Yan, Y., Wang, J., Brousseau, E., Sun, Y., & Sun, Y., 2018, Fabrication of periodic nanostructures using AFM tip-based nanomachining: combining groove and material pile-up topographies. Engineering, 4(6), 787-795.

Geng, Y., Zhang, J., Yan, Y., Yu, B., Geng, L., & Sun, T., 2015, Experimental and Theoretical Investigation of Crystallographic Orientation Dependence of Nanoscratching of Single Crystalline Copper. Plos One, 10(7), e0131886.

Gingold, R., and Monaghan, J., 1977, Smoothed Particle Hydrodynamics: Theory and Application to Non-Spherical Stars. Monthly Notices of the Royal Astronomical Society, 181(3), 375-389.

Gouskov, A., Nikolaev, S., Kuts, V., Nizametdinov, F., Korovaitseva, E., & Yuan, S., 2018, Analysis of displacement fields of particle shaping surface during nanoscale ductile mode cutting of brittle materials. The International Journal of Advanced Manufacturing Technology, 95, 1911-1918.

Gu, X., Wang, H., Zhao, Q., Xue, J. and Guo, B., 2018. Effect of cutting tool geometries on the ductile-brittle transition of monocrystalline sapphire. International Journal of Mechanical Sciences, 148, 565-577.

Guo, X., Li, Y., Cai, L., Guo, J., Kang, R., Jin, Z. and Guo, D., 2020. Effects of tool edge radius on chip formation during the micromachining of pure iron. The International Journal of Advanced Manufacturing Technology, 108(7), 2121-2130.

Guo, X.G., Liu, Z.Y., Gao, H., Guo, D.M., 2015. Nano-indentation study on the (001) face of KDP crystal based on SPH method. Journal of Semiconductors, 36(8), p.083007.

Guo, Z., Tian, Y., Liu, X., Wang, F., Zhou, C. and Zhang, D., 2017. Modeling and simulation of the probe tip based nanochannel scratching. Precision Engineering, 49, 136-145.

Hallquist J. O., 2003. LS-DYNA Keyword User's Manual. Livermore Software Technology Corporation, California.

Hallquist J. O., 2006. LS-DYNA Theory Manual. Livermore Software Technology Corporation, California.

He, Y., Geng, Y., Yan, Y., & Luo, X., 2017, Fabrication of nanoscale pits with high throughput on polymer thin film using AFM tip-based dynamic plowing lithography. Nanoscale Research Letters, 12(1), 1-11.

He, Y., Yan, Y., Geng, Y., & Brousseau, E., 2018, Fabrication of periodic nanostructures using dynamic plowing lithography with the tip of an atomic force microscope. Applied Surface Science, 427, 1076-1083.

He, Y., Yan, Y., Geng, Y., & Hu, Z., 2017, Fabrication of none-ridge nanogrooves with large-radius probe on PMMA thin-film using AFM tip-based dynamic plowing lithography approach. Journal of Manufacturing Processes, 29, 204-210.

Huang, H. T., Ger, T. R., Lin, Y. H., & Wei, Z. H. (2013). Single cell detection using a magnetic zigzag nanowire biosensor. Lab on a Chip, 13(15), 3098-3104.

Huo, D., Liang, Y., & Cheng, K., 2007, An investigation of nanoindentation tests on the single crystal copper thin film via an AFM and MD simulation. Proceedings of the IMechE, Part C: Journal of Mechanical Engineering Science, 221, 259-266.

Islam, S. and Ibrahim, R.N., 2011. Mechanism of abrasive wear in nanomachining. Tribology letters, 42(3), 275- 284.

Islam, S., Ibrahim, R., Das, R. and Fagan, T., 2012. Novel approach for modelling of nanomachining using a mesh-less method. Applied Mathematical Modelling, 36(11), 5589-5602.

Jin, X., & Unertl, W. N., 1992, Submicrometer modification of polymer surfaces with a surface force microscope. Applied physics letters, 61(6), 657-659.

Johnson, G. R., Stryk, R. A., and Beissel, S. R., 1996, "SPH for High Velocity Impact Computations," Computer Methods in Applied Mechanics & Engineering, 139(1), 347-373.

Johnson, G.R., 1983. A constitutive model and data for materials subjected to large strains, high strain rates, and high temperatures. Proc. 7th Inf. Sympo. Ballistics, 541-547.

Jones, N., "Structural Aspects of Ship Collisions," Chapter 11, in Structural Crashworthiness, Eds. N. Jones and T Wierzbicki, Butterworths, London, 308-337 (1983).

Kareer, A., Hou, X.D., Jennett, N.M. and Hainsworth, S.V., 2016. The existence of a lateral size effect and the relationship between indentation and scratch hardness in copper. Philosophical Magazine, 96(32-34), 3396-3413.

Karimzadeh A, Ayatollahi MR, Alizadeh M (2014) Finite element simulation of nano-indentation experiment on aluminum 1100. Comput Mater Sci 81:595–600.

Karkalos, N. E., & Markopoulos, A. P., 2019, Examination of the influence of cutting conditions on nano-metric face milling using MD models. In IOP Conference Series: Materials Science and Engineering (Vol. 564, No. 1, p. 012008). IOP Publishing.

Karkalos, N. E., Markopoulos, A. P., & Kundrák, J., 2018, 3D molecular dynamics model for nano-machining of fcc and bcc materials. Procedia CIRP, 77, 203-206.

Kreig, R. D., and Key, S. W., 1976, "Implementation of a time dependent plasticity theory into structural programs", Constitutive Equations in Viscoplasticity: Computational and Engineering Aspects, 20, 125-137.

Kulasegaram, S., Bonet, J., Lewis, R. W., and Profit, M., 2004, "A Variational Formulation Based Contact Algorithm for Rigid Boundaries in Two-Dimensional SPH Applications," Computational Mechanics, 33(4), 316-325.

Kurniawan, R., Kumaran, S. T., & Ko, T. J., 2021, Finite element analysis in ultrasonic elliptical vibration cutting (UEVC) during micro-grooving in AISI 1045. International Journal of Precision Engineering and Manufacturing, 22, 1497-1515.

Leach, R., 2001, The measurement of surface texture using stylus instruments. NPL.

Leroch, S., Varga, M., Eder, S.J., Vernes, A., Ripoll, M.R. and Ganzenmüller, G., 2016. Smooth particle hydrodynamics simulation of damage induced by a spherical indenter scratching a viscoplastic material. International Journal of Solids and Structures, 81, 188-202.

Li, M., Guo, X., Zhai, R., Luo, X., Kang, R., Jin, Z. and Guo, D., 2021. Study on the subsurface damage mechanism of optical quartz glass during single grain scratching. Ceramics International, 47(6), 7683-7691.

Liao Y. S., Chen S. T., Lin C. S., et al., 2005, Fabrication of high aspect ratio microstructure arrays by micro reverse wire-EDM. Journal of Micromechanics and Microengineering, 15(8): 1547–1555.

Liao, Y., Song, J., Li, E., Luo, Y., Shen, Y., Chen, D., Cheng, Y., Xu, Z., Suqioka, K., and Midorikawa, K., 2012, "Rapid Prototyping of Three-Dimensional Microfluidic Mixers in Glass by Femtosecond Laser Direct Writing," Lab on A Chip, 12(4), 746-749.

Lin, H. Y., Chen, H. A., & Lin, H. N. (2008). Fabrication of a single metal nanowire connected with dissimilar metal electrodes and its application to chemical sensing. Analytical Chemistry, 80(6), 1937-1941.

Lin, Z. C., & Huang, J. C., 2008, A study of the estimation method of the cutting force for a conical tool under nanoscale depth of cut by molecular dynamics. Nanotechnology, 19(11), 115701.

Liu, G. R., and Liu, M. B., 2003, "Smooth Particle Hydrodynamics - A Meshfree Particle Method," World Scientific Publishing Co. Pte. Ltd, Singapore.

Liu, K., and Melkote, S. N., 2006, "Effect of Plastic Side Flow on Surface Roughness in Micro-Turning Process," International Journal of Machine Tools and Manufacture, 46(14), 1778-1785.

Liu, M. B., Liu, G. R., and Lam, K. Y., 2002, "Coupling Meshfree Particle Method with Molecular Dynamics - A Novel Approach for Multi-Scale Simulations," Advances in Meshfree and X-FEM Methods, 211-216.

Liu, M. B., Liu, G. R., Zong, Z., and Lam, K. Y., 2003, "Computer Simulation of the High Explosive Explosion Using Smoothed Particle Hydrodynamics Methodology," Computers & Fluids, 32(3), 305-322.

Luo, X., Cheng, K., and Ward, R., 2005, The Effects of Machining Process Variables and Tooling Characterisation on the Surface Generation, International Journal of Advanced Manufacturing Technology, 25(11-12), 1089-1097.

Mabrouki, T., Girardin, F., Asad, M., & Rigal, J. F., 2008, Numerical and experimental study of dry cutting for an aeronautic aluminium alloy (A2024-T351). International Journal of Machine Tools and Manufacture, 48(11), 1187-1197.

Madaj, M., & Píška, M., 2013, On the SPH orthogonal cutting simulation of A2024-T351 alloy. Procedia Cirp, 8, 152-157.

Maekawa, K., & Itoh, A., 1995, Friction and tool wear in nano-scale machining—a molecular dynamics approach. Wear, 188(1-2), 115-122.

Mao C., Sun X., Huang H., et al., 2016, Characteristics and removal mechanism in laser cutting of cBN-WC-10Co composites, Journal of Materials Processing Technology, 230: 42–49.

Markopoulos, A. P., Karkalos, N. E., & Kundrák, J., 2018, Nanometric face milling simulations using MD method. In IOP Conference Series: Materials Science and Engineering (Vol. 448, No. 1, p. 012006). IOP Publishing.

Markopoulos, A. P., Karkalos, N. E., & Papazoglou, E. L., 2020, Meshless methods for the simulation of machining and micro-machining: a review. Archives of Computational Methods in Engineering, 27, 831-853.

Masuzawa, T., 2000, State of the art of micromachining. Cirp Annals, 49(2), 473-488.

Menard, L. D., and Ramsey, J. M., 2011, “Fabrication of Sub-5 nm Nanochannels in Insulating Substrates Using Focused Ion Beam Milling,” Nano Letters, 11(2), 512-517.

Nitsche, L. C., and Zhang, W. D., 2002, “Atomistic SPH and a Link Between Diffusion and Interfacial Tension,” Fluid Mechanics and Transport Phenomena, 48(2), 201-211.

Noritaka, K., Noboru, T., Daisuke, & Oka, et al., 2005, Nanomachining of silicon surface using atomic force microscope with diamond tip. Journal of Manufacturing Science and Engineering, 128(3), 723-729.

Oymak, M., Bahçe, E., & Gezer, İ., 2021, Investigation of cryogenic cooling effect with finite element method in micro milling of Ti6Al4V material. International Journal of Innovative Engineering Applications, 5(2), 93-100.

Park, S., Mostofa, M., Park, C., Mehrpouya, M., & Kim, S., 2014, Vibration assisted nano mechanical machining using AFM prob. CIRP Annals - Manufacturing Technology, 63, 537–540.

Rahman M., Asad A., Masaki T., et al., 2010, A multiprocess machine tool for compound micromachining. International Journal of Machine Tools & Manufacture, 50(4): 344–356.

Randles, P., Carney, T., Libersky, L., Renick, J., & Petschek, A., 1995, Calculation of Oblique Impact and Fracture of Tungsten Cubes Using Smoothed Particle Hydrodynamics. International Journal of Impact Engineering, 17(4), 661-672.

Rüttimann, N., Roethlin, M., Buhl, S., & Wegener, K., 2013, Simulation of hexa-octahedral diamond grain cutting tests using the SPH method. Procedia CIRP, 8, 322-327.

Shchurov, I., Nikonov, A., & Boldyrev, I., 2016, SPH-simulation of the fiber-reinforced composite workpiece cutting for the surface quality improvement. Procedia Engineering, 150, 860-865.

Shi, Z., Xiang, D., Feng, H., Wu, B., Zhang, Z., Gao, G., & Zhao, B., 2021, Finite element and experimental analysis of ultrasonic vibration milling of high-volume fraction SiCp/Al composites. International Journal of Precision Engineering and Manufacturing, 22(10), 1777-1789.

Simoneau, A., Ng, E., & Elbestawi, M., 2006, Chip formation during microscale cutting of a medium carbon steel. International Journal of Machine Tools and Manufacture, 46(5), 467-481.

Stenberg, N., Delić, A., & Björk, T., 2017, Using the SPH method to easier predict wear in machining. Procedia CIRP, 58, 317-322.

Sun, X., & Cheng, K., 2010, Micro/nano-machining through mechanical cutting. Manufacturing Engineering and Technology, Editor: Qin, Y., Elsevier, 24-38.

Sun, X., and Cheng, K., 2010, Multiscale simulation of the nanometric cutting process, International Journal of Advanced Manufacturing Technology, 47, 891-901.

Sun, Y., Yan, Y., Liang, Y., Hu, Z., Zhao, X., Sun, T., Dong, S., 2013, Effect of the molecular weight on deformation states of the polystyrene film by AFM single scanning. Scanning, 35(5), 308–315.

Takabi, B., Tajdari, M., & Tai, B. L., 2017, Numerical study of smoothed particle hydrodynamics method in orthogonal cutting simulations–Effects of damage criteria and particle density. Journal of Manufacturing Processes, 30, 523-531.

Takacs, M., Verö, B., & Meszaros, I., 2003, Micromilling of metallic materials. Journal of Materials Processing Technology, 138(1-3), 152-155.

Tseng, A., 2011, Removing Material Using Atomic Force Microscopy with Single- and Multiple-Tip Sources, Small, 7(24), 3409-3427.

Tsuru T, Shibutani Y, Kaji Y (2010) Nanoscale contact plasticity of crystalline metal: experiment and analytical investigation via atomistic and discrete dislocation models. Acta Mater 58(8):3096–3102.

Vahid Hosseini, S., Vahdati, M., & Shokuhfar, A., 2011, Effect of tool nose radius on nano-machining process by molecular dynamics simulation. Defect & Diffusion Forum, 312-315, 977-982.

Varga, M., Leroch, S., Eder, S. J., & Ripoll, M. R., 2017, Meshless microscale simulation of wear mechanisms in scratch testing. Wear, 376, 1122-1129.

Villumsen, M. and Fauerholdt, T., 2008, Simulation of Metal Cutting using Smoothed Particle Hydrodynamics, 7. LS-DYNA Anwenderforum, C-III-17–C-III-36.

Vogler, M., DeVor, R., & Kapoor, S., 2004, On the Modelling and Analysis of Machining Performance in Micro-Endmilling, Part I: Surface Generation. Journal of Manufacturing Science and Engineering, 126(4), 685-694.

Wang CT, Jian SR, Jang JSC, Lai YS, Yang PF (2008) Multiscale simulation of nanoindentation on Ni (1 0 0) thin film. Applied Surface Science 255(5):3240–3250.

Wang, J., Yan, Y., Chang, S., Han, Y., & Geng, Y. (2020). Label-free surface-enhanced Raman spectroscopy detection of absorption manner of lysozyme based on nanodots arrays. Applied Surface Science, 509, 145332.

Wang, J., Yan, Y., Geng, Y., Gan, Y., & Fang, Z. (2019). Fabrication of polydimethylsiloxane nanofluidic chips under AFM tip-based nanomilling process. Nanoscale Research Letters, 14, 1-14.

Wang, W., Wan, Z., Yang, S., Feng, J., Dong, L., & Lu, L., 2020, Experimental and numerical investigation on the effect of scratch direction on material removal and friction characteristic in BK7 scratching. Materials, 13(8), 1842.

Woon, K. S., Rahman, M., Fang, F. Z., Neo, K. S., & Liu, K., 2008, Investigations of tool edge radius effect in micromachining: a FEA simulation approach. Journal of Materials Processing Tech, 195(1-3), 204-211.

Xi, Y., Bermingham, M., Wang, G., & Dargusch, M., 2014, SPH/FE modelling of cutting force and chip formation during thermally assisted machining of Ti6Al4V alloy. Computational materials science, 84, 188-197.

Xiao, G., He, Y., Geng, Y., Yan, Y., & Ren, M., 2019, Molecular dynamics and experimental study on comparison between static and dynamic ploughing lithography of single crystal copper. Applied Surface Science, 463, 96-104.

Xie, X. N., Chung, H. J., Sow, C. H., and Wee, A. T. S., 2006, Nanoscale Materials Patterning and Engineering by Atomic Force Microscopy Nanolithography, Materials Science and Engineering R54, 1-48.

Xu, Y., Wang, M., Zhu, F., Liu, X., Chen, Q., Hu, J., & Liu, Y., 2019, A molecular dynamic study of nano-grinding of a monocrystalline copper-silicon substrate. Applied Surface Science, 493, 933-947.

Yan, Y., He, Y., Geng, Y., Hu, Z., & Zhao, X., 2016, Characterization study on machining PMMA thin-film using AFM tip-based dynamic plowing lithography. Scanning, 612-618.

Yan, Y., Geng, Y., and Hu, Z., 2015, Recent advances in AFM tip-based nanomechanical machining, International Journal of Machine Tools & Manufacture, 99, 1-18.

Youn, S. W., & Kang, C. G., 2005, FEA study on nanodeformation behaviours of amorphous silicon and borosilicate considering tip geometry for pit array fabrication. Materials Science & Engineering A, 390(1-2), 233-239.

Zhang, L., & Tanaka, H., 1997, Towards a deeper understanding of wear and friction on the atomic scale—a molecular dynamics analysis. Wear, 211(1), 44-53.

Zhang, S. and Zong, W., 2020. Micro defects on diamond tool cutting edge affecting the ductile-mode machining of KDP crystal. Micromachines, 11(12), p.1102.

Zhang, S., Zhang, H., & Zong, W., 2019, Modeling and simulation on the effect of tool rake angle in diamond turning of KDP crystal. Journal of Materials Processing Technology, 273, 116259.

Zhao, H., Liu, C., Cui, T., Tian, Y., Shi, C., Li, J., & Huang, H., 2013, Influences of sequential cuts on micro-cutting process studied by smooth particle hydrodynamic (SPH). Applied surface science, 284, 366-371.

Zhao, H., Zhang, P., Liu, H., Liu, C., Tong, D., Zhang, L., Ren, L., Dong, X. & Liang, S., 2014. Influences of residual stress induced by cutting on subsequent scratch using smooth particle hydrodynamic (SPH). Materials Transactions, p.M2014078.

Zhao, P., Wu, J., Chen, H., Liu, H., Li, D., & Tan, J., 2021, Molecular dynamics simulation study of interaction mechanism between grain boundaries and subgrain boundaries in nano-cutting. Journal of Manufacturing Processes, 67, 418-426.

Zhong, Y., Zhao, H., Ma, Z., Shi, Y., & Fu, H., 2017, A study on the effect of double-tip inclined angle on micro-scratching process using smooth particle hydrodynamic method. Advances in Mechanical Engineering, 9(8), 1687814017720877.

Zhou, L., and Cheng, K., 2009, Dynamic cutting process modelling and its impact on the generation of surface topography and texture in nano/micro cutting, Proceedings of the Institution of Mechanical Engineers, Part B: Journal of Engineering Manufacture, 223(3), 247-266.

Zhou, M., Wang, X., Ngoi, B., & Gan, J., 2002, Brittle-ductile transition in the diamond cutting of glasses with the aid of ultrasonic vibration. Journal of Materials Processing Technology, 121, 243–251.

Zong, W., Sun, T., Li, D., and Cheng, K., 2010, The basic issues in design and fabrication of diamond-cutting tools for ultra-precision and nanometric machining. International Journal of Machine Tools and Manufacture, 50(4), 411-419.

Appendix – Simulation code of AFM probe-based DPL

This appendix shows the developed simulation code for the SPH simulation of AFM probe-based DPL used in Chapter 6. The vibration amplitude and vibration period of the AFM probe employed in this simulation code are 4 nm and 2 nm, respectively. The following code can be used as input into ANSYS/LS-DYNA software:

```
*KEYWORD MEMORY=2000000000
*TITLE
*CONTROL_CONTACT
   1.000000        0.000             0             0             0             0             0             0
             0             0             0             0         0.000             0             0             0
         0.000         0.000         0.000         0.000         0.000         0.000         0.000
             0             0             0             0             0             0         0.000
             0             0             0         0.000     1.000000             0         0.000             0
             0
*CONTROL_ENERGY
             2             2             2             2
*CONTROL_SPH
             0             0         0.000             3             0             0         0.000         0.000
             0             0
*CONTROL_TERMINATION
   0.004000             0         0.000         0.000         0.000
*CONTROL_TIMESTEP
         0.000     0.900000             0         0.000         0.000             0             0             0
         0.000             0             0
*DATABASE_RCFORC
   5.0000E-5             0             0             1
*DATABASE_SPCFORC
   5.0000E-5             0             0             1
*DATABASE_BINARY_D3PLOT
   5.0000E-5             0             0             0             0
             0
*DATABASE_FORMAT
             0             0
*DATABASE_EXTENT_BINARY
             0             0             3             1             1             1             1             1
             0             0             4             1             1             1             2             1
             0             0     1.000000             0             0             0
```

```
*DATABASE_EXTENT_BINARY
         0         0         0         0         0         0         0         0
         0         0         0         1         1         1         2         1
         0         0  1.000000         0         0         0
*BOUNDARY_PRESCRIBED_MOTION_RIGID
         1         3         0         3  1.000000         0     0.000     0.000
*BOUNDARY_PRESCRIBED_MOTION_RIGID
         1         1         0         1  1.000000         0     0.000     0.000
*BOUNDARY_SPC_SET
         2         0         1         1         1         1         1         1
*CONTACT_ERODING_NODES_TO_SURFACE
         1         1         4         3         0         0         0         0
     0.000     0.000     0.000     0.000     0.000         1     0.000     0.000
  1.000000  1.000000     0.000     0.000  1.000000  1.000000  1.000000  1.000000
         1         1         1
         1     0.000         0     0.000     0.000         0         0         0
*PART
RIGID
         1         1         1         0         0         0         0         0
*SECTION_SOLID
         1         1         0
*MAT_RIGID
         1  3.515E-12  1141.000  0.070000     0.000     0.000     0.000
  1.000000         2         7
     0.000     0.000     0.000     0.000     0.000     0.000
*PART
SphNode
         6         2         2         2         0         0         0         0
*SECTION_SPH
         2  1.200000     0.000     0.000     0.000     0.000     0.000
*MAT_JOHNSON_COOK_TITLE
JC model for cooper
         2  8.93E-12 43.330002   117.000    0.3500  1.80E-7     0.000     0.000
  0.090000  0.292000  0.310000  0.025000  1.090000 1356.0000  293.00000  1.000000
 3.8300E+8     0.000  2.000000     0.000  1.200000     0.000     0.000     0.000
     0.000     0.000         0 1.0000E-6
*EOS_GRUNEISEN_TITLE
EOS for copper
         2 3.9850E+6  1.497000     0.000     0.000  2.020000  0.470000     0.000
     0.000
*DEFINE_CURVE
         1         0  1.000000  1.000000     0.000     0.000         0
                 0.000          2000.0000000
```

```
            0.0040000        2000.0000000
*DEFINE_CURVE
$4
         3         0  1.000000  1.000000     0.000     0.000         0
               0.000      -80000.000000
     4.9999999e-005      -80000.000000
     4.9999999e-005       80000.000000
     9.9999997e-005       80000.000000
     9.9999997e-005      -80000.000000
     1.5000001e-004      -80000.000000
     1.5000001e-004       80000.000000
     1.9999999e-004       80000.000000
     1.9999999e-004      -80000.000000
     2.5000001e-004      -80000.000000
     2.5000001e-004       80000.000000
     3.0000001e-004       80000.000000
     3.0000001e-004      -80000.000000
     3.4999999e-004      -80000.000000
     3.4999999e-004       80000.000000
     3.9999999e-004       80000.000000
     3.9999999e-004      -80000.000000
     4.4999999e-004      -80000.000000
     4.4999999e-004       80000.000000
     5.0000002e-004       80000.000000
     5.0000002e-004      -80000.000000
     5.5000000e-004      -80000.000000
     5.5000000e-004       80000.000000
     6.0000003e-004       80000.000000
     6.0000003e-004      -80000.000000
     ……
          0.0034000       80000.000000
          0.0034000      -80000.000000
          0.0034500      -80000.000000
          0.0034500       80000.000000
          0.0035000       80000.000000
          0.0035000      -80000.000000
          0.0035500      -80000.000000
          0.0035500       80000.000000
          0.0036000       80000.000000
          0.0036000      -80000.000000
          0.0036500      -80000.000000
          0.0036500       80000.000000
          0.0037000       80000.000000
```

```
        0.0037000      -80000.000000
        0.0037500      -80000.000000
        0.0037500       80000.000000
        0.0038000       80000.000000
        0.0038000      -80000.000000
        0.0038500      -80000.000000
        0.0038500       80000.000000
        0.0039000       80000.000000
        0.0039000      -80000.000000
        0.0039500      -80000.000000
        0.0039500       80000.000000
        0.0040000       80000.000000
*SET_NODE_LIST
         2     0.000     0.000     0.000     0.000
    184394    184395    184396    184397    184398    184399    184400    184401
    184402    184403    184404    184405    184406    184407    184408    184409
    184410    184411    184412    184413    184414    184415    184416    184417
    184418    184419    184420    184421    184422    184423    184424    184425
    184426    184427    184428    184429    184430    184431    184432    184433
    184434    184435    184436    184437    184438    184439    184440    184441
    184442    184443    184444    184445    184446    184447    184448    184449
    184450    184451    184452    184453    184454    184455    184456    184457
    184458    184459    184460    184461    184462    184463    184464    184465
    184466    184467    184468    184469    184470    184471    184472    184473
    184474    184475    184476    184477    184478    184479    184480    184481
    ..........................................................................................
    296750    296751    296752    296753    296754    296755    296756    296757
    296758    296759    296760    296761    296762    296765    296766    296767
    296768    296769    296770    296771    296772    296773    296774    296775
    296776    296777    296778    296779    296780    296781    296782    296783
    296786    296787    296788    296789    296790    296791    296792    296793
    296794    296795    296796    296797    296798    296799    296800    296801
    296802    296803    296804    296807    296808    296809    296810    296811
    296812    296813    296814    296815    296816    296817    296818    296819
    296820    296821    296822    296823    296824    296825    296828    296829
    296830    296831    296832    296833    296834    296835    296836    296837
    296838    296839    296840    296841    296842    296843    296844    296845
    296846    296849    296850    296851    296852    296853    296854    296855
    296856    296857    296858    296859    296860    296861    296862    296863
    296864    296865    296866    296867         0         0         0         0
*SET_NODE_LIST
         1     0.000     0.000     0.000     0.000
    163100    163101    163102    163103    163104    163105    163106    163107
```

163108 163109 163110 163111 163112 163113 163114 163115
163116 163117 163118 163119 163120 163121 163122 163123
163124 163125 163126 163127 163128 163129 163130 163131
163132 163133 163134 163135 163136 163137 163138 163139
163140 163141 163142 163143 163144 163145 163146 163147
163148 163149 163150 163151 163152 163153 163154 163155
163156 163157 163158 163159 163160 163161 163162 163163
163164 163165 163166 163167 163168 163169 163170 163171
163172 163173 163174 163175 163176 163177 163178 163179
.....
318084 318085 318086 318087 318088 318089 318090 318091
318092 318093 318094 318095 318096 318097 318098 318099
318100 318101 318102 318103 318104 318105 318106 318107
318108 318109 318110 318111 318112 318113 318114 318115
318116 318117 318118 318119 318120 318121 318122 318123
318124 318125 318126 318127 318128 318129 318130 318131
318132 318133 318134 318135 318136 318137 318138 318139
318140 318141 318142 318143 318144 318145 318146 318147
318148 318149 318150 318151 318152 318153 318154 318155
318156 318157 318158 318159 318160 318161 318162 318163
*ELEMENT_SOLID
1 1 11 36 12 19 19 19 19 19
2 1 15 25 29 40 40 40 40 40
3 1 9 34 37 10 10 10 10 10
4 1 21 32 26 22 22 22 22 22
5 1 25 27 29 40 40 40 40 40
6 1 5 39 6 26 26 26 26 26
7 1 10 36 33 37 37 37 37 37
8 1 3 27 40 4 4 4 4 4
9 1 12 30 36 13 13 13 13 13
10 1 6 22 39 8 8 8 8 8
11 1 24 25 27 29 29 29 29 29
12 1 4 38 5 28 28 28 28 28
13 1 6 26 39 22 22 22 22 22
14 1 14 29 31 35 35 35 35 35
15 1 3 40 27 25 25 25 25 25
.....
72 1 30 33 36 43 43 43 43 43
73 1 35 36 37 43 43 43 43 43
74 1 33 36 43 37 37 37 37 37
75 1 33 37 43 34 34 34 34 34
76 1 17 20 34 43 43 43 43 43
77 1 20 34 43 41 41 41 41 41

78	1	20	41	43	42	42	42	42	42
79	1	17	20	43	42	42	42	42	42
80	1	34	37	43	41	41	41	41	41
81	1	37	43	41	42	42	42	42	42
82	1	35	43	37	42	42	42	42	42
83	1	31	43	35	42	42	42	42	42
84	1	23	27	29	24	24	24	24	24
85	1	23	29	27	42	42	42	42	42
86	1	17	33	30	43	43	43	43	43
87	1	17	30	33	18	18	18	18	18

*ELEMENT_SPH

163100	6	8.5274913e-014
163101	6	8.6704014e-014
163102	6	8.7711502e-014
163103	6	8.7799038e-014
163104	6	8.7800793e-014
163105	6	8.7800793e-014
163106	6	8.7800793e-014
163107	6	8.7799058e-014
163108	6	8.7800840e-014
163109	6	8.7800759e-014
163110	6	8.7800840e-014
163111	6	8.7800793e-014
163112	6	8.7799010e-014
163113	6	8.7800793e-014
163114	6	8.7800881e-014
163115	6	8.7784746e-014
163116	6	8.7640012e-014
163117	6	8.7457751e-014
……		
318147	6	8.7808084e-014
318148	6	8.7809785e-014
318149	6	8.7808084e-014
318150	6	8.7809819e-014
318151	6	8.7808036e-014
318152	6	8.7809819e-014
318153	6	8.7808036e-014
318154	6	8.7809859e-014
318155	6	8.7807996e-014
318156	6	8.7809859e-014
318157	6	8.7808036e-014
318158	6	8.7791977e-014
318159	6	8.7649072e-014

```
   318160          6   8.7463152e-014
   318161          6   8.7043504e-014
   318162          6   8.6170085e-014
   318163          6   8.5598283e-014
*NODE
        1    -4.0300002     2.3299999     3.2900000           0           0
        2         0.000     -4.6501999     3.2900000           0           0
        3    -3.2240000     0.9339700     3.2900000           0           0
        4    -2.4180000    -0.4620700     3.2900000           0           0
        5    -1.6120000    -1.8581001     3.2900000           0           0
        6    -0.8060001    -3.2541001     3.2900000           0           0
        7     4.0300002     2.3299999     3.2900000           0           0
        8     0.8060001    -3.2541001     3.2900000           0           0
        9     1.6120000    -1.8581001     3.2900000           0           0
       10     2.4180000    -0.4620700     3.2900000           0           0
       11     3.2240000     0.9339700     3.2900000           0           0
       12     2.4180000     2.3299999     3.2900000           0           0
       13     0.8060001     2.3299999     3.2900000           0           0
       14    -0.8060001     2.3299999     3.2900000           0           0
       15    -2.4180000     2.3299999     3.2900000           0           0
       ..........................................................................
   318149    13.8716002    -5.0778999    -2.5868001           0           0
   318150    13.8716002    -5.0778999    -2.8326001           0           0
   318151    13.8716002    -5.0778999    -3.0783999           0           0
   318152    13.8716002    -5.0778999    -3.3241999           0           0
   318153    13.8716002    -5.0778999    -3.5699999           0           0
   318154    13.8716002    -5.0778999    -3.8157001           0           0
   318155    13.8716002    -5.0778999    -4.0615001           0           0
   318156    13.8716002    -5.0778999    -4.3073001           0           0
   318157    13.8716002    -5.0778999    -4.5531001           0           0
   318158    13.8716002    -5.0778999    -4.7988000           0           0
   318159    13.8716002    -5.0778999    -5.0444002           0           0
   318160    13.8716002    -5.0778999    -5.2895002           0           0
   318161    13.8716002    -5.0778999    -5.5337000           0           0
   318162    13.8716002    -5.0778999    -5.7761002           0           0
   318163    13.8716002    -5.0778999    -6.0165000           0           0
*END
```